An Experimental Investigation of the Attachment Line Boundary Layer Transition on Swept Cylinders in Hypervelocity Flow

高温極超音速気流中における斜め円柱付着線境界層の遷移に関する実験的研究

Keisuke Fujii

藤井啓介

Abstract

An exploratory experiment was performed on high enthalpy effects on hypersonic boundary layer transition using nitrogen, air and carbon dioxide as test gases in the T5 hypervelocity shock tunnel, Graduate Aeronautical Laboratories, California Institute of Technology. Previous experiments in the facility on transition of a sharp cone boundary layer showed significant effects of total enthalpy especially for carbon dioxide cases. This series concerns how the total enthalpy effect appears depending on conditions of boundary layer such as representative temperature and edge Mach number. More in detail, an objective is to examine how the relation between the most strongly amplified frequency of linear instability mechanism and the characteristic frequencies of relaxation processes, affect transition when the significant high enthalpy effect is active.

Of particular interest is the question how the relaxation in chemical reactions and/or vibrational excitation affects the boundary layer transition when these have characteristic frequencies which are quite different from those in the previous cone experiments. Then, swept cylinder models with sweep angles of 60 deg and 45 deg have been chosen for the present experiment aiming to achieve large extent of the range in the ratio between the characteristic frequencies. The observed trend of transition Reynolds number with total enthalpy, which is found to be similar to that in the cone results, shows strong transition delay at the larger sweep angle for carbon dioxide, while no significant effect is observed in nitrogen and air. The larger inclination angle (*i.e.*, less sweep angle) leads to less total enthalpy effect on transition in terms of transition Reynolds number.

The acoustic wave absorption rate due to relaxation at the most strongly amplified frequency estimated at the reference enthalpy condition providing it as acoustic second mode reveals a quite similar trend in enthalpy dependence to observed transition Reynolds number for the carbon dioxide at the larger sweep case. This suggests that the dominant effect in delaying boundary layer transition in the carbon dioxide case is vibrational relaxation. A linear inviscid stability analysis was also carried out assuming perfect gas both for the boundary layer profile and for disturbances. The comparisons between the magnitude of the strongest amplification rate and the absorption rate due to relaxation show that they are of the same order of magnitude for carbon dioxide and

that absorption is not significant for nitrogen or air compared with linear instability amplification, which supports the above understanding of the effect of relaxation on transition. Estimated absorption rate evaluated for the smaller sweep angle case, however, does not explain the observations in transition Reynolds number dependence on total enthalpy.

In order to consider the effect of edge Mach number variation on the appearance of the high enthalpy effects, re-examination on the previous 5 deg half-angle cone experiments was made and compared with the present results in terms of momentum thickness Reynolds number. It then becomes clear that high enthalpy effect on transition loses its importance monotonically as the edge Mach number decreases from 5 to 2. Some possible mechanisms were proposed involving a change in the responsible instability mode in the boundary layer of interest as edge Mach number varies, however, this observed trend remains to be examined in the future.

In short, the present study indicated that the absorption due to relaxation process directly predicts the trend in transition Reynolds number with total enthalpy variation qualitatively well, supposing the edge Mach number high enough. As the edge Mach number decreases, the high enthalpy effects loses its importance monotonically.

要約

極超音速境界層の乱流遷移現象への高エンタルピー実在気体効果について調べる目的で、カリフォルニア工科大学 GALCIT(Graduate Aeronautical Laboratories) の T5 hypervelocity shock tunnel において、空気、窒素および二酸化炭素を試験気体とした一連の実験を実施した。同設備を用いた半頂角 5° の鋭い先端を持った円錐上に発達する境界層の遷移に関する過去の実験によれば、二酸化炭素を試験気体とした場合に、高エンタルピー効果によって乱流遷移が著しく遅れることが示されていた。今回の一連の実験は、境界層の代表温度や境界層端 Mach 数といった境界層の状態量が大きく異なるときに、この高エンタルピー効果がどのように現れるかについて実験的に調べることを目的としている。更には上記円錐実験で見られた高エンタルピー効果に関係して、境界層の線形不安定性により最も強く増幅される擾乱の周波数と、気体分子の振動や解離反応における緩和時間により定まる特性周波数との関係がどのように境界層遷移に影響を与えているかを調べることを具体的な目標とした。また、それが上記の円錐実験と比べて大きく異なるための条件について考察し、本研究では、これら二つの特性周波数の比を広い範囲で変化させることができるように後退角 45 deg と 60 deg の斜め円柱付着線における境界層を対象と定めた。本実験において遷移 Reynolds 数は、付着線における加熱率を計測し完全気体理論値と比較することで決定した。それらを総エンタルピーに対して整理したところ、高い後退角 ($\Lambda = 60$ deg) のケースにおいては、二酸化炭素を試験気体としたときには円錐実験における結果と同様に、高エンタルピー効果は遷移をきわめて強く遅らせることが明らかとなった。ただし、窒素、空気を試験気体とした場合では大きな効果は観測されなかった。また後退角の小さいケース ($\Lambda = 45$ deg) に関しては遷移 Reynolds 数への総エンタルピー効果は高後退角 ($\Lambda = 60$ deg) のケースと比べ、小さくなることが明らかとなった。

以上の実験結果を用いて、本実験条件において遷移へつながる線形不安定性が 2nd mode であると仮定して、もっとも強く増幅されると予想される周波数における音響減衰率を境界層の参照エンタルピー条件において算出した。その結果、大きな後退角の実験ケース ($\Lambda = 60$ deg) については音響減衰率の総エンタルピーに対する変化は、観測された遷移 Reynolds 数の総エンタルピー依存性にきわめて類似した特長を有することが示された。このことは、二酸化炭素分子の振動エネルギー緩和が主要な要因となって、本研究の二酸化炭素の実験で得られたような遷移 Reynolds 数を大きく増加させるという高エンタルピー効果が現れたという可能性を示唆している。次に、完全気体非粘性線形安定解析を実施し、最大増幅率ならびに上記のように算出された緩和による音響減衰率との比較を行った。その結果、二酸化炭素の実験条件では、それらはほぼ同オーダーの大きさで相互に効果を打ち消しあう状況であるのに対し、窒素および空気の実験条件では二つの特性周波数が離れすぎているため 2nd mode 周波数における音響減衰率はきわめて小さいことが示された。これらの結果は、大き

な後退角のケースの実験結果を支持している。

次に、境界層端 Mach 数への依存性あるいは境界層端 Mach 数が異なる場合における総エンタルピー依存性について調べるために、過去に実施された半頂角 5 ° 円錐の実験結果を、運動量厚を基準とした遷移 Reynolds 数として再整理し、本実験結果との比較をおこなった。その結果、境界層端 Mach 数の減少に伴い、遷移 Reynolds 数への総エンタルピー効果はその重要性を単調に失う傾向が明らかにされた。境界層端 Mach 数の減少に伴い音響擾乱の特徴を持つ 2nd mode 不安定性がその重要性を失うためにこの現象がおきるという可能性が考えられた。

以上、本研究において明らかにされたことをまとめると以下のとおりである:
境界層端 Mach 数の増加とともに高エンタルピー効果によって境界層遷移 Reynolds 数は増大する。この現象は高い Mach 数域における緩和現象による音響減衰によって定性的によく説明される。

Contents

List of Figures

List of Tables

Nomenclature

$\mathbf{A}$	= matrix of reciprocal of relaxation time constant, s^{-1}
a	= sound speed, m/s
C	= constant in equation 2.4, 1/s.Pa
	or specific heat of solid material, J/kg K
C_f	= rate coefficient appearing in Arrhenius rate equation
C_i	= mass fraction of ith species
c_s	= phase velocity of subsonic wave, m/s
D	= diameter of cylinder of the models, m
$f_{2\text{nd}}$	= most strongly amplified 2nd mode frequency, Hz (See equation 2.3)
g	= degeneracy
h	= enthalpy, J/kg
h_f^o	= formation enthalpy at standard condition per mole, J/mole
K	= constant in equation 2.4
K_{eq}	= equilibrium constant
k	= Roughness height, m
k_B	= Boltzmann constant, $=1.38054\times10^{-23}$ J/K
L	= length of the model, m
M	= Mach number
M_1	= relative edge Mach number defined as $\equiv \frac{u_e - c_s}{a_e}$
$\bar{M}$	= normalized relative Mach number defined as: $\equiv \frac{\alpha u + \beta w - \omega}{\sqrt{\alpha^2+\beta^2}} \frac{M_1}{\sqrt{T/T_e}}$
M_{w_i}	= molecular weight of ith species, kg/mole
m	= mass of molecule, kg
N_i	= mole mass ratio, mole/kg
$\mathcal{N}_i$	= number of mole of ith species, mole
P_r	= Prandtl number
p	= pressure, Pa
Q	= integrated heat to surface, J/m^2

$\mathbf{q}$ = vector of relaxation variables measured per unit mass

$\dot{q}$ = heat flux to surface, W/m^2

R = universal gas constant, =8.314 J/kg K

R_e = Reynolds number

R_{e_δ} = Reynolds number based on boundary layer thickness δ

r = cylinder radius, m

$\bar{R}$ = Poll's Reynolds number based on η

S_t = Stanton number

T = temperature, K

t = time, s

u, v, w = velocity components of x,y,z direction, m/s

V = velocity, m/s

x, y, z = coordinates defined as shown in figure 4.5(b), m

x_i = mole fraction of ith species, mole/mole

y_s = height at the generalized inflection point, m

y_o = height at which M_1 becomes unity,
i.e., at which relative velocity equals to speed of sound at the edge, m

α = x-component of wave number, m^{-1}
or degree of reaction, mole/kg

α_{relax} = absorption rate, m^{-1}

β = y-component of wave number, m^{-1}

γ = specific heat ratio

δ = boundary layer thickness, m

ε_{pw} = well depth of molecular potential energy, J

η = characteristic length defined by equation 2.8, m

η_f = constant appearing at chemical rate equation

κ = heat conductivity of solid material, W/m K

Λ = sweep back angle, deg

λ = wave length, m

μ = viscosity, N.s/m^2

μ_p = the dipole moment, debye

ν_{ij} = stoichiometric coefficient of jth species in ith reaction , $\nu_{ij} \equiv \nu''_{ij} - \nu'_{ij}$

$\Omega^{(2,2)*}$	= normalized collision integral for viscosity
ω	= angular frequency, s^{-1}
π	= ratio of circle circumference to diameter
ϕ	= arbitrary fluctuating measure of sound wave
ρ	= density, kg/m^3
σ_{col}	= collision diameter, m
σ_{sym}	= symmetry factor
Θ	= characteristic temperature, K
θ	= momentum thickness, m
τ_{relax}	= relaxation time, s

subscript

diss	value related to dissociation or chemical reactions
e	boundary layer edge value
el	value related to electronic excitation
lami	value at laminar boundary layer
r	value of adiabatic wall (recovery) condition
rot	value related to rotation
tr	value at transition point
turb	value at turbulent boundary layer
vib	value related to vibration
w	wall condition
0	stagnation condition, or undisturbed base condition
∞	values at freestream

superscript

$*$	values evaluated at reference condition, or undisturbed equilibrium condition
$\prime$	fluctuation

Chapter 1 Introduction

1.1 Motivation

The phenomenon that the laminar boundary layer which develops on the surface of a body transitions to a turbulent state has a great importance from the engineering point of view in general. Indeed, transition in pipe flow causes extra total pressure loss or increase in heat transfer, and transition of the boundary layer on an aircraft leads to greater friction drag, which may imply shorter cruise range or less payloads. Besides, the transition phenomena is one of the biggest issues to be understood in fluid dynamics. Furthermore, the accurate prediction of the boundary layer transition in compressible flow is a crucial technology not only for the transport aircraft with high performance but also for the re-entry vehicle, such as the U.S. Space Shuttle, on which the increase of aerodynamic heating caused by the boundary layer transition could be very high. As shown in figure 1.1(a)(heat flux is calculated with a formula by Fay and Riddell[1]), re-entry vehicles generally suffer from severe aerodynamic heating, so that they are eventually designed to keep it at or below the maximum allowable heating rate. As they descend, unit Reynolds number increases monotonically (figure 1.1(b)), leading to transition of boundary layer at some point. Occurence of the transition during maximum heating phase could be disastrous. Indeed, there have been a number of studies devoted in the hypersonic boundary layer transition issue. Some of these investigations are those by Throckmorton[2] and by Zoby[3,4], where the transition Reynolds numbers observed during the U.S. Space Shuttle flights were considerably higher than those obtained from ground facilities. It illustrates our situation that the accuracy in predicting the hypersonic boundary layer transition is not necessarily satisfactory so far. Another example can be Hypersonic Flight Experiment (HYFLEX) in Japan, whose flight data clearly showed an early transition in flight comparing with the prediction based on the ground test results, as reported by Fujii *et al.*[5,6] (see appendix A). They also reported a violent increase in aerodynamic heating associated with the hypersonic boundary layer transition during its maximum heating phase , emphasizing the importance of the establishment of an accurate prediction methodology once again.

Boundary layer stability in compressible flow has distinct characteristics from that in incompressible boundary layer, such as the dominance of higher modes of linear instability known as Mack modes, which were first discovered by Mack[7]. The existence of the modes was confirmed experimentally by Kendall[8]. A brief description of the modes will be given in the following chapter. As the edge Mach number increases, the first mode which corresponds to the Tollmien-Schlichting wave in incompressible flow loses its maximum amplification rate quickly, while the second mode which has the greatest amplification rate among the higher modes takes its dominance at around an edge Mach number of 4 in adiabatic flat plate case. On the other hand, the second mode is known to behave quite differently from the first mode, as pointed out by Mack[7]. From these facts, one can easily expect that the hypersonic boundary layer transition has different characteristics from incompressible or low supersonic transition. Indeed, it has been studied by many researchers experimentally and numerically.

In actual situation when the flow becomes hypersonic such as the flow around a re-entering vehicle, the flow is eventually high temperature flow, or in other words, hypervelocity flow, since total enthalpy can be approximated as $\frac{1}{2}V^2$, where V denotes vehicle velocity. This aspect underlines the importance not only of the high Mach number effect but also the high enthalpy effect on the transition from the engineering point of view. Figure 1.2[9] exhibits schematically when the high enthalpy effect should be considered in the altitude-velocity plane. In the figure, a typical re-entry trajectory and regions in which chemical reactions occurs in the stagnation condition.

In spite of such importance of the high enthalpy effect on boundary layer transition, only a limited number of experimental studies on the issue have been made. One of the earliest experimental studies known by the author was conducted in T4 hypervelocity shock tunnel, University of Queensland, by He and Morgan[10] who investigated the boundary layer on a flat plate at 30 deg angle of attack with air as the test gas. They reported that the transition Reynolds number decreases with increasing total enthalpy in the manner of the effect of wall cooling on the second mode instability under their conditions, which were in the range $5.2 < M_\infty < 6.6$. Some other experimental studies were made by Germain and Hornung[11] in the T5 hypervelocity shock tunnel, California Institute of Technology, using a 5 deg half-angle cone model aiming to eliminate the edge effect which could affect results in a certain condition. They observed that increasing enthalpy had a slight stabilizing effect in terms of the transition Reynolds number evaluated at the boundary layer reference condition, in the case of nitrogen and air. Further experiments confirming the above

results were conducted by Adam and Hornung[12] using the model of the identical configuration with air and carbon dioxide as test gases. They revealed that total enthalpy increase stabilizes the boundary layer dramatically in the case of carbon dioxide.

There have been a number of numerical investigations made on the high enthalpy effect, including those by Malik and Anderson[13] who assumed both thermally and chemically equilibrium air flow, which means the time required for the vibrational excitations and the chemical reactions are assumed infinitesimally short. They found that equilibrium high enthalpy effects stabilize the first mode disturbances and that they, however, destabilize higher modes. Stuckert and Reed[14] considered vibrational equilibrium but chemical non-equilibrium boundary layer flow on a cone at an edge Mach number of 10.6. They found that the chemical non-equilibrium effect stabilizes the boundary layer but not significantly. More recently, Johnson, Seipp and Candler[15] calculated the linear stability of the boundary layer on a 5 deg half-angle cone considering thermal and chemical non-equilibrium effects. Flow conditions of the T5 experiments by Adam and Hornung[12] as mentioned above were simulated in the calculation. Also, it is worth noting that they examined high enthalpy effects on transition through mean flow profile change and disturbance growth separately. They found that reacting mean flow would have larger amplification rate than that when no reaction existed, but that finite relaxation rate causes a net damping effect that is especially marked in carbon dioxide. They also made comparisons of their numerical results with the T5 experimental data and observed a consistent tendency in transition Reynolds number dependence on total enthalpy for both air and carbon dioxide.

This may also be supported by an analysis introduced by Clarke and McChesney[16], who considered effects of relaxation on sound wave propagation in an ideal dissociating gas. They showed that the relaxation in the chemical reaction damps sound waves whose frequency is near the reciprocal of the relaxation time, as will be discussed in the following chapter. This suggests that, depending on the relation between the most strongly amplified frequency in the boundary layer and the frequency of relaxation, the effect of high enthalpy can be quite different. Therefore, it comes into our interest to study transition of a boundary layer where the relation of these two characteristic frequencies is different from that in the above mentioned cone experiments.

1.2 Objectives and Scope of Present Study

As introduced in the foregoing section, the objective of the present study is to broadly examine the novel idea that the sound absorption phenomenon due to high temperature relaxation process would suppress the amplification of linear instability wave which is expected to have acoustic features in hypersonic regime. Along with the context, the experiment has been planned to compare the differences in the effect of high enthalpy on transition Reynolds number between several cases where the two characteristic frequencies differ from each other. A Damköhler number is proposed in this study in order to illustrate the frequency relation quantitatively, which can be approximated as,

$$\frac{1}{\tau_{\mathrm{relax}} f_{2\mathrm{nd}}} = \frac{2\mu^* Re_\delta^*}{\gamma^* M_e^{*2} e^{\left(\frac{K}{T^*}\right)^{1/3}}}$$

where $f_{2\mathrm{nd}}$ is the estimated second mode frequency which has the largest amplification rate, and τ the relaxation time in thermal and/or chemical reaction. The boundary layer on swept cylinder attachment line is therefore chosen for present experiment in order to achieve a large variation of the Damköhler number.

In order to understand the experiments, however, it is first necessary to get acquainted with hypersonic boundary layer stability and its characteristics, and with high temperature relaxation processes. The following chapter 2 will be devoted to briefly describe mechanisms of hypersonic linear stability, high temperature relaxation processes and their consequences, the idea of their interactions from the point of view of effect on the transition, and some specific aspects of attachment line transition. Chapter 3 presents a detailed description on the analysis method for the attenuation rate of sound through high temperature relaxing gases, which is developed along with the present study. Chapter 4 describes the experimental setup for the present experiment. Chapter 5 gives information on the analysis methods carried out in order to clarify the experimental results which appear and be discussed in the chapter 6. Chapter 7 summarizes the present study and what are left for the future work. Appendix A briefly introduce some relevant measurement on Hypersonic Flight Experiment, which attracts the author's attention on the topic of the present study. Relevant parameters of the experiment are shown in the appendix B. Appendix C gives detail descriptions mainly of calculation codes which are used for facility diagnostic data processing. Coefficients of chemical reactions, that of relaxations and tranport properties are given in appendix D.

Chapter 2 Background

2.1 Boundary Layer Transition

Although the mechanics of the boundary layer transition has not been fully understood, recent studies on transition phenomenon, especially a part of non-linear process following the slowly growing linear stability regime, have shed light on the overall picture of the transition process. The general process by which transition is believed to occur in quiet incompressible boundary layer flow past a smooth surface is schematically shown in figure 2.1(White[17]). A similar process is believed to occur for the hypersonic case. Initially, a stable laminar boundary layer exists, followed by the region where waves of particular frequencies become unstable and experience exponential growth when the critical Reynolds number is reached. The unstable waves grow in amplitude to the point that non-linear processes take over and turbulent spots begin to appear before the boundary layer ultimately transitions to turbulence. More recent and detailed picture is given by Herbert[18] or Schmid and Henningson[19]. Figure 2.2 is reproduced from Herbert[18] showing the paths of transition to turbulence schematically. Transition can be understood as a consequence of the nonlinear response of the very complicated oscillator to forcing environmental disturbances. The conversion of environmental disturbances into internalized disturbances is governed by the mechanisms of receptivity. After entrainment of environmental disturbances, several paths of transition are possible, for example, under certain conditions, such as very noisy environment, the response may be spontaneous transition without involvement of known growth mechanisms, known as bypass transition (Path E). Provided environmental disturbance not very strong, other paths are possible, yielding the process of eigenmode growth, such as Tollmien-Schlichting instability or cross flow instability(Path A or B). This eigenmode instability, however, does not directly lead to turbulence, but may saturate to a steady state and establish a new mean flow. This mean flow in turn may become unstable to infinitesimal disturbances. The linear stability with the new modified mean base flow is called secondary instability, which corresponds to 'Parametric Instabilities and Mode Interactions' in figure 2.2. Then, secondary instability structures may break down to turbulence. Transient growth mechanism in the figure is that based on the algebraic instability first discovered

by Landahl[20], and has been shown to be responsible for transition in plane Couette and pipe flow, both of which are stable according to linear stability theory.

In spite of the complicated path to turbulence, it is often reported that relatively simple e^N method predicts transition quite well for T-S dominated boundary layers even in the hypersonic regime. This is because secondary instabilities rise so explosively that the overall length of the transition process is mainly determined by slow linear (primary) instability, Tollmien-Schlichting instability. Considering that linear instability is responsible for the attachment line boundary layer transition even in compressible flow, as reported by Malik[21], one may expect that behavior of attachment line transition can be inferred qualitatively by examining the behavior of linear instability under the condition of the present experiment.

2.2 Linear Stability of Compressible Boundary Layer

A distinct feature of compressible boundary layer stability, especially in the hypersonic regime, is the dominance of the 'higher modes', as predicted by Mack[7]. According to an excellent review by Mack[22], a exploratory study on compressible boundary layer stability was made by Lees and Lin[23], who examined it with temporal two dimensional inviscid linear stability analysis. They first classified all instability waves as, (i)subsonic wave, (ii)sonic wave and (iii)supersonic wave, depending on whether the relative edge Mach number, M_1, is lower than, equal to or greater than unity, where $M_1 \equiv \frac{\bar{u}_e - c_s}{a_e}$, c_s is the phase velocity of the disturbance wave. Then they showed the following major results:

(i) The necessary and sufficient condition for the existence of the neutral subsonic wave is that there is some point $y_s > y_o$ in the boundary layer where,

$$\frac{\partial}{\partial y}\left(\rho \frac{\partial u}{\partial y}\right) = 0,$$

and y_o is the point at which $u = u_e\,(1 - 1/M_1)$. This necessary condition is the generalization of Rayleigh's condition for incompressible flow that there must be a point of inflection in the velocity profile for a neutral wave to exist. The point y_s, therefore, is called the generalized inflection point. The proof of sufficiency given by them requires $\bar{M}$ to be everywhere subsonic, where, $\bar{M}$ is normalized relative Mach number defined as $\bar{M} \equiv \frac{\alpha u + \beta w - \omega}{\sqrt{\alpha^2+\beta^2}} \frac{M_1}{\sqrt{T/T_e}}$.

(ii) A sufficient condition for the existence of an unstable wave is the presence of a generalized inflection point at some $y > y_o$. The proof of this condition also requires $\bar{M}$ to be subsonic.

(iii) If $\bar{M}^2 < 1$ everywhere in the boundary layer, there is a unique wave number α_s corresponding to c_s for the neutral subsonic wave.

Although the Lees-Lin proof for neutral subsonic waves that α_s is a unique function of c_s was dependent on $\bar{M}^2 < 1$, and although Lees and Reshotko[24] mentioned the possibility that α_s may not be unique for $\bar{M}^2 > 1$, no serious consideration was given to the possibility of multiple solutions until the extensive numerical work of Mack[25] brought them to light. The equations for normalized disturbance velocity normal to the wall, $\frac{\hat{v}'}{\tilde{\alpha}\tilde{u}-\omega}$, and pressure, $\frac{\hat{p}'}{\gamma\bar{M}^2}$, can be written as,

$$\frac{\partial^2}{\partial y^2}\left[\frac{\hat{v}'}{\tilde{\alpha}\tilde{u}-\omega}\right] - \tilde{\alpha}^2(1-\bar{M}^2)\left[\frac{\hat{v}'}{\tilde{\alpha}\tilde{u}-\omega}\right] = 0 \tag{2.1}$$

$$\frac{\partial}{\partial y}\left[\frac{\hat{v}'}{\tilde{\alpha}\tilde{u}-\omega}\right] = i\left(1-\bar{M}^2\right)\frac{\hat{p}'}{\gamma\bar{M}^2}. \tag{2.2}$$

Equations (2.1),(2.2) is elliptic for $\bar{M}^2 < 1$, and it is under this circumstance that Lees and Lin proved the uniqueness of α_s. However, when $\bar{M}^2 > 1$, the equation becomes a wave equation, therefore, an infinite sequence of wave numbers that will satisfy the boundary conditions can be expected. Provided α^2 is large enough, solutions for equation (2.1) can be approximated as,

$$\frac{\hat{v}'}{\tilde{\alpha}\tilde{u}-\omega} = \begin{cases} \pm\sin\left[\tilde{\alpha}\int_0^y \sqrt{\bar{M}^2-1}dy\right] & \text{if} \quad y < y_a \\ -i\,e^{-\tilde{\alpha}\int_{y_a}^y \sqrt{1-\bar{M}^2}dy} & \text{if} \quad y > y_a. \end{cases}$$

where, y_a is y where $\bar{M}^2 = 1$. Since $\hat{p}'$ is finite at $y = y_a$, $\frac{\partial}{\partial y}\frac{\hat{v}'}{\tilde{\alpha}\tilde{u}-\omega}$ must approach zero as fast as $\bar{M}^2 - 1$ as y goes to y_a from equation (2.2). Differentiating the approximated solution above with respect to y, the coefficient of sinusoidal function becomes $\sqrt{\bar{M}^2-1}$, implying the required additional factor, $\sqrt{M^2-1}$, must come from the cosine:

$$\cos\left[\tilde{\alpha}\int_0^{y_a}\sqrt{\bar{M}^2-1}dy\right] = 0.$$

Therefore,

$$\tilde{\alpha}\int_0^{y_a}\sqrt{\bar{M}^2-1}dy = \left(n-\frac{1}{2}\right)\pi.$$

The above equation, in fact, demonstrates the nature of an infinite sequence of discrete neutral wave numbers with the phase velocity, c_s, and the existence of higher modes in a hypersonic boundary layer, somewhere in which the relative Mach number, $\bar{M}(y)$, exceeds unity somewhere. It should be noted that the above simple derivation is valid when the wave number, α_s, is large enough, so that this simple theory is not expected to correctly describe the first mode, which has a different origin[22]. As pointed out by Lees and Gold[26], the higher modes are nothing more than sound waves which reflect back and forth between the wall and the sonic line of the relative flow at $y = y_a$ (figure 2.3). The neutral wave above the sonic line travels acoustically as it does in the low supersonic boundary layer, where $\bar{M}(y)$ is below unity everywhere, while that below the sonic line propagates supersonically forming a set of Mach waves reflecting between the sonic line and the wall.

Among the higher modes, the second mode is in general the dominant instability in a hypersonic boundary layer, provided that it is not subject to any cross flow instability or bypass mechanism, as shown by Mack[22]. As the edge Mach number, M_e, increases, the dominant instability mode switches from first mode to second mode. This feature is shown in figure 2.4, which is a viscous instability calculation made by Mack for adiabatic two dimensional flat plate with $Re = 1500$, where $Re \equiv \sqrt{Re_x}$. The figure shows spacial amplification rate, σ, versus boundary layer edge Mach number M_e. In compressible boundary layer, Squire's theorem which states that the most strongly amplified instability wave is two dimensional in incompressible boundary layer flow, does not hold. As shown in the figure, most amplified first mode wave is an oblique wave with an angle between 55 deg and 60 deg depending on edge Mach number. The figure also shows that the first mode amplification rate, σ, decreases with increasing edge Mach number, however, it is the dominant instability mode up to Mach number of approximately 4. When the edge Mach number becomes larger than 4, second mode rises very sharply to take over the dominance in the boundary layer instability. Although the Mach number at which second mode overcomes the first mode instability, is broadly referred as 4 approximately, it can vary depending on several factors. As pointed out by Reshotko[27], second mode can be the dominant instability at a lower Mach number under highly cooled wall condition, since sufficient wall cooling can damp out 1st mode instability completely at any finite Reynolds number as generalized inflection point vanishes, as confirmed numerically by van Driest[28] and, on the contrary, 2nd mode is predicted to be destabilized by wall cooling since second mode has nothing to do with the generalized inflection point. This means that

sufficient wall cooling of hypersonic boundary layer, as is the case with present experiment and with actual environment around reentry vehicles, reduces the edge Mach number at which the switching in the dominant mode occurs. The amplification rate of linear instability also certainly depends on viscosity, and Reynolds number. The characteristics of the second mode viscous instability have been extensively examined by Mack, and he reported that the viscosity always stabilizes second mode instability wave in his conditions examined. This result may suggest lower amplification rate at finite Reynolds number than at infinite Reynolds number *i.e.*, amplification estimated by an inviscid analysis.

Since it is of particular interest to compare the frequency of most amplified instability wave and another frequency which represents relaxation process of high temperature gas as will be discussed later, a simple and useful relation to estimate the second mode frequency, $f_{2\mathrm{nd}}$ referred by Stetson[29] should be written here:

$$f_{2\mathrm{nd}} \approx \frac{u_e}{2\delta}, \tag{2.3}$$

where u_e and δ are external flow velocity and the boundary layer thickness, respectively. This relation, however, is not very accurate, but it is confirmed experimentally[30] to give acceptable accuracy in a wide range of flow condition. This relation seems to represent the physical mechanism of second mode, which is illustrated in figure 2.3, provided that the phase velocity of the wave can be approximated as edge velocity.

2.3 Sound Absorption due to Relaxation

It is known that the speed of sound which propagates through gases consisting of diatomic molecules, in general, can depend on its frequency (See Vincenti and Kruger[31]). This means that the wellknown relation, $a = \sqrt{(\partial p/\partial \rho)_s} = \sqrt{\gamma RT}$, does not always give the exact speed of sound for diatomic gases. This is because the relaxation of rotational and/or vibrational energy modes of the molecule require a finite time and when this relaxation frequency is comparable to sound frequency, the relaxation can affect propagation of sound through altering the effective value of specific heat ratio, γ. Sometimes used to illustrate the relaxation effect are the two limiting speeds of sound, frozen and equilibrium speed of sound, represented by a_f and a_e respectively. Frozen speed of sound corresponds to that for infinitely high frequency, while equilibrium speed of sound to infinitesimally low frequency. Frozen speed of sound is, in general, faster than that of equilibrium.

Not only the speed of sound but also the amplitude of sound is affected by the relaxation process. As Lighthill[32] pointed out, this effect appears as the bulk viscosity in the case when the sound frequency is low enough comparing with the relaxation frequency as is the case in most situations of low speed flow field. For better understanding of the effect due to relaxation, restrict ourselves to such situations where frozen speed of sound is greater than that of equilibrium, *i.e.*, $a_f > a_e$. For instance, relaxation due to internal energy or a endothermic chemical reaction such as dissociation, is the case. Now let a gas particle be compressed suddenly to double its density at $t/\tau = 0$. Pressure is expected to vary as figure 2.5(a), *i.e.*, pressure jumps within infinitesimal time to the 'frozen' value which is higher than that of 'equilibrium' since $\left(\frac{\partial p}{\partial \rho}\right)_f > \left(\frac{\partial p}{\partial \rho}\right)_e$, then decreases (or relaxes) exponentially to the 'equilibrium' value with a certain characteristic time, τ.

When the gas particle oscillating in volume as illustrated in figure 2.5(b), it is relatively easy to understand that the relaxation mechanism results in 'phase-advanced' responce in pressure as shown in figure 2.5(c) and (d), which suppresses kinetic energy, *i.e.*, energy of sound wave is dissipated. When it is in contracting motion, translational energy rises due to adiabatic compression. Relaxation in internal modes or chemical reaction of such kinds, however, makes translational energy higher than in equilibrium case, implying higher pressure, since temperature is directly related to translational energy. In expanding motion, on the contrary, the pressure would be lower than in equilibrium change, meaning a phase-advanced system.

In addition, when the sound frequency is so slow compared with relaxation that internal or chemical energy is always in equilibrium with translation during a cycle, no sound absorption can be expected since no pressure difference exists between contracting and expanding motion. In the opposite situation when the sound frequency is so high that no significant variation in internal energy occurs during a cycle, no pressure difference is expected, either. Thus, one may expect that the maximum absorption takes place at a frequency around the reciprocal of relaxation time as illustrated in figure 2.5(e). The maximum absorption rate depends on the ratio of specific heat ratios of equilibrium and frozen process, which can be represented by the ratio of equilibrium and frozen speed of sound, $\frac{a_f}{a_e}$. Here, the bulk viscosity can be interpreted as a linearized approximation of the relaxation absorption mechanism for a infinitesimally low frequency sound wave.

Although some text books such as Vincenti and Kruger[31] or Clarke and McChesney[16] discuss the absorption with single relaxation mode, such as vibration relaxation of single diatomic species without dissociation or dissociating relaxation of ideal dissociating gas, Fujii and Hornung[33]

proposed a procedure to estimate the absorption rate with multiple modes of relaxation as in the actual high temperature gases (See Chapter 3).

Since the relaxation time is determined by the frequency of collision of molecules, it depends on both temperature and pressure, for instance, higher temperature and higher pressure lead to the shorter relaxation time. Actually, relaxation time in vibration for example, τ_{vib}, can be approximated as[31],

$$\ln \tau_{\mathrm{vib}} = \left(\frac{K}{T}\right)^{1/3} - \ln p + \ln C, \tag{2.4}$$

where, K and C are constants depending on gas species, and T and p is temperature and pressure respectively. The relaxation time of chemical reactions can be in general a matrix of the order of the number of chemical reactions. For simplicity, the relaxation time of dissociation of pure diatomic gas, τ_{diss}, can be defined as,

$$\frac{1}{\tau_{\mathrm{diss}}} = \frac{d}{d\alpha}\left(\frac{d\alpha}{dt}\right),$$

where, α is degree of dissociation defined by,

$$\alpha \equiv \frac{2x_{\mathrm{A}}}{x_{\mathrm{M}} + 2x_{\mathrm{A}}},$$

x_A and x_M is mole fraction of dissociated atom and of diatomic molecule, respectively. Dissociation rate, $\frac{d\alpha}{dt}$, can be approximated by an Arrhenius type expression as,

$$\frac{d\alpha}{dt} = \frac{C_f T^{\eta_f} e^{-\frac{\Theta_f}{T}}}{\rho}\left[(\rho N_M) - \frac{1}{K_{eq}}(\rho N_A)^2\right].$$

If the base condition through which the sound propagates is in equilibrium, the relation can be simplified to,

$$\frac{1}{\tau_{\mathrm{diss}}} = -C_f T^{\eta_f} e^{-\frac{\Theta_f}{T}}\left(\frac{4}{N_A} + \frac{1}{N_M}\right) N_M. \tag{2.5}$$

As expected, the relaxation time both of the vibration and chemical reactions reduces with increasing temperature and pressure.

Considering that relaxation frequency of nitrogen rotation at the standard condition, 1 atm and 298.15 K, is approximately 1 GHz, and that higher temperature makes the characteristic frequency even higher, rotational relaxation in this experiment condition can be taken into account reasonably by the concept of conventional bulk viscosity. However, relaxations of vibration and/or

chemical reactions can have characteristic frequencies comparable with or even lower than the frequency of our interest, which is approximately 1 MHz∼10 MHz. Figures 2.6(a), (b) and (c) show sound absorption rate $\alpha_{\mathrm{relax}}\lambda$ of nitrogen, air(N_2:78.1%+O_2:20.9%+Ar:1.0%) and carbon dioxide, calculated along with the procedure described by Fujii and Hornung[33], taking frequency as the abscissa. Here, absorption rate $\alpha_{relax}\lambda$ is defined as natural logarithm of the ratio of amplitudes per wave length:

$$f = f_0 e^{-\alpha_{relax}\lambda\frac{x}{\lambda}} e^{i(\omega t - ax)}.$$

In the figure, some of the lines have more than one peak absorption, the highest frequency is absorption due to vibrational relaxation, and others are associated with chemical reactions (and some of them with vibration of another molecule produced by a chemical reaction). The maximum absorption rate of air and carbon dioxide at each temperature range, is approximately equal to or even greater than 0.2, which corresponds to damping of as much as 20% down per wave length. As seen in equation (2.4),(2.5) previously, the frequency of maximum absorption increases quickly with increasing temperature. It should be noted that in the case of carbon dioxide, the value of the absorption maximum associated with vibrational relaxation decreases as the temperature becomes sufficiently high, because of dissociation of carbon dioxide molecules.

2.4 Related Previous Investigations at T5 Hypervelocity Shock Tunnel

Since this study was inspired by knowledge obtained at previous experimental studies made at T5 hypervelocity shock tunnel, and was conducted using the facility, a brief summary of related previous investigations made at T5 shock tunnel is to be presented here.

Transition experiments on a 5 deg half-angle sharp cone model were studied in the facility by Germain[34] and Adam[35] to throw light on the high enthalpy effect. In these studies, freestream velocity was approximately 5 km/s, the maximum freestream static temperature was 4000 K and the edge Mach number was between 4.3 $\sim$ 5.9. They plotted the measured transition Reynolds number versus total enthalpy using nitrogen and air as test gases in figure 2.7 (solid symbols). The Reynolds number here is based on distance of transition location from the cone tip and local flow parameters evaluated at Eckert's reference temperature[36]. The major feature in the figure is that

the transition Reynolds number in air increases with total enthalpy and is slightly larger than that of nitrogen. Predicted transition Reynolds number using e^N method (N value was set to 10) based on non-equilibrium linear stability code by Johnson *et al.*[15] is overplotted with open symbols in the figure. The prediction showed the same feature described above for measured data. The major cause of the difference between air and nitrogen case was understood as the existence of oxygen molecule which has lower vibrational and dissociation characteristic temperature.

When carbon dioxide was used as a test gas, since it has even lower vibrational and dissociation characteristic temperatures than oxygen and since it has as much as four vibrational modes, a significant effect of high enthalpy had been expected. In fact, the transition Reynolds number for carbon dioxide varies with total enthalpy by almost a factor of 10 in the enthalpy range where vibrational excitation and dissociation reaction are expected to be significant, as shown in figure 2.8 . These observations support the idea that the non-equilibrium relaxation influences boundary layer transition in high enthalpy flow regime as will be mentioned in the section 2.5.

2.5 A Consideration for Present Study

Since the dominant instability mode in hypersonic boundary layers is the second mode, which can be interpreted as acoustic wave trapped in the boundary layer as described in section 2.2, one may expect that the hypersonic boundary layer has acoustic nature. Malmuth, *et al.*[37] and Fedorov, *et al.*[38] studied this issue numerically and analytically. An experimental study was made by Rasheed, *et al.*[39,40], where the boundary layer transition was measured on 5 deg half-angle sharp cone model with porous surface effective for absorbing sound of frequency in specific range, reporting that the passive control device has a strong effect in delaying transition depending on flow condition. On the other hand, acoustic wave with a certain frequency travelling through high temperature gas is suppressed by relaxation effects as discussed above. One may infer that hypersonic boundary layer transition could be delayed a lot due to relaxation process when two characteristic frequencies are close enough to each other. This inference that sound absorption may influence linear stability is qualitatively supported by the interesting numerical results by Johnson, *et al.*[15] who fictitiously switched the sign of the enthalpy derivative with respect to the degree of dissociation of oxygen (*i.e.*, reaction was switched from endothermic to exothermic). Their numerical result was that this virtual switching leads to a significant destabilization (figure 2.9). Since the magnitude of the sound

absorption rate depends monotonically on $a_f/a_e - 1$, sound waves would be amplified by relaxation processes if the frozen sound speed were slower than the equilibrium sound speed, which was done by the artificial switching. This results indicates at the same time a possibility that a transitional reaction in a complicated dissociation process such as that of poliatomic molecule might have an effect on the sound propagation differently depending on whether each reaction is endothermic or exothermic.

In the aforementioned experiments on 5 deg half-angle sharp cone model in T5, second mode frequency (equation (2.3)) is found to be less than the relaxation frequency (equation (2.4) or (2.5)). Then it is considered below how one can make these frequencies close to each other at the point of transition. The ratio of these frequencies defines a Damköhler number:

$$\frac{1}{\tau_{\mathrm{relax}} f_{\mathrm{2nd}}} = \frac{2\delta}{u_e \tau_{\mathrm{relax}}} \tag{2.6}$$

This expression can be rewritten assuming perfect gas relation in terms of Reynolds number based on boundary layer thickness and edge properties:

$$\frac{1}{\tau_{\mathrm{relax}} f_{\mathrm{2nd}}} = \frac{2\mu^* Re_\delta^*}{\gamma^* M_e^{*2} e^{\left(\frac{K}{T^*}\right)^{1/3}}}, \tag{2.7}$$

where values with superscript $*$ denote values at a representative condition, γ specific heat ratio, μ viscosity. Assuming the transition Reynolds number based on boundary layer thickness is insensitive to geometry of model, equation (2.7) implies that Damköhler number decreases with increasing temperature, T^* or with decreasing edge Mach number, M_e^*. Therefore, a lower Damköhler number than at the previous experiments on 5 deg half-angle sharp cone in T5 is expected achievable by increasing inclination angle of model surface to the freestream, which causes a lower edge Mach number, M_e^*, and higher temperature, T^*. Considering practical restriction such as blockage problem that would arise for sharp cone model with greater half-angle, attachment line boundary layer on a swept cylinder is suitable to investigate, since it yields basically two dimensional linear instability mode as that over sharp cone and the Damköhler number can be altered simply by changing the sweep angle.

So called high enthalpy effects can be divided in two categories as that on boundary layer profile and that on the evolution of disturbance. The former can be accounted for by a linear stability analysis of 'frozen' disturbance through 'non-equilibrium' mean flow profile, such as that

described in appendix C.4. The relevance of sound absorbing phoenomina is, therefore, of a particular interest with respect to the later effect. Effects other than that of relaxation on instability of boundary layer, which is already known in low enthalpy hypersonic or even low speed flow, such as that of freestream noise, edge Mach number, wall temperature, surface roughness, and pressure gradient will be discussed later (section 6.3).

It seems appropriate to describe here the flow field model and assumptions considered in the present study. Both thermally and chemically equilibrium mean flow is considered everywhere downstream of the oblique shock wave formed in front of the model. Boundary layer profile is also implicitely assumed equilibrium in terms of 'reference condition' of equilibrium state, although linear stability analysis is conducted in the basis of perfect gas boundary layer profile, instead. Sound absorption due to relaxation process is, of course, taking thermal and chemical non-equilibrium aspects into account. Reservoir condition is assumed to be thermally and chemically equilibrium, whereas freestream condition is calculated assuming chemical non-equilibrium but thermal equilibrium by a one dimensional nonequilibrium nozzle expanding flow code. The detailed descriptions can be found found in chapter 4 and 5.

2.6 Attachment Line Boundary Layer Transition

It seems appropriate to remind ourselves of some relevant results on attachment line transition reseaches made at regimes of cold hypersonic or supersonic flow, since we will use later the criteria found through these experiments in order to make the high enthalpy effects more visible. As was pointed out earlier, the attachment line boundary layer was chosen for the present study because it provides the opportunity not only to obtain a very different value of the Damköhler number than in the flow over a sharp cone, but also to vary it by changing the sweep angle. But attachment line boundary layer transition, in fact, has been a subject of study for many years from another point of view, such as that of leading edge transition over swept wings of transonic aircraft, especially. To evaluate the transition condition for the attachment line boundary layer over a swept cylinder, the local Reynolds number proposed by Poll[41], $\bar{R}$, which is based on the boundary layer characteristic length, η, and edge velocity in the axial direction, is commonly used in incompressible flow (figure 2.10[41]):

$$\bar{R} \equiv \frac{\rho_e u_e \eta}{\mu_e}.$$

The characteristic length for that Reynolds number is defined as follows,

$$\eta = \sqrt{\frac{\mu_e}{\rho_e \frac{dw_e}{dz}}}. \tag{2.8}$$

Poll[42] also extended this notation to compressible flow by evaluating the density and viscosity in the Reynolds number at a reference temperature in the boundary layer, thus introducing $\bar{R}^*$ as,

$$\bar{R}^* \equiv \frac{\rho^* u_e \eta^*}{\mu^*} = \sqrt{\frac{\rho^* u_e^2}{\mu^* \frac{dw_e}{dz}}},$$

where the reference temperature here is defined by,

$$T^*_{\text{Poll}} = 0.10 T_w + 0.60 T_r + 0.30 T_e. \tag{2.9}$$

Poll[43] reviewed the issue in detail. Many experimental and numerical investigations on attachment line transition in perfect gas flows have been made. Malik and Beckwith[21] conducted linear stability analysis at a freestream Mach number of 3.5, which is followed by another calculation made by Nomura[44]. As for experimental investigations, Benard *et al.*[45] gives a good summary of the literature in this area. Most of them concern the leading edge boundary layer contamination effect due to the turbulent boundary layer which grows along the aircraft fuselage. In such situations, attachment line boundary layers are subject to strong disturbances and transition Reynolds number is, therefore, reported by many investigators as low as $\bar{R}^* \approx 245$. Without conjunction to body or plate at the tip of the cylinder, however, transition is not supposed to occur with smooth surface at the Reynolds number below $650 \sim 750$, as reported by Creel, Beckwith and Chen[46] whose studies were conducted in the low-disturbance supersonic wind tunnel at NASA Langley Research Center. They reported that the Reynolds number $\bar{R}^*$ at which transition occurs on a smooth enough surface is approximately the same value both for 'quiet' and 'noisy' freestream conditions. In hypersonic condition, Murakami, *et al.*[47] made experiments in a Ludwieg tube with freestream Mach number ranging from 5 to 7, and Fujii, *et al.*[48] in a conventional hypersonic wind tunnel with freestream Mach number of 7. Both of them reported that transition occurs with smooth surface and with no strong disturbance upstream at the Reynolds number approximately equal to that observed by Creel, *et.al.* They also reported transition Reynolds number dependence on edge Mach number, as summarized in figure 2.11. As edge Mach number, M_e, increases, transition Reynolds number gradually increases, which qualitatively agree with the flat plate results discussed in section 6.3.

Chapter 3 Sound Wave Propagation Through Relaxing Gases

Attenuation of sound propagating through high temperature relaxing gas has been reviewed in several textbooks such by Lighthill[32], Vincenti and Kruger[31] or Clarke and McChesney[16]. They, however, take single relaxing mode into account, while practical situation such as in the present study has two or even more, both vibrational and chemical. The author has extended the procedure described in textbooks above to multiple relaxing modes. This chapter describes the details of the procedure used in the present study. Example calculations and source code of the procedure can be found in a technical report by Fujii and Hornung[33].

3.1 Estimation of Sound Attenuation Rate for Equilibrium Gas at Rest

The governing equations for this purpose will be set here. Let $\mathbf{q}$ be a vector of non-equilibrium variables measured per unit mass (for example, these could include e_v for vibrational non-equilibrium and/or $\boldsymbol{\alpha}$ for ideal dissociating gas). When the disturbance quantities are denoted with $'$, the governing equations for a small disturbance propagating through gas in equilibrium can be written as,

$$\frac{\partial \rho'}{\partial t} + \rho_o \frac{\partial u_i'}{\partial x_i} = 0, \tag{3.1}$$

$$\rho_o \frac{\partial u_i}{\partial t} + \frac{\partial p'}{\partial x_i} = 0, \tag{3.2}$$

$$\rho_o \frac{\partial h'}{\partial t} - \frac{\partial p'}{\partial t} = 0, \tag{3.3}$$

$$h' = h_{p_o} p' + h_{\rho_o} \rho' + \frac{\partial h}{\partial \mathbf{q}} \mathbf{q}', \tag{3.4}$$

$$\frac{\partial \mathbf{q}'}{\partial t} = \mathbf{A}(\mathbf{q}^{*\prime} - \mathbf{q}'), \tag{3.5}$$

$$\mathbf{q}^{*\prime} = \mathbf{q}^*{}_{p_o} p' + \mathbf{q}^*{}_{\rho_o} \rho', \tag{3.6}$$

where $*$ denotes equilibrium value under the given pressure and density. And $\mathbf{A}$ is a matrix related with the inverse of relaxation time, defined as,

$$\mathbf{A} \equiv -\frac{\partial}{\partial \mathbf{q}} \left(\frac{\partial \mathbf{q}}{\partial t} \right) \qquad \left(\sim \frac{1}{\tau} \right). \tag{3.7}$$

We restrict the discussion to one-dimensional sound propagation. In order to eliminate p' and u', introduce a function ψ from equation 3.2 as follows:

$$p' = -\rho_o \psi_t, \qquad u' = \psi_x. \tag{3.8}$$

Thus, equation 3.1 becomes

$$\frac{\partial \rho'}{\partial t} = -\rho_o \psi_{xx}.$$

Substituting into equation 3.4, we can get

$$-\psi_{tt} = -\rho_o h_{p_o} \psi_{tt} - \rho_o h_{\rho_o} \psi_{xx} + \frac{\partial h}{\partial \mathbf{q}} \frac{\partial \mathbf{q}'}{\partial t}. \tag{3.9}$$

Differentiating equation 3.5 with respect to time, t, and substituting equation 3.6 to eliminate virtual fluctuation of $\mathbf{q}^{*\prime}$ in the equilibrium state, we get

$$\frac{\partial}{\partial t} \left(\frac{\partial \mathbf{q}'}{\partial t} \right) = \mathbf{A} \left\{ -\rho_o \mathbf{q}^*{}_{p_o} \psi_{tt} - \rho_o \mathbf{q}^*{}_{\rho_o} \psi_{xx} - \frac{\partial \mathbf{q}'}{\partial t} \right\}, \tag{3.10}$$

$$\frac{1 - \rho_o h_{p_o}}{\rho_o h_{\rho_o}} \psi_{tt} - \psi_{xx} + \frac{1}{\rho h_{\rho_o}} \frac{\partial h}{\partial \mathbf{q}} \frac{\partial \mathbf{q}'}{\partial t} = 0. \tag{3.11}$$

Assuming the frequencies for the fluctuation vector $\mathbf{q}'$ and ψ to be identical, *i.e.*,

$$\frac{\partial \mathbf{q}'}{\partial t} = \mathbf{f}(x) e^{i\omega t} \tag{3.12}$$

$$\psi = g(x) e^{i\omega t}. \tag{3.13}$$

Then the equations become

$$\frac{1 - \rho_o h_{p_o}}{\rho_o h_{\rho_o}} \omega^2 g - g'' + \frac{1}{\rho h_{\rho_o}} \frac{\partial h}{\partial \mathbf{q}} \mathbf{f} = 0 \tag{3.14}$$

$$(i\omega\mathbf{I}+\mathbf{A})\,\mathbf{f}=\mathbf{A}\left(\rho_o\omega^2 g\mathbf{q}^*_{p_o}-\rho_o g''\mathbf{q}^*_{\rho_o}\right). \tag{3.15}$$

Solving the above equations, the function g can be written in the form

$$g=Ce^{Dx} \tag{3.16}$$

or,

$$\psi=ge^{i\omega t}=Ce^{-\left(\frac{2\pi D_{real}}{D_{imag.}}\right)\frac{x}{\lambda}}e^{i\omega\left(t+\frac{D_{imag.}}{\omega}x\right)}, \tag{3.17}$$

where

$$D=\pm\sqrt{\frac{-\omega^2\left(\frac{1}{a^2_{f_o}}-\frac{1}{h_{\rho_o}}\left(\frac{\partial h}{\partial\mathbf{q}}\right)(i\omega\mathbf{I}+\mathbf{A})^{-1}\mathbf{A}\mathbf{q}^*_{p_o}\right)}{1+\frac{1}{h_{\rho_o}}\left(\frac{\partial h}{\partial\mathbf{q}}\right)(i\omega\mathbf{I}+\mathbf{A})^{-1}\mathbf{A}\mathbf{q}^*_{\rho_o}}}, \tag{3.18}$$

$$a^2_{f_o}=\frac{h_{\rho_o}}{\frac{1}{\rho_o}-h_{p_o}},$$

$$\lambda=\frac{a}{f}=-\frac{2\pi(\omega/D_{imag.})}{\omega}.$$

Both for waves propagating in the positive direction ($-\frac{\omega}{D_{imag.}}>0$) and in the negative direction ($-\frac{\omega}{D_{imag.}}<0$), positive $\frac{D_{real}}{D_{imag.}}$ means damping. To confirm that this result contains the case of a single relaxation mode as a special case, consider the matrix $\mathbf{A}$ to be reduced to $\frac{1}{\tau}$, where τ is the relaxation time. Introducing another relaxation time, τ^+,

$$\tau^+=\frac{\tau\,(h_p-1/\rho)}{h_p+h_q q^*_p-1/\rho},$$

the absorption parameter, D, can be reduced to

$$\begin{aligned}D^2&=-\frac{\omega^2(i\omega\tau^++1)}{i\omega\tau^+a^2_f+a^2_e}\\&=-\frac{\omega^2}{a^2_e}\left[\frac{1+X(\omega\tau^+)^2}{1+X^2(\omega\tau^+)^2}+i\frac{(1-X)\omega\tau^+}{1+X^2(\omega\tau^+)^2}\right],\end{aligned} \tag{3.19}$$

where a_e is the equilibrium speed of sound, which can be written as

$$a^2_e=-\frac{h_\rho+h_q q^*_\rho}{h_p+h_q q^*_p-1/\rho},$$

and X is defined as the square of the ratio of the frozen to the equilibrium speed of sound,

$$X \equiv (a_f/a_e)^2 \,.$$

equation 3.19 is identical to well-known result for the ideal dissociating gas case[16,31]. It should be noted that the sign of $\frac{D_{real}}{D_{imag.}}$, which determines whether relaxation acts as damping or amplifying force, depends on the sign of $1 - X$, *i.e.*, $a_e - a_f$, as can be seen from the sign of the imaginary part of D^2 shown in equation 3.19:

$$\frac{D_{real}}{D_{imag.}} \quad \begin{cases} > 0 & (a_f > a_e) : \text{ damping} \\ < 0 & (a_f < a_e) : \text{ amplifing} \end{cases} .$$

3.2 Definition of Variables and Description of the System

The linearly independent set of chemical reactions can be represented as

$$\overbrace{\sum_{j=1}^{n_s} \nu'_{ij} X_j}^{reactants} \rightleftharpoons \overbrace{\sum_{j=1}^{n_s} \nu''_{ij} X_j}^{products},$$

$$\nu_{ij} \equiv \nu''_{ij} - \nu'_{ij}.$$

Defining a vector $\boldsymbol{\alpha}$, which represents the degree of advancement of the reactions per unit mass (mole/kg), each species concentration, N_j, moles per unit mass of mixture, can be written by $\boldsymbol{\alpha}$ as

$$N_j = \sum_{i=1}^{n_{re}} \alpha_i \nu_{ij} + N_{0j}. \tag{3.20}$$

The vector of non-equilibrium variables, $\mathbf{q}$, can be defined as a combination of $\boldsymbol{\alpha}$ and the vibrational energies per unit mass for the molecular species:

$$\mathbf{q} \equiv \begin{pmatrix} \boldsymbol{\alpha} \\ e_v(1) \\ \vdots \\ e_v(n_s) \end{pmatrix} . \tag{3.21}$$

Since it is necessary to take account of several reaction paths to evaluate the non-equilibrium rate processes properly, a matrix, $\mathbf{R}'$, which represents the relation between the set of linearly independent reactions (n_{r_e}) and the remaining reactions($n_r > n_{r_e}$) can be introduced:

$$\boldsymbol{\nu}^* = \begin{pmatrix} \mathbf{I} \\ \mathbf{R}' \end{pmatrix} \boldsymbol{\nu}. \tag{3.22}$$

where $\boldsymbol{\nu}^*$ is a $n_r \times n_s$ coefficient matrix for all reactions, and $\mathbf{R}'$ is $n_r - n_{r_e} \times n_{r_e}$ matrix. Then, letting $\boldsymbol{\alpha}'$ express the degrees of advancement of reactions $\boldsymbol{\nu}^*$,

$$\boldsymbol{\alpha} = \begin{pmatrix} \mathbf{I} & {}^{\mathrm{t}}\mathbf{R}' \end{pmatrix} \boldsymbol{\alpha}' \equiv \mathbf{R}\boldsymbol{\alpha}'. \tag{3.23}$$

3.3 Calculation of Derivative Values

The pressure and density dependence of the $\mathbf{q}$ in equilibrium can be calculated as follows: In the equilibrium state,

$$K_i(T) = \rho^{\sum_j \nu_{ij}} \prod_j N_j^{*\nu_{ij}}, \tag{3.24}$$

must be satisfied. Using the following form of the equation of state,

$$\frac{dT}{T} = \frac{1}{p}dp - \frac{1}{\rho}d\rho - \overline{M_w} \sum_i (\sum_j \nu_{ij}) d\alpha_i, \tag{3.25}$$

and differentiating the law of mass action (equation 3.24) with respect to T, the following equation can be derived

$$\mathbf{A}_p dp + \mathbf{A}_\rho d\rho - \mathbf{A}_\alpha d\boldsymbol{\alpha}^* = 0,$$

where

$$\mathbf{A}_{pi} \equiv \frac{T}{K_i}\frac{dK_i}{dT}\left(\frac{1}{p}\right)$$

$$\mathbf{A}_{\rho i} \equiv \left[\frac{T}{K_i}\frac{dK_i}{dT}\left(\frac{1}{\rho}\right) + \frac{\sum_j \nu_{ij}}{\rho}\right]$$

$$\mathbf{A}_{\alpha ij} \equiv \left[\frac{T}{K_i}\frac{dK_i}{dT}\overline{M_w}\sum_k \nu_{jk} + \sum_k \frac{\nu_{ik}\nu_{jk}}{N_k}\right].$$

Then, the equilibrium change of the vector $\boldsymbol{\alpha}$ corresponding to given changes in pressure and density can be calculated as follows,

$$d\boldsymbol{\alpha}^* = \mathbf{A}_\alpha^{-1}\mathbf{A}_p dp + \mathbf{A}_\alpha^{-1}\mathbf{A}_\rho d\rho,$$

$$\left(\frac{\partial \boldsymbol{\alpha}^*}{\partial p}\right) = \mathbf{A}_\alpha^{-1}\mathbf{A}_p,$$

$$\left(\frac{\partial \boldsymbol{\alpha}^*}{\partial \rho}\right) = \mathbf{A}_\alpha^{-1}\mathbf{A}_\rho.$$

Similarly, the change in vibrational energy, assuming a harmonic oscillator model is

$$de_{v_i}^* = \frac{de_{v_i}^*}{dT}dT = e_{v_i}^* \frac{\left(\frac{\Theta_{v_i}}{T^2}\right) e^{\frac{\Theta_{v_i}}{T}}}{e^{\frac{\Theta_{v_i}}{T}} - 1} \left\{ \left(\frac{T}{p} + \frac{\partial T}{\partial \boldsymbol{\alpha}}\frac{\partial \boldsymbol{\alpha}^*}{\partial p}\right) dp + \left(-\frac{T}{\rho} + \frac{\partial T}{\partial \boldsymbol{\alpha}}\frac{\partial \boldsymbol{\alpha}^*}{\partial \rho}\right) d\rho \right\},$$

since

$$dT = \frac{T}{p}dp - \frac{T}{\rho}d\rho + \frac{\partial T}{\partial \boldsymbol{\alpha}}d\boldsymbol{\alpha},$$

where, from equation 3.25,

$$\left(\frac{\partial T}{\partial \alpha_i}\right) = -\overline{M_w} T \sum_k \nu_{ik}.$$

In equation 3.18, $\frac{\partial h}{\partial \mathbf{q}}$ as well as h_{ρ_o} and h_{p_o} need to be known. They are calculated under the assumption mentioned before, as,

$$\frac{\partial h}{\partial \rho} = -\sum_{s=1}^{n_s} N_s \frac{T}{\rho}\hat{C}_{v,t+r} - \frac{p}{\rho^2},$$

$$\frac{\partial h}{\partial p} = \sum_{s=1}^{n_s} N_s \frac{T}{p}\hat{C}_{v,t+r} + \frac{1}{\rho},$$

$$\frac{\partial h}{\partial e_{v_i}} = M_{w_i} N_i,$$

$$\frac{\partial h}{\partial \alpha_i} = \sum_{j=1}^{n_s} \left[\nu_{ij}\left(\hat{e}_j + \hat{e}_{0j}\right) - N_j \overline{M_w} T \left(\sum_s \nu_{is}\right) \hat{C}_{v,t+r} \right].$$

The first two equations indicate our assumption of "thermal equilibrium in translation and rotation" and "frozen electronic excitation" in the disturbance wave.

3.4 Relaxation Time

The relaxation time of chemical reaction is related to reaction rate, $\frac{d\boldsymbol{\alpha}'}{dt}$, each of which can be estimated by

$$\rho\frac{d\alpha_i'}{dt} = k_{f_i}\left[\prod_s (\rho N_s)^{\nu'_{i,s}} - \frac{1}{K_i}\prod_s (\rho N_s)^{\nu''_{i,s}}\right], \tag{3.26}$$

where, k_{f_j} is the forward reaction rate coefficient of the form

$$k_{f_j} = C_{f_j} T^{\eta_{f_j}} e^{\frac{\Theta_{f_j}}{T}}. \tag{3.27}$$

The reaction rates for the linearly independent reactions are then derived using equation 3.23, *i.e.*,

$$\frac{d\boldsymbol{\alpha}}{dt} = \begin{pmatrix}\mathbf{I} & {}^{\mathrm{t}}\mathbf{R}'\end{pmatrix}\frac{d\boldsymbol{\alpha}'}{dt} = \mathbf{R}\frac{d\boldsymbol{\alpha}'}{dt}. \tag{3.28}$$

In order to differentiate an arbitrary function (say, f) of species concentration, N_j, with respect to α_i, we can use the following relation from equation 3.20. The reaction rates for the linearly independent reactions are then derived using

$$\begin{aligned}\frac{\partial f}{\partial \alpha_i} &= \sum_j \frac{\partial f}{\partial N_j}\frac{\partial N_j}{\partial \alpha_i} \\ &= \sum_j \nu_{ij}\frac{\partial f}{\partial N_j}.\end{aligned} \tag{3.29}$$

Differentiate equation 3.28 with respect to α_j, using equation 3.29,

$$\frac{\partial}{\partial \alpha_j}\left(\frac{d\alpha_i}{dt}\right) = \sum_k R_{ik}\frac{k_{f_k}}{\rho}\left[\sum_l \left(\frac{\nu'_{kl}\nu_{jl}}{N_l}\right)\prod_s (\rho N_s)^{\nu'_{ks}} - \frac{1}{K_k}\sum_l \left(\frac{\nu''_{kl}\nu_{jl}}{N_l}\right)\prod_s (\rho N_s)^{\nu''_{ks}}\right].$$

When the undisturbed condition is in equilibrium, the above equation can be reduced to

$$\frac{\partial}{\partial \alpha_j}\left(\frac{d\alpha_i}{dt}\right) = -\sum_k R_{ik}\frac{k_{f_k}}{\rho}\left[\sum_l \left(\frac{\nu_{kl}\nu_{jl}}{N_l}\right)\right]\prod_s (\rho N_s)^{\nu'_{ks}}.$$

In the above equation, changes in k_{f_j} and K_k in accordance with temperature changes resulting from $\delta\alpha_i$, *i.e.*, $(\partial K_k/\partial T)(\partial T/\partial \alpha_i)$, are ignored.

The vibrational energy relaxation for species s due to collisions with species r is determined

from the expression given by Millikan and White[49],

$$\ln A_1 \tau_{sr} p = A_2 \mu_{sr}^{0.5} \Theta_{v_s}^{4/3} \left(T^{-1/3} - A_3 \mu_{sr}^{1/4} \right),$$

where μ_{sr} is the equivalent molecular weight between the two species s and r defined $\mu_{sr} \equiv \frac{M_{w_s} M_{w_r}}{M_{w_s} + M_{w_r}}$. p is the pressure, Θ_{v_s} is vibrational characteristic temperature. Constants, A_1, A_2 and A_3 are,

$$A_1 = 9.8625 \times 10^2 \text{ Pa}^{-1}\text{s}^{-1} \qquad A_2 = 0.0367 \text{ kg}^{-1/2}\text{mol}^{1/2}\text{K}^{-5/3} \qquad A_3 = 0.08435 \text{ K}^{1/3}\text{mol}^{1/4}\text{kg}^{-1/4}.$$

The relaxation time of species s is determined by taking the number-weighted average of τ_{sr}:

$$\tau_s = \frac{\sum_r N_r}{\sum_r \frac{N_r}{\tau_{sr}}}. \tag{3.30}$$

where, $N_r$is the number density of species r. Although the Millikan-White formulation gives good agreement with experimental data for the diatomic molecules, the formulation does not hold for carbon dioxide because it predicts three different relaxation times for four vibrational modes while Camac[50] showed experimentally that all four vibration modes of carbon dioxide relax at the same rate. The relaxation time of carbon dioxide vibrational excitation is therefore estimated with following formulation which is independent of collision partner,

$$\ln A_4 \tau_{\text{CO}_2} p = A_5 T^{-1/3},$$

where constants A_4 and A_5 are

$$A_4 = 4.8488 \times 10^2 \text{ Pa}^{-1}\text{s}^{-1} \qquad A_5 = 36.5 \text{ K}^{1/3}.$$

Strictly speaking, the vibrational relaxation time might be a function of concentration. However, it is assumed that this effect of the disturbance wave is small. (Vibrational relaxation time is assumed constant through the disturbance wave at a value evaluated with the undisturbed equilibrium concentration.) Then the matrix $\mathbf{A}$ in equation 3.7 becomes

$$\mathbf{A}_{ij} = \frac{\partial}{\partial \alpha_j} \left(\frac{d\alpha_i}{dt} \right) \quad i, j < n_{r_e},$$

for chemical relaxation, and

$$\mathbf{A}_{ij} = \begin{cases} 0 & i \neq j \\ \frac{1}{\tau_s} & i = j \end{cases} .$$

for vibrational relaxation. Reaction parameters and species parameters required for the above equations can be found in appendix D.

Chapter 4 Experiment

4.1 Facility and Apparatus

4.1.1 T5 Hypervelocity Shock Tunnel

It is commonly recognized that Reynolds number and Mach number have a great importance in studying the flow field around an object which travels through gases with moderate velocity. In order to realize the similarity between the actual flow field such as that around a re-entering vehicle or flying aircraft, and the flow field in laboratory, both parameters should agree in both flow fields. In simulating the flow field of a re-entering object with high velocity, such hypersonic Mach number can be achieved in two ways, *i.e.*, by increasing the flow velocity, or by decreasing the speed of sound. The latter is, in general, the easier way to achieve high Mach number flow from the engineering point of view. Actually, so called conventional hypersonic wind tunnels belong to this kind and are sometimes referred as cold hypersonic facilities. This kind of facilities is wellsuited for the purpose to investigate Mach number effect or Reynolds number effect, however, it does not give a complete similarity to the actual flow field. This is because actual flow field around re-entering object with orbital velocity experiences so high temperature in general that the molecules of the gas can be excited vibrationally, dissociated or even ionized. Since such thermal and/or chemical effects could break up the flow field similarity, it is required to increase flow velocity, *i.e.*, stagnation enthalpy, to achieve the complete similarity or to investigate such chemical and/or thermal effect on flow field.

It is a crucial requirement for the present study to achieve not only high Mach number and high Reynolds number, but also high enough stagnation enthalpy to observe the relaxation effect on transition. A condition of high Reynolds number and high stagnation enthalpy means that both temperature and pressure are very high at the reservoir. Since it is not practically possible to keep gases at such high temperature and high pressure for long time, a facility which can create such flow must be eventually a short duration facility. Shock tunnel, along with this context, is one of such facilities widely used, with which high temperature reservoir condition is realized by a shock wave driven by high pressure gas initially stored at room temperature. The reservoir temperature

obtained by the facility, however, is not necessarily high enough for studies of chemical effects. The T5 hypervelocity shock tunnel, Graduate Aeronautical Laboratories, California Institute of Technology, in which the present study was made, is a free-piston shock tunnel designed to achieve high enough reservoir temperature and pressure (figure 4.1). The key idea of this facility is, as appearing in its name, the piston, which travels through the compression tube (CT) to compress 'driver gas' adiabatically to achieve high temperature and high pressure condition. In a typical shot condition, driver gas temperature can be approximately 4000 K and pressure of 120 MPa. This very hot and dense condition of driver gas makes even faster shock wave than that would be obtained in conventional shock tubes, resulting in higher reservoir temperature and pressure. Shock speed which basically determines stagnation enthalpy ranges up to 5 km/s, and stagnation enthalpy in operational shot conditions ranges from 2 MJ/kg to 25 MJ/kg, stagnation pressure from 10 MPa to 70 MPa when air is used as test gas. More detailed descriptions regarding the T5 operations and performance can be found in literatures by Hornung and Bélanger[51], Hornung, *et al.* [52] and Hornung[53].

In spite of the very high stagnation pressure, it is not always easy to achieve a sufficiently high Reynolds number to get boundary layer transition at high enthalpy, which is crucial for the present study. This is because of lower density and higher viscosity at higher temperature. Indeed, it is expected that the study on boundary layer transition in hypervelocity flow in a facility whose physical size is less than the T5 is more difficult. Even with the size of T5, the maximum Reynolds number is not high enough at very high enthalpy condition in the present experiments. In order to maximize the obtainable Reynolds number, therefore, a 30 mm diameter nozzle throat, which is the largest throat for the facility, is used, except at very low enthalpy cases of carbon dioxide, where a 15 mm diameter throat is used because, in turn, the lower limit in Reynolds number range needed to be extended. In the present experiment on attachment line flow, the transition Reynolds number can be obtained only through varying the freestream flow properties, since the flow is considered as two dimensional, and Reynolds number does not change with distance along the stagnation line. Since the stagnation conditions of the flow must therefore be varied over a wide range to obtain the trend of transition Reynolds number versus total enthalpy, a conical nozzle was used all through the tests so that reasonably good flow quality is obtained. The conical nozzle has an exit diameter of 300 mm, and produces nominal freestream Mach number of 5 with the 30 mm diameter throat.

A typical trace of stagnation pressure measured at the end of shock tube section is shown

in figure 4.2, where approximately constant stagnation pressure is seen for 3 ms at the bottom of the figure. Flow duration is, however, estimated approximately as short as 1 ms for typical condition during which flow quality is good enough for actual measurements. This time duration is determined mainly by two factors, one is the starting process of nozzle flow, and the other is driver gas contamination. After the secondary diaphragm at the end of the shock tube is burst by the incident shock, the high pressure test gas starts to flow through the nozzle throat. A finite time is required to establish a steady flow, and this starting process takes approximately $0.5 \sim 1.0$ ms for typical shot conditions. The testing time starts from the point of the establishment of steady flow and ends up at the point when driver gas, Helium and Argon mixture, arrives in the test section. It had been found by Sudani and Hornung[54] that the time when the driver gas starts to contaminate the flow has a direct relation to the total enthalpy, and it was estimated by an empirical method proposed by them for the present study.

4.1.2 Freestream Properties

It is important in general to know the reservoir condition in hypersonic facilities in order to determine freestream properties. In short duration facilities, however, it is usually difficult to measure stagnation temperature directly, due to the response time of a temperature probe. Stagnation temperature in T5 is, therefore, calculated from measured stagnation pressure and shock wave speed, which is determined from the pressure measurements at several locations in shock tube section, using the chemical and thermal equilibrium code, STANJAN, developed by Reynolds[55] based on the JANAF table[56] (see appendix C.1), since pressure, *i.e.*, density, is so high that equilibrium assumption is well justified. Figure 4.2 also shows pressure traces at known locations in the shock tube section, to illustrate how the shock speed is measured, and figure 4.3 describes assumptions and calculations made here schematically.

Freestream properties are often determined from stagnation properties by calculation of isentropic expansion through the nozzle in 'cold' hypersonic facilities. A problem associated with high enthalpy hypersonic facilities, as is the case here, is the fact that nozzle expanding flow may not be necessarily isentropic. This is because dissociation takes place when two molecules collide, while recombination requires three-body collisions, it means that recombination is more sensitive to density than dissociation. In a nozzle expansion, therefore, a point may be reached where the recombination rate can no longer keep up with the demands put on it by the rate of increase of area.

The recombination rate falls so rapidly in nozzle flow that this transition to non-equilibrium flow is followed fairly closely by a second transition to frozen flow, after which no significant changes of recombination occur anymore. Due to this phenomenon, known as nozzle freezing, chemical non-equilibrium calculation is necessary. A quasi-one-dimensional chemical non-equilibrium nozzle expansion code, NENZF, developed by Lordi *et al.*[57], is used for the purpose in the present study (see appendix C.2). In the calculation, thermal equilibrium is assumed during the expansion. Properties of post-shock, boundary layer edge and reference condition is calculated assuming both chemical and thermal equilibrium.

Pressure gradient due to divergence of freestream produced by conical nozzle expansion may cause some influences on boundary layer transition and Tollmien-Schlichting like instability wave as discussed by Schlichting[58]. Although it is almost impossible to fully assess its effects on transition in the present experiment, figure 4.4 gives some information on the issue from the point of view of pressure gradient dependence on total enthalpy and on species of test gases. This plot of static pressure gradient from NENZF calculation versus total enthalpy, shows no significant dependence either on total enthalpy or species of gases.

To determine Reynolds number, viscosity is needed in addition to other freestream flow properties, such as pressure, density, temperature, velocity and mole fraction of gas species. In an environment of high enough temperature where dissociation and/or other chemical reactions occur, as is the case here, it must be taken into account that viscosity, which can be interpreted as diffusion of momentum, is a function of chemical species and their mole fractions in general. For engineering purpose, a simplified mixing rule is often used to calculate viscosity of a mixture from viscosities of each chemical species, one of the most commonly used is that proposed by Wilke[59], which is used in the present study for evaluation of Reynolds number. A detailed description is given by White[17]. In Wilke's mixing rule, taking μ_s as viscosity of chemical species s at a temperature and a pressure of interest, the viscosity of a gas mixture, μ_{mix}, can be written as,

$$\mu_{\mathrm{mix}} \approx \sum_{i=1}^{n} \frac{\mu_i}{\sum_{j=1}^{n} \phi_{ij} \dfrac{x_j}{x_i}},$$

where,

$$\phi_{ij} = \frac{\left[1 + (\mu_i/\mu_j)^{1/2} (M_{w_j}/M_{w_i})^{1/4}\right]^2}{2^{3/2}(1 + M_{w_i}/M_{w_j})^{1/2}}.$$

This rule can also be interpreted as an approximate form of more general mixing formula discussed by Hirschfelder *et al.*[60]. It has been shown experimentally that Wilke's rule gives a good estimate as long as the collision cross sections of the species involved do not differ from each other too much.

We now need to estimate the viscosity of each chemical species. A curve fit method by Blottner[61] is widely used for experimental and for numerical studies in high temperature gases. That method, however, does not always agree well with Sutherland formula[62] at low temperature, such as the wall temperature in the experiment. Another method, described by Poling[63] is therefore adopted here. From kinetic theory of gases, viscosity of pure gases can be written as,

$$\mu = \frac{5}{16}\frac{\sqrt{\pi m k_B T}}{\pi \sigma_{\rm col}^2 \Omega^{(2,2)*}}, \tag{4.1}$$

where, $\Omega^{(2,2)*}$ is the collision integral for viscosity normalized with that for a rigid sphere model, $\sigma_{\rm col}$ collision diameter, m molecular mass, and k_B Boltzmann constant. This collision integral, $\Omega^{(2,2)*}$, depends on the intermolecular potential. For example, it would reduce to unity with rigid sphere potential, by its definition, and equation (4.1) results in a form proportional to $\sqrt{T}$. When weak attractive intermolecular forces are taken into account in addition to rigid sphere model, as is the case at relatively low temperature condition, the equation gives the Sutherland formula. At high temperature, however, when the average molecule velocity is so fast that the colliding molecules penetrate into each other, the intermolecular potential should take the effect into account. The Lennard-Jones(6-12) model is one of the most frequently used models which does it. The collision integral associated with the potential model can be obtained from kinetic theory, and Monchick and Mason[64], for example, tabulated the collision integral. A correlation made by Neufeld *et al.*[65] with the exact calculation is used in the present study to calculate the viscosity of pure gas which is expected to be valid through the temperature range of interest. The correlation is,

$$\Omega^{(2,2)*} = A(T^*)^{-B} + Ce^{-DT^*} + Ee^{-FT^*} + \frac{0.2\delta^{*2}}{T^*},$$

where, $A = 1.16145, B = 0.14874, C = 0.52487, D = 0.77320, E = 2.16178, F = 2.43787$ $T^* \equiv \frac{k_B T}{\varepsilon_{pw}}$, $\delta^* \equiv \frac{\mu_p^2}{2\varepsilon_{pw}\sigma_{\rm col}^3}$. It is reported that the deviation of this from the exact solution is less than 0.06% within the range in normalized temperature, T^*, of $\delta^* \equiv \frac{\mu_p^2}{2\varepsilon_{pw}\sigma_{\rm col}^3}$. Properties such as ε_{pw}, $\sigma_{\rm col}$, μ_p for each species are presented in appendix D.

4.1.3 Models and Instrumentation

Swept Cylinder models with sweep angle of 45 deg and 60 deg are tested to obtain a wide range in the Damköhler number defined by equation (2.7). The configurations of models, shown in figure 4.5, were determined considering following three aspects. The first is large enough L/D (length to diameter ratio) to realize the two dimensional attachment line flow assumption, the second, small enough to fit the core flow in the test section, and the last, large enough diameter for boundary layer transition because Poll's Reynolds number is related to diameter through η. As a result, the models, as shown in figure 4.5, have diameters of $D = 50.19$ mm, $D = 50.8$ mm and lengths of $L = 402.6$ mm, $L = 305.3$ mm for $\Lambda = 60$ deg model and $\Lambda = 45$ deg model, respectively. The models were made of grade o-1 oil-hardening drill rod, since the relatively high inclination surface may be contaminated by dust which is believed to flow through the nozzle with quite high velocity after the test time. Model arrangement in the test section of T5 is sketched in figure 4.6.

Boundary layer transition in the hypersonic regime in general is accompanied by increase in aerodynamic heating in the same manner as increase in wall shear stress. The detection of the transition, therefore, has been accomplished by measuring the heat flux to the attachment line and by comparing it with theoretical value of laminar and turbulent heat flux. Among many methods to measure heat flux in short duration facilities, measurement with in-house made co-axial thermo-couples developed by Sanderson[66] and evaluated by Davis[67] is regularly used in the T5 hypervelocity shock tunnel, considering the severe environment of T5 flow. In the present study, also, co-axial thermo-couples made in the same manner were used to measure heat flux. The thermo-couple contains two parts: an outer constantan jacket with 2.38 mm outer diameter, 0.80 mm inner diameter and 3.05 mm height, and a chromel inner wire with thin insulation layer to the outer piece (as shown in figure 4.7). These two pieces have a so thin contact to make Type E thermo-couple with a typical response time of 1 μs for surface temperature measurement. The models have coaxial thermo-couples on and off the attachment line and aerodynamic heating is deduced from surface temperature traces assuming one-dimensional heat conduction. The cold junction of the thermo-couple is on the back side of the co-axial thermo-couple, in order to minimize electric noise by reducing resistance. No reference junction compensation was attempted because the test time is so short in the present experiments, that thermal penetration depth during the test time is estimated even less than 0.1 mm.

The co-axial thermo-couples are, however, re-installed after every 20∼30 shots typically, because they are contaminated by impacts of dust after the test duration whose velocity could be of the order of a kilometer per second. The depth of dents is measured typically 0.02∼0.03 mm before re-installation, which corresponds to $k/\eta^* \approx 0.1 \sim 0.5$. The critical roughness height which Creel *et al.*[46] and Murakami *et al.*[47] reported at a lower edge Mach number condition is larger than the above measurements, so that the surface is thought aerodynamically smooth.

4.2 Measurement

4.2.1 Facility Diagnostic Data and Data Acquisition System

In order to acquire sufficient information for determination of freestream quantities, stagnation pressure, shock speed and initial shock tube quantities are measured. The facility diagnostic instrumentation consisted primarily of PCB piezo-electric fast response pressure transducers (PCB119M44) located along the length of the facility (See figure 4.8). Two redundant transducers ($P_{0,\mathrm{North}}$ and $P_{0,\mathrm{South}}$) were located diametrically opposite each other on the shock tube at a distance of 47 mm from the shock tube end wall to measure the stagnation pressure in the reflected shock region. The rising signal of P_0 triggers the Data Acquisition System to start recording and time $t = 0$ in the present study corresponds to this trigger. Two more transducers (ST_3 and ST_4) were located at 2.38 m and 4.78 m from the shock tube end wall and were used to calculate the shock speed (u_{shock}). Another two redundant transducers ($P_{4,\mathrm{North}}$ and $P_{4,\mathrm{South}}$) were located in the compression tube just upstream of the primary diaphragm in order to measure the diaphragm burst pressure. Additional diagnostic instrumentation consisted of two linear voltage displacement transducers (LVDT) to measure the tunnel recoil.

The high speed data acquisition system consisted of three CAMAC-standard crates from DSP Technology capable of sampling 60 channels at 12-bit resolution. A schematic diagram of the system is shown in figure 4.9. The first crate housed a GP-IB crate controller module (CC-488), the trigger generator (Model 1024), an in-house manufactured laser controller and eight digitizer channels that were on four independently controlled digitizer modules (Model 2612). These were used exclusively for facility diagnostic instrumentation. The other two crates housed the remaining 52 channels on 26 digitizer modules (Model 2860), 52 amplifiers (Model 1402E), the GP-IB crate

controllers (CC-488), the system controllers (Model 4012A/4032A) and memory modules (Model 5200/5204). Each of these crates had a total throughput of 8 MSamples per second that was available entirely for model instrumentation. The data acquisition system was controlled using software developed in-house and run on a Sun workstation.

Signals from the co-axial thermo-couples on the models are amplified, digitized and recorded with 200 kHz sampling rate and 12 bit resolution. The recorded signal is converted to temperature off line by spline interpolation of reference table of emf(electro motive force) to temperature relation[68].

4.2.2 Aerodynamic Heating

The heat flux to a surface, in general, can be determined from the time resolved temperature traces, if boundary and initial conditions are known. Assuming that heating takes place to infinitely deep and homogeneous material one dimensionally, *i.e.*, uniform heating, and assuming no initial temperature distribution, the aerodynamic heating to the model's surfaces were calculated. There are some practical methods for the reduction, such as 'Direct method' outlined by Schultz and Jones[69], in which the rate of change of temperature is integrated in time to obtain heat flux:

$$\dot{q}(t) = \sqrt{\frac{\rho_M C \kappa}{\pi}} \int_0^t \frac{dT(\tau)}{d\tau} \frac{d\tau}{\sqrt{t-\tau}}.$$

Another method referred as 'Indirect method', on the contrary, is to integrate temperature and to obtain the time history of integrated heat, Q[70]:

$$Q(t) = \sqrt{\frac{\rho_M C \kappa}{\pi}} \int_0^t \frac{T(\tau)}{\sqrt{t-\tau}} d\tau.$$

Rewriting in discrete finite difference form yields,

$$Q(t) = \sqrt{\frac{\rho_M C \kappa}{\pi}} \sum_{i=1}^{n} \frac{T(t_i) + T(t_{i-1})}{\sqrt{t_n - t_i} + \sqrt{t_n - t_{i-1}}} \left(t_n - t_{n-1}\right).$$

Heat flux is, then, obtained by differentiating the above integrated heat, Q:

$$\dot{q}(t_n) = \frac{dQ(t_n)}{dt} = \frac{1}{40(t_n - t_{n-1})}(-2Q_{n-8} - Q_{n-4} + Q_{n+4} + 2Q_{n+8}).$$

One of the advantages of the indirect method is that integrating before differentiating effectively smoothes the computed heat transfer rate. For the present experiments, therefore, the indirect method was used to obtain aerodynamic heating. Thermal properties, $\rho_M C\kappa$, which is required for semi-infinite one dimensional heat conduction, was given as the averaged value for constantan and chromel, since Davis[67] concluded that the average would give good results for typical conditions such as heat flux and time scale in T5 experiments. The calculation is, then, conducted taking $\sqrt{\rho C\kappa} = 8919$ J/m^{2}Ks$^{0.5}$.

4.3 Theoretical Heat Flux on Attachment Line

It is crucial in the present experiment for determining the boundary layer state to compare the measured heat flux to the attachment line with reference heat flux which corresponds to turbulent or laminar boundary layer, since attachment line boundary layer is essentially two dimensional so that the heat flux distribution does not show the transition process. As for the reference heat flux, Beckwith and Gallagher[71] showed theoretical relations for turbulent and laminar attachment line boundary layers which is verified by many experimental results in cold hypersonic flow:

$$St_{lami} = \frac{\dot{q}_{lami}}{\rho_\infty u_\infty (h_0 - h_w)} = (2\gamma)^{-1/4} Pr^{-1} \sqrt{\frac{\mu_e}{\mu_\infty} \frac{1}{R_\infty M_\infty}} \left[\frac{T_\infty}{T_e} \frac{p_e}{p_\infty} \left(\frac{p_e}{p_\infty} - 1 \right) \right]^{1/4} \tag{4.2}$$

$$St_{turb} = \frac{\dot{q}_{turb}}{\rho_\infty u_\infty (h_0 - h_w)} = R_{D,\infty}^{-1/5} Pr^{-2/3} \left(a \frac{\mu_w}{\mu_0} \frac{T_\infty}{T_w} \frac{p_e}{p_\infty} \right)^{4/5} \sin^{3/5} \Lambda \left(\frac{49}{376} \frac{\mu_0}{\mu_\infty} \frac{dw}{dz} \frac{D}{u_\infty} \right)^{1/4}, \tag{4.3}$$

where, $a = 0.0228$. It should be noted, however, that the above relations are derived and verified under the perfect gas assumptions so that their accuracies is not necessarily very good in the high enthalpy condition such as those in the present experiments. These values, therefore, are used just as reference values for the purpose of determining the boundary layer state.

4.4 Test Condition

A total of 78 shots with carbon dioxide, 39 shots with air and 55 shots with nitrogen were carried out in the present experiment. Pure nitrogen has simple relaxation modes both vibrationally and chemically, and has the relatively high characteristic temperatures both of vibration and of dissociation. The effect of relaxation for the case of pure nitrogen is therefore not expected to be strong

until the total enthalpy is very high. For carbon dioxide, however, there are four vibrational modes whose characteristic temperatures are quite low compared with those for oxygen and nitrogen, and also there are a lot of chemical relaxation processes. Based on these facts, carbon dioxide is expected to provide high enthalpy effects at lower total enthalpy than air or pure nitrogen.

At a low total enthalpy condition, stagnation pressure needs to be almost at the lowest limit of T5 to achieve low enough Reynolds number, while as total enthalpy increases, stagnation pressure must increase to keep Reynolds number approximately constant, since higher temperature lowers density. At some point, therefore, stagnation pressure, P_0, is required even higher than the facility limitation to make the boundary layer go turbulent. This occurs at a total enthalpy of approximately 15 MJ/kg for all test gases in the present experiment.

Table 3.1 shows relevant parameters in the present experimental condition. The table indicates that for 60 deg sweep angle, dissociation at the boundary layer edge is expected to be small at the total enthalpy, $h_0 \leq 15$MJ/kg for nitrogen, and $h_0 \leq 5$MJ/kg for carbon dioxide. The Mach number at the boundary layer edge, M_e, is seen to be $3.2 \sim 3.4$ for both cases with 30 mm throat, and $3.2 \sim 3.7$ with 15 mm throat. On the other hand, the degree of dissociation for 45 deg sweep angle cases becomes significant at relatively lower total enthalpy, due to higher temperature at the boundary layer edge. Edge Mach number for 45 deg sweep angle case is even lower than that for 60 deg sweep angle case, which is in a range of $2.1 \leq M_e \leq 2.4$. The stagnation, freestream, edge and reference conditions for all the shots are summarized in appendix B.

One of the consequences of the relatively low edge Mach numbers is a possibility that the responsible instability mode to the boundary layer transition can be altered from second mode to first mode. The dominant instability mode of boundary layers on a flat plate or a sharp cone is known to be the second mode with an edge Mach number greater than 4 when the wall is insulated as shown in figure 2.4, and the oblique first mode when it is lower than 4. Although the edge Mach number in the present experiment is estimated to be below 4 for both sweep angle models as shown in figure 4.10, it should be noted that the edge Mach number at which the second mode takes its dominance from the first mode must be lowered by wall cooling as Reshotko[27] suggested, because amplification of the first mode is weakened by cooling. For example, sufficient wall cooling stabilizes the first mode completely at any finite Reynolds number as the generalized inflection point vanishes, and on the contrary, the second mode is destabilized by wall cooling. In fact, the wall temperature in the present experiment, which rises only of the order of 10$\sim$100 K due to

very short test time, is effectively very cold compared with the total temperature, with a ratio of approximately 0.05 for typical conditions. Therefore, under such very highly cooled wall condition in the present experiment, no unstable first mode was detected according to the two dimensional inviscid linear instability analysis described in a later section.

Such highly cooled conditions can bring another consequence. Due to relatively low edge Mach number, $M_e \approx 2 \sim 3$ as noted above, and due to the highly cooled condition, the temperature profile in the boundary layer takes a maximum value at the edge and the temperature decreases monotonically with y. In such a situation, equation (2.9) for reference temperature underestimates the effect of the wall temperature, and gives much higher temperature than any actual temperature in the boundary layer. Since viscosity, Reynolds number or any quantities calculated based on the temperature then does not seem to have a physical meaning any more, it was decided to use Eckert's reference enthalpy condition[36] instead, even in the calculation of attachment line Reynolds number, $\bar{R}^*$. Eckert's reference enthalpy is written as,

$$h^*_{\text{Eckert}} \equiv \frac{1}{2}(h_e + h_w) + 0.092u_e^2. \tag{4.4}$$

This reference condition, as Dorrance[72] pointed out, can be recognized as a condition at which the Chapman-Rubesin parameter takes the averaged value, which is an important parameter in determination of compressible boundary layer profile. In this sense, the reference enthalpy condition is a representative condition of a compressible boundary layer. Quantities at the reference condition were calculated from the enthalpy described by equation (4.4) and pressure at the boundary layer edge, assuming both chemical and thermal equilibrium.

Chapter 5 Data Analysis

Many relevant quantities including reservoir condition, freestream condition, and boundary layer edge condition must be determined numerically in the present experiment from the limited measurable quantities due to the extreme environment created by the facility. The methods in which flow properties are estimated have been described in the foregoing chapter. However, Damköhler number defined by equation 2.6, amplification of linear instability, and sound absorption rate due to relaxation process are to be compared with measured transition Reynolds number, each of which must be estimated numerically. Figure 5.1 shows a schematic diagram of data analysis from the measurable data such as P_0, V_{shock} and surface temperature trace to the resultant quantities. In this section, the estimation methods for the most strongly amplified frequency, absorption rate due to relaxation process, and amplification of linear instability will be described.

5.1 Most Strongly Amplified Frequency

As discussed in chapter 2, the most strongly amplified frequency is expected to play an important role in the mechanisms of high temperature boundary layer transition. The frequency can be approximately estimated by equation (2.3), in which boundary layer thickness and edge velocity are required. Since the boundary layer thickness is affected by so-called real gas effects, it was estimated by a non-equilibrium boundary layer code, BLIMPK (Boundary Layer Integral Matrix Procedure with Kinetics options, see appendix C.3 for more detailed description). This code has been first developed by Bartlett and Kendall[73] and extended to include surface reactions by Tong, Buckingham, and Morse[74]. A brief input guide for the latest version of BLIMPK can be found in Murray[75] and application to the T5 hypervelocity shock tunnel condition was discussed by Adam[76]. This code is capable of dealing with multiple and various chemical species, reactions, and frozen, equilibrium, and finite reaction rate processes under the planar or axisymmetric two dimensional boundary layer assumption. The restriction that the maximum number of nodal points in the boundary layer calculation is as little as 15 points seemed acceptable for the purpose of estimation of boundary layer thickness, but not for the instability analysis. The boundary layer thickness

is taken as that at which velocity reaches 99 % of the edge velocity, δ_{99}, for the estimation of most strongly amplified frequency. The boundary layer was calculated with non-equilibrium, fully catalytic surface and surface reactions which had been used by Chen *et al.*[77]. It is worth noting that, especially in carbon dioxide, a wall temperature of 300 K does not necessarily guarantee 100 % mole fraction of carbon dioxide according to the possible surface reactions. This means that the wall enthalpy, h_w, (and therefore the reference enthalpy, see equation 4.4) is higher than if carbon dioxide were recombined 100%.

In order to apply BLIMPK, a basically two dimensional code, to a three dimensional boundary layer calculation, Cook's[78] brilliant concept of the 'axisymmetric analogy' was used. In this analogy, the three dimensional boundary layer is approximated by an axially two dimensional boundary layer whose external streamlines spread at the same rate as those of the actual three dimensional case. This approximation is strictly only justified when the boundary layer has no cross flow, unlike the case of the present experiment. Because of its simplicity and theoretical justification for weak cross flow situation, the approximation has been widely used in many engineering aspects, including aero-thermal predictions of re-entry vehicle performance done by DeJarnette *et al.*[79]. The boundary layer thickness, δ_{99}, was therefore determined by BLIMPK code with the spreading rate of external streamline corresponding to that on the attachment line. The spreading rate is estimated from the modified Newtonian pressure distribution as Rakich and Mateer[80] reported for the attachment line boundary layer on a swept cylinder as

$$r_{\text{axis}} = r_0 e^{\frac{k_{ax} x}{r_0}},$$

where r_{axis} represents radius at the station of interest, i.e., spreading rate, r_0 initial radius, and $k_{ax} \equiv \frac{x}{u}\frac{\partial w}{\partial z}$=const.

5.2 Absorption Due to Relaxation Process

It is definitely desirable to examine linear stability taking relaxation effects into account as Hudson *et al.*[81] and Johnson *et al.*[15] did. For simplicity, however, relaxation effects and linear instability were examined separately in the present study. Absorption due to relaxation process was estimated in a representative condition of the boundary layer, *i.e.*, Eckert's reference condition was chosen. Although a full explanation for the estimation of sound absorption rate is available in the report

written by Fujii and Hornung[33] or in Chapter 3, only a summary of the assumptions made in the estimation will be described here. In the calculation, several assumptions were made such as, that the base condition through which sound propagates is both chemically and thermally in equilibrium, and that sound wave (i) is equilibrium in translation and rotation, (ii) has finite relaxation time in vibrational excitation and in chemical reactions, and (iii) is frozen at equilibrium base condition in electronic excitation. Bertolotti[82] reported in his relatively low temperature hypersonic stability analysis, that non-equilibrium in rotation is well approximated by bulk viscosity with appropriate value, as expected. At higher temperature, since the relaxation time must be even shorter, conventional bulk viscosity approach is expected to give good results, see Mack[22].

5.3 Inviscid Perfect Gas Linear Instability Analysis

Boundary layer profile calculated with BLIMPK code consists profile of mole fractions of each species as well as velocity and temperature. In order to examine linear stability of frozen disturbances with the non-equilibrium base flow profile, algorithm for perfect gas was modified to take the effect of variation in mole fraction into account, which is described in appendix C.4. However, the profile obtained from BLIMPK code has so coarse grid that the linear stability analysis does not give reliable results. Instead of using BLIMPK profile, the profile was calculated assuming perfect gas relation with edge Mach number and constant specific heat ratio throughout the boundary layer with the value at the edge condition in equilibrium, and perfect gas linear stability was examined. Perfect gas profile of attachment line boundary layer was obtained with the method described by Reshotko and Beckwith[83]. Inviscid linear stability was analyzed with the method described by Mack[22]. The temporal inviscid growth rate of a disturbance wave which travels in the direction of the cylinder axis was examined assuming perfect gas. The components in the chordwise direction of all gradients of mean flow quantities were neglected in the instability analysis. Due to the very highly cooled wall, only the higher modes are found unstable for all shot conditions examined, as noted previously. Since the analysis is based on perfect gas, two-dimensional, inviscid, linear stability theory, neither the frequency nor the growth rate of the most strongly amplified disturbance may be necessarily accurate. Indeed, the frequency for the most strongly amplified disturbance estimated with equation 2.3 is approximately 2$\sim$3 times higher than the peak frequency of the inviscid linear instability disturbance obtained here. One major cause is that the perfect gas boundary layer calculation results a thicker boundary layer than the BLIMPK calculation (*i.e.,* 'real gas'

calculation) does by a factor of 1.5∼2. Nevertheless, the above inviscid linear stability results give the correct order of magnitude for both the maximum amplification rate and the peak frequency, which is sufficient for our purpose here.

Chapter 6 Results and Discussion

This chapter describes the results obtained from the present experiment and some considerations on the results. It first describes measured heat flux distributions and the method of determining the boundary layer state. Total enthalpy effects on the transition observed in the present experiment are then presented and compared with numerical estimation of boundary layer stability. A possible explanation for the novel observed trend in total enthalpy effect on transition is then discussed in conjunction with the edge Mach number effect comparing with the previous 5 deg half-angle cone results.

6.1 Laminar and Turbulent Heat Flux

Figures 6.1, 6.2, 6.3 show typical heat flux traces measured at sensor #9, $x/r \approx 10$ on the attachment line of the 60 deg sweep model , where x is coordinate along attachment line whose origin locates at the upstream tip of the model and r represents radius of the cylinder (See also figure 4.5). The time $t = 0$ corresponds to the pressure rise in the stagnation region of the shock tube as measured by the pressure transducers $P_{0,\mathrm{North}}$ and $P_{0,\mathrm{South}}$. The high heat flux period at the beginning of each shot, which lasts approximately up to 1 ms, corresponds to the starting process during which the steady nozzle flow is established. The test time is then taken as the time between the end of the starting process and the onset of driver gas contamination, which is determined by an empirical correlation as indicated by a set of dashed vertical lines in the figures. The heat flux averaged during the test time is compared to the predictions for laminar and turbulent values, which are from equations 4.2 and 4.3 respectively and correspond to the two dashed horizontal lines in each figure (b), in order to determine the boundary layer state. As illustrated in these figures, the measured heat flux can be categorized in three types of behavior. In the first type, as represented by figure 6.1, the heat flux is almost constant at a value close to the theoretical laminar heat flux after the high heating period due to starting process. In the second type, as represented by figure 6.3 the initial heat flux spike corresponding to the nozzle starting process is not distinguishable from the following high steady heat flux whose value is close to the theoretical turbulent value.

In the third type the heat flux trace fluctuates intermittently between the laminar and turbulent theoretical predictions (figure 6.2). To detect the transition Reynolds number as accurately as possible, freestream conditions were planned basically by means of adjusting the stagnation pressure so that these three types of the boundary layer states occur equally. These three situations are reasonably inferred to correspond to laminar, turbulent and transitional attachment line boundary layer respectively.

Since the aspect ratio of the models in this experiment is not necessarily as long as those in other studies on attachment line transition in order to achieve high enough Reynolds number, two dimensionality in the heat flux distribution is one of the major concerns. Typical heat flux distributions are also shown in the figures 6.1(b), 6.2(b) and 6.3(b), indicating fairly constant distribution around the point $x/r \approx 10$, following a higher but decreasing heating portion which suggests the boundary layer on growing. The boundary layer state is then examined at the location of $x/r \approx 10$ where the two dimensionality assumption is expected valid.

6.2 Total Enthalpy Effect on Transition

6.2.1 60 deg Sweep Angle Model

The Poll's Reynolds number of the 60 deg sweep model attachment line boundary layer, $\bar{R}^*$, for every shot is plotted versus freestream total enthalpy in figure 6.4. Since the attachment line boundary layer does not grow along the cylinder axis, the data for a particular shot condition can only show whether the boundary layer is laminar or turbulent, and do not give the transition Reynolds number directly. We can thus conclude that the transition Reynolds number lies somewhere between the open symbols and the solid symbols, which represent laminar and turbulent boundary layer, respectively. Symbols with '+' mark indicate that the state is intermittent, that is, transitional. Figure 6.4(a) indicates that the transition Reynolds number $\bar{R}^*_{tr}$ for the nitrogen tests lies between $600 \sim 700$, which is approximately the same value as that observed in a supersonic quiet wind tunnel experiment made by Creel *et al.*[46] (they reported transition Reynolds number as $\bar{R}^*_{tr} = 650 \sim 750$), and no significant dependence on total enthalpy can be seen through the range from 2 MJ/kg to 15 MJ/kg. The air data, figure 6.4(b), show a slightly higher transition Reynolds number than the nitrogen data, and once again, there appears to be no dependence on the total enthalpy. For

the carbon dioxide data (figure 6.4(c)), on the other hand, some features can be clearly observed. Namely, the transition Reynolds number increases rapidly with total enthalpy from $\bar{R}^* \approx 600 \sim 700$ at $h_0 \approx 1 \sim 2$ MJ/kg, to $\bar{R}^* \approx 1000$ at $h_0 \approx 7$ MJ/kg. It does not increase further for total enthalpy higher than approximately 7 MJ/kg or even decreases slightly with total enthalpy. The transition Reynolds number dependence on the total enthalpy is similar to that obtained in the previous 5 deg cone experiments in T5, although a clear saturation of transition Reynolds number for carbon dioxide tests could not be seen in the cone experiments.

Since various factors can affect boundary layer transition as described in a later section, it is needed to assess variations of other parameters and their effects when the influence of a particular parameter, total enthalpy in this case, is to be examined. The edge Mach number variation is shown in figure 4.10 with carbon dioxide. The edge Mach number varies from 3.2 to 3.8 throughout the 60 deg sweep experiments. According to the results of other researchers[46,47] on attachment line transition in low total enthalpy conditions, the transition Reynolds number increases with edge Mach number. However, the edge Mach number is seen to decrease with increasing total enthalpy for carbon dioxide case. This indicates that a dominant effect other than that of edge Mach number exists in the present experiment condition.

One might also be curious to see if the effect of the wall temperature ratio T_w/T_0 can be an alternative explanation. This effect, however, cannot explain the trends in transition Reynolds number for the carbon dioxide case with the 60 deg sweep model. Indeed, the wall-to-stagnation temperature ratio shown in figure 6.5, in which the wall temperature is taken to be constant at 300 K, indicates only a small variation with different test gas used. The slight difference in the temperature ratio with carbon dioxide from the other gases comes from the larger specific heat at constant pressure, C_p, for carbon dioxide. Furthermore, the temperature ratio decreases less with increasing total enthalpy for carbon-dioxide than for air or nitrogen, while the observed trend in transition Reynolds number is opposite.

It might give a good insight into high enthalpy effect issue to estimate the sound absorption rate at the temperature of the reference condition, which represents an average condition in the boundary layer as mentioned before. The sound absorption rate per wave length, $\alpha_{relax}\lambda$, at reference enthalpy condition, is therefore calculated at the frequency estimated as most strongly amplified (equation 2.3), provided that the second mode is the dominant instability, and shown in figure 6.6. In the case of carbon dioxide, the figure clearly shows the similarity between the

trend of absorption rate and that of the transition Reynolds number with total enthalpy. The sound absorption rate increases rapidly with total enthalpy up to about 7 MJ/kg, and after that, it becomes nearly constant or even decreases slightly. This becomes clear from figure 2.6, showing that the maximum absorption frequency due to the vibrational relaxation of carbon dioxide increases as the temperature increases. When it reaches 2000 K, which corresponds roughly to a total enthalpy of 5∼6 MJ/kg in this test situation, the absorption takes its maximum approximately at the frequency of our interest, 1∼10 MHz. However, higher temperature causes carbon dioxide to begin to dissociate and the relaxation effects to remain roughly constant or even to decrease. Relaxation due to chemical reactions, on the other hand, is calculated to have such a low peak absorption frequency that one may not expect it to have significant importance in the transition.

For the nitrogen case, the absorption rate due to relaxation is quite weak compared with that in carbon dioxide, which is also consistent with the measured trend in transition Reynolds number. It comes from the fact that, for nitrogen, the vibrational excitation and dissociation become important at higher temperatures than in carbon dioxide. For the air experiments, the expected absorption rate is higher than in the nitrogen case. However, the magnitude is not significant. This is because the oxygen molecule is more easily vibrationally excited than nitrogen and the absorption peak frequency is closer to the most strongly amplified frequency, although the mole fraction of oxygen is relatively small, and it has only one vibrational mode compared with four in carbon dioxide.

Although the trends of absorption rate due to relaxation and of the transition Reynolds number with total enthalpy are quite similar, one might have a question about the relative magnitude of the absorption rate to the amplification rate of linear instability as a function of frequency. To compare these approximately, an inviscid two-dimensional temporal linear stability analysis was carried out assuming perfect gas flow for both the mean flow profile and the disturbances. Amplification rates per cycle for several representative cases among nitrogen, air and carbon dioxide shots are shown by solid symbols in figure 6.7 together with absorption rate per wave length (open symbols). According to the analysis, no unstable first mode exists in any conditions examined, and the unstable disturbances shown in the figure are those from the second mode instability. For carbon dioxide (figure 6.7(c)), the absorption rate due to vibrational relaxation of CO_2 is quite strong compared with the amplification rate of the second mode instability without chemistry for the mid-enthalpy conditions (shot 2046 : $h_0 = 5.9$ MJ/kg). In contrast, for a lower enthalpy condi-

tion (shot 2035 : $h_0 = 1.9$ MJ/kg), since the two characteristic frequencies are completely different, *i.e.* the Damköhler number (equation 2.6) is very low, absorption may not be expected to affect transition significantly. At even higher total enthalpy condition (shot 2216 : $h_0 = 15.6$ MJ/kg), the absorption peak passes the second mode frequency, and additionally, the peak absorption value itself is getting weaker due to CO_2 dissociation. At this point, we should remember that the instability analysis conducted here gives only approximate values for peak frequency because of the perfect gas assumption in the mean flow calculation. Nevertheless, we can see in figure 6.7 that the sound absorption rate mainly due to the vibrational relaxation of carbon dioxide at the estimated second mode frequency is not negligible compared with the second mode amplification rate. The large transition delay observed in the carbon dioxide tests, thus, can be consistently explained by the effect of vibrational relaxation of carbon dioxide, supposing the second mode instability to be still responsible. The fact that no significant dissociation of carbon dioxide is expected at a total enthalpy below 5 MJ/kg as shown in table 3.1 also supports the important role of vibrational relaxation on the observed transition trend.

On the other hand, nitrogen sound absorption due to vibrational relaxation has its peak so far from the most strongly amplified frequency estimated by inviscid linear stability, that we might not expect any effect of relaxation on linear disturbance growth according to this figure. Air cases are basically similar to nitrogen cases, except that oxygen vibration causes a slightly stronger absorption effect. These results also support the observed trend in transition Reynolds number.

6.2.2 45 deg Sweep Angle Model

The Poll's Reynolds number, $\bar{R}^*$, for the test results with 45 deg sweep angle are shown versus freestream total enthalpy in figure 6.8. For all gases, no significant feature in transition Reynolds number is recognized except several faint features including an increase around a total enthalpy of 15 MJ/kg in carbon dioxide. The rest of the transition Reynolds numbers lie between 700 and 800, which is the same order of magnitude as in cold hypersonic results as mentioned before. Although detecting transition Reynolds number from the limited data points in the figure leads to considerable error, it can be derived from them that transition Reynolds number has no significant dependence on freestream total enthalpy nor on gas species.

At first sight, this result, which shows a very weak total enthalpy effect, is somewhat

unexpected, because the absorption rate at the second mode frequency, as shown in figure 6.9, is estimated to be even stronger than for 60 deg sweep angle for all the tests. Especially for the carbon dioxide case, the absorption rate due to relaxation is estimated to have great importance at even lower total enthalpy than in the 60 deg sweep model cases. Besides, the absorption rate is estimated to have quite different values depending on gas species, while observed transition Reynolds number shows no dependence on species, either.

The amplification rate per cycle from linear instability mechanisms is calculated assuming perfect gas two-dimensional disturbance once again and is plotted versus disturbance frequency in figure 6.10. Even at this low edge Mach number, no unstable first mode disturbances were calculated because of the very highly cooled wall condition. The amplification rate of the second mode is, however, much lower due to the lower Mach number. Remembering that the inviscid analysis is likely to underestimate the second mode growth rate because of the viscous effect, absorption due to relaxation, which is even stronger than the 60 deg cases, was expected to have a stronger effect on the second mode growth rate.

In summary, evaluating the sound absorption rate based on the boundary layer reference condition gives a good qualitative prediction of the effect on transition of total enthalpy variation and effect of test gases with the edge Mach number kept approximately unchanged, but it does not account well for the effect of edge Mach number variation. This disagreement between the qualitative prediction and the observation with respect to edge Mach number becomes more evident when the results in the previous 5 deg cone experiments are compared with the present results as shown in the next sub-section.

6.2.3 Comparisons with 5 deg Half-angle Cone Model

Boundary layers developing on a sharp cone yields two dimensional linear instability, which is also responsible to attachment line transition on a swept cylinder, so that a consistent trend could be extracted by comparing the results obtained here with the previous cone experiments. Since the laminar boundary layer thickness on a cone is roughly proportional to $\sqrt{\mu_e x/\rho u_e}$, the variation in Reynolds number based on wetted length from the cone tip cannot be compared directly with the dependence on Reynolds number based on boundary layer thickness, such as Poll's Reynolds number, $\bar{R}^*$. To compare the results of the previous 5 deg cone experiments with the present studies,

momentum thickness Reynolds number at the transition point were reproduced using the BLIMPK code for both experiments. Figure 6.11 shows the variation in momentum thickness Reynolds number evaluated at reference condition at the transition point in the 5 deg half-angle cone experiments conducted by Rasheed[39] versus Damköhler number $1/\tau_{\mathrm{relax}} f_{\mathrm{2nd}}$ defined by equation (2.6) taking characteristic relaxation time τ_{relax} as that in vibrational excitation of nitrogen or carbon dioxide. The figure clearly indicates a strong effect of relaxation on transition Reynolds number, which increases by a factor of 3 as the characteristic relaxation frequency reaches the second mode frequency (Damköhler number approaches to unity).

Results of the present experiment are shown in figure 6.12 in terms of momentum thickness Reynolds number versus Damköhler number evaluated with vibration of nitrogen, oxygen and carbon dioxide molecule for nitrogen, air and carbon dioxide test cases respectively. Accounting for the fact that edge Mach number in the 5 deg cone experiment is approximately 5, while those on the 60 deg and 45 deg sweep models are 3 and 2 respectively, a comparison with the cone results reveals a consistent trend that transition delay due to relaxation becomes less evident as edge Mach number decreases. This trend means the "unexpected" results that the transition delay becomes less evident as the two characteristic frequencies become closer, *i.e.*, as the Damköhler number approaches unity.

This unexpected result especially for the 45 deg sweep model has not been explained by the author. However, one possibility is that due to the relatively low edge Mach number ($M_e \approx 2.1 \sim 2.4$, see figure 4.10), the finite Reynolds number might make the first mode unstable and responsible for transition, in spite of the very high wall cooling. Because the relaxation process is not expected to affect vorticity wave propagation involved in first mode disturbances, as we might see by an analogy with the bulk viscosity effect, this could explain the absence of significant total enthalpy dependence at the lower edge Mach number case. Another possibility is that the lower edge Mach number is expected to restrict the relative supersonic region where the second mode is trapped only to the vicinity of the wall, while the location where sound absorption rate was calculated remains approximately the same (relatively close to the boundary layer edge). If so, the temperature at which absorption should be evaluated might be much lower than that of the reference condition, and it would weaken the estimation of the relaxation effect a lot. These possibilities remain to be examined in the future.

It is important to realize that the mechanism of transition delay by relaxation claimed in the

present study suggests the possibility of so called 'high enthalpy effects' on transition in hypersonic flow that are quite different from those observed here. As mentioned above (equation 2.3), the most strongly amplified frequency of the second mode instability wave without chemistry can be basically determined only by edge velocity and boundary layer thickness, while sound absorption effects depend additionally on representative temperature (for magnitude and frequency) and pressure (for frequency). These parameters might have quite different values, depending on freestream conditions, angle of attack, wall temperature and geometry. The Damköhler number proposed here could provide a rough estimate for the appearance of relaxation effect on boundary layer transition.

6.3 Limitations of the Experiment

As in most experimental studies, there are several limitations to the overall experiment which should be addressed here. The present experiment has been conducted in the T5 hypervelocity shock tunnel as described earlier, which creates hypersonic freestream with high stagnation enthalpy, and yields some difficulties in specific aspects due to its extraordinary environment. One of the major practical restrictions in measurements is soot particles flowing after test time with a velocity as fast as 5 km/s typically. This situation does not allow to use any sensitive devices such as hot wire in the facility. Additionally, very high velocity leads to very high frequencies of unstable modes of the order of 1$\sim$10 MHz in the boundary layer, and therefore it is difficult to detect either velocity fluctuation or surface pressure fluctuation of such high frequency. Since a stability experiment in such high enthalpy flow is not attainable for that reason, only transition experiments are possible using relatively durable heat flux sensors with short response time. Transition experimental data are, however, sometimes difficult to interpret, because many parameters may be interrelated with each other, as Stetson[29] pointed out.

Boundary layer transition is a complicated process affected by a numbers of factors. It is therefore essential in interpreting transition data to be aware which parameters have major influences on transition and how the major parameters can affect transition or growth rates in linear processes, without relaxation. Along with reviews made by Stetson *et al.*[84], Stetson[29], and Reshotko[27], the major known parameters on transition in cold hypersonic boundary layer are summarized below:

(i.) Freestream noise and its spectrum

Since freestream noise establishes the initial disturbance amplitude to the linear instability growth mechanism, it is generally recognized to affect transition significantly. However, as Stetson[29] suggested, not all freestream disturbances are important to boundary layer transition, *i.e.* the critical freestream disturbances are believed to be those of the same frequency as the boundary layer disturbances responsible for transition. It is then important to identify the dominant instability mode and the amplitude of freestream disturbances at the same frequency. Also, one should be aware especially in a parametric study that both amplitude and spectrum of freestream disturbances can vary with other flow parameters.

(ii.) Edge Mach number

Higher edge Mach number suppresses the maximum growth rate in hypersonic boundary layers, according to Mack's calculations[22]. As expected from this result, transition Reynolds number obtained experimentally by Beckwith *et al.*[85] increases as the boundary layer edge Mach number increases (see figure 6.13).

(iii.) Wall-temperature/total-temperature ratio

It is known that wall cooling stabilizes incompressible boundary layer through the temperature dependence of viscosity for air. Compressible boundary layers, however, have an additional mechanism, *i.e.*, wall cooling alters density profile so that generalized inflection is weakened. Supposing that the cooling is sufficient, it causes complete stabilization of first mode disturbances at any finite Reynolds number according to van Driest's calculation[86]. However, second mode disturbances are expected to be destabilized by wall cooling theoretically.

(iv.) Surface roughness

Experimental results of roughness effect on transition are well reviewed by Reda[87]. Roughness dominated attachment-line transition Reynolds number obtained experimentally by Poll[41,88] and Flynn[89] are correlated in terms of the critical roughness Reynolds number and the correlation suggests critical roughness height would be $k/\eta \approx 1$, which is much higher value than in the present experiment although their results are for incompressible flows.

Critical roughness height (the height below which roughness has no aerodynamic influences to boundary layer transition) depends strongly on the edge Mach number. Braslow[90] reported that it increases with edge Mach number and that even in the low hypersonic regime, it can be as high as the boundary layer thickness.

(v.) Pressure gradient

Favorable pressure gradient is found to stabilize two dimensional instability disturbances in incompressible boundary layer both experimentally and theoretically (Schlichting[58]). In hypersonic boundary layer, Kimmel *et al.*[91] made an experimental study on axisymmetric body at a freestream Mach number of 8 and found same trend in pressure gradient effect on transition.

In the present experiment, each effect has been assessed at least qualitatively except (i) the freestream noise issue. Explanation or description for (ii)edge Mach number effect, (iii)wall temperature ratio effect can be found in section 6.2.1, and effects of (iv)surface roughness, and of (v)pressure gradient respectively in section 4.1.3, section 4.1.2.

A major issue related to the limitations that remains unexplained is then the lack of knowledge of the noise spectrum radiated by the nozzle wall boundary layer in T5, since the tunnel noise level is known to have a strong effect even on the trend of transition Reynolds number, as discussed recently in the review by Schneider[92]. Davis[67] has made pressure fluctuation measurements in T5 shock tunnel with fast response pressure transducers. However, the frequency of the responsible disturbance for transition is estimated 1∼10 MHz which is too high to capture for any available pressure transducer suitable for use in the aggressive environment of T5. Another attempt was made by Adam[35] by measuring transient heat flux fluctuation to the 5 deg half angle cone without using relatively slow response amplifiers. But no fruitful information could be extracted due to large noise level compared to weak signals. The author can then only assume the noise level in T5 to be of order 3% in pitot pressure fluctuation, as He and Morgan[10] measured in T4, a similar shock tunnel to T5, at relatively low frequencies (hundreds of kHz), although a limited measurement of pressure fluctuation in the T5[67] does not show the large peak of unknown origin which is the dominant fluctuation in the T4 measurement. At this time, neither the noise level in the T5 freestream at the frequencies of the most strongly amplified disturbances nor the dependence of the noise spectrum on the total enthalpy are known.

In addition to above mentioned factors, other uncertainties exist in experiments at high enthalpy conditions, *i.e.*, those in flow parameters such as species concentrations, degree of chemical and/or thermal non-equilibrium and so on. Althogh these accuracies are not neccesarily very good, these are not believed to alter the observed qualitative trend in transition Reynolds number significantly. When considering atmospheric flight conditions where gas of the freestream stays in

equilibrium state, one might doubt if the results obtained here is applicable to flight condition. Provided that boundary layer edge conditions are estimated equilibrium as was the case in the present experiment at least, the trend observed here is believed to hold.

6.4 Summary

This section is to clarify what the results of the present experiment mean and what can be inferred from them when the previous T5 transition experiments by Germain[34], Adam[35] and Rasheed[39], are taken into account under the above limitations. First, since the observed transition delay with total enthalpy in carbon dioxide case cannot be explained by the known edge Mach number effect, it suggest another effect than of the Mach number. Considering the significant difference in transition delay between test gases used and little variation in wall temperature ratio as shown in figure 6.5, it becomes clear that wall temperature ratio does not have an important role in the transition Reynolds number variation with total enthalpy in the present experiment. Since pressure gradient in freestream of conically diverging flow which is expected to affect transition has no significant dependence either on total enthalpy or on test gas species as shown in figure 4.4, it is not likely to affect total enthalpy dependence of transition specifically in the experimental condition. Surface roughness height measured in the present experiment is less than the value reported as critical in cold supersonic and hypersonic experiments at relatively 'cold' condition conducted by Creel *et al.*[46], Murakami *et al.*[47] and Fujii *et al.*[48]. For freestream disturbances, no data have been measured in this experiment, however, compiling experiments on attachment line transition from quiet supersonic environment to conventional hypersonic facility by the above mentioned researchers, freestream turbulence does not seem to affect transition strongly at their condition. Taking into account that transition Reynolds number observed at 60 deg sweep model with carbon dioxide is even higher than the value of the quiet tunnel test and that those of all other cases in the present experiment show approximately the same value of cold flow condition, it can be concluded that the freestream environment variation due to variation in total enthalpy alone cannot provide full explanation for the observed transition delay with total enthalpy. The following statements can thus be drawn from the present results with reasonable certainty:

(a) High total enthalpy causes a significant delay in transition Reynolds number at 60 deg sweep model with carbon dioxide in the present experimental condition, which is qualitatively the

same trend observed in the previous experiment made with 5 deg cone in the T5 shock tunnel.

(b) The delay in transition Reynolds number due to high enthalpy appears stronger as the edge Mach number increases. With 45 deg sweep model, no distinguishable effect has been found.

Comparing the experimental results with linear stability analysis assuming perfect gas and with estimations of sound absorption rate due to high temperature relaxation, the followings may reasonably be inferred:

(c) The absorption rate due to relaxation calculated at a typical condition where transition is delayed a lot with carbon dioxide show a very similar trend in total enthalpy with observed transition Reynolds number, and are of the same order of magnitude with amplification rate due to perfect gas linear instability. This suggests that the high enthalpy effect of delaying transition at the present experimental conditions comes mainly from the absorption due to relaxation process of sound wave disturbances which travels through the boundary layer. Relaxation in vibrational excitation of carbon dioxide molecules is calculated to have a much stronger effect than that in chemical reactions in the present condition.

(d) The reason why the effect of total enthalpy on transition appears to be quite different with respect to the Damköhler number defined by equation 2.6, when the edge Mach number decreases sufficiently is thought to be that the acoustic second mode loses its dominance as the edge Mach number decreases. Since the first mode is a vortical disturbance, relaxation processes are not expected to affect it significantly.

The possibility (d) remains to be examined in the future probably numerically rather than experimentally because of the difficulties mentioned before.

From the engineering view point, the physical mechanism of instability in a hypersonic boundary layer claimed in the present study could appear differently depending on the Damköhler number with which a good "rough" estimation method could be drawn in high enthalpy region, where massive numerical computations would be otherwise required to tell whether a boundary layer under a particular condition is stable or unstable. Hypersonic bounadry layer transition is subject not only to Reynolds number, Mach number and other flow parameters but also to the Damköhler number which represents the frequency ratio.

Chapter 7 Conclusions

An exploratory experiment was performed on high enthalpy effects on transition of the hypersonic boundary layer that develops on the attachment-line of swept cylinders using nitrogen, air and carbon dioxide as test gases in the T5 hypervelocity shock tunnel, Graduate Aeronautical Laboratories, California Institute of Technology. Previous experiments of transition on a sharp cone showed significant effects of high enthalpy. This series concerns how the total enthalpy effect varies when conditions of the boundary layer are altered in temperature and edge Mach number. Another objective of the present study is to examine the effect with respect to ratio of most strongly amplified frequency in the boundary layer and the characteristic frequency of absorption by relaxation processes.

A Damköhler number which represents the frequencies ratio was proposed to characterize high enthalpy effects on hypersonic boundary layer transition. Of particular interest is the question how the relaxation in chemical reactions and/or vibrational excitation affect the hypersonic boundary layer transition when these have characteristic frequencies which are quite different from those in the previous cone experiments. Therefore, swept cylinder models whose sweep angles are 45 deg and 60 deg, have been chosen for the experiment. The observed trend of transition Reynolds number with enthalpy, which is found to be similar to that in the cone results, shows strong transition delay at the larger sweep angle for carbon dioxide, while no significant effect is observed in nitrogen or air where transition Reynolds number has approximately the same value as that obtained in experiments by other researchers including supersonic quiet tunnel data although the reference condition is calculated slight differently accounting for the extremely high temperature condition in the present experiment.

The acoustic wave absorption rate due to relaxation at the most strongly amplified frequency calculated at the reference enthalpy condition shows a quite similar trend in enthalpy dependence to transition Reynolds number for the carbon dioxide case. This suggests that the dominant factor for the delay in the boundary layer transition in the carbon dioxide case is vibrational relaxation. A linear inviscid stability analysis was also carried out assuming perfect gas both for the boundary

layer mean profile and for disturbances. The comparisons between the magnitude of the strongest amplification rate and the absorption rate due to relaxation processes show that they are of the same order of magnitude for carbon dioxide and that absorption is not significant for nitrogen or air, which supports the above understanding of the effect of relaxation on transition.

On the other hand at the smaller sweep angle, no significant effect in the trend of transition Reynolds number with enthalpy was observed even for carbon dioxide. In short, estimation of the absorption rate due to relaxation gives a good qualitative prediction of the dependence of transition Reynolds number on total enthalpy, but not of its dependence on edge Mach number. Re-examining the previous 5 deg half-angle cone experiments in terms of momentum thickness Reynolds number and comparing them with the present results, it becomes clear that the high enthalpy effect on transition loses its significance consistently as the edge Mach number decreases. This result suggests that another unknown effect is active at these lower edge Mach number cases. One of the possibilities is that the first mode, which is not expected to be affected by relaxation process, takes its dominance as edge Mach number decreases. Another is an underestimate of the effective temperature for the evaluation of relaxation effect in the boundary layer.

Acknowledgements

I would express my deepest gratitude to Professor Hans G. Hornung who not only gave me a chance to push back the frontiers of knowledge in some extent but also showed what a fun it is to think out and to examine one's own novel idea, in another word, to be curious, a primitive desire of human beings. I would also express my special acknowledgement to Dr. Kenichi Rinoie who made valuable suggestions and advices on the thesis. I believe that his such keen comments and massive endeavor to make the thesis better is an essential part in the thesis. I owe an acknowledgment to Professor Takashi Abe, Professor Etsuo Morishita, Dr.Kojiro Suzuki and Dr.Kimiya Komurasaki for their valuable comments and suggestions. I would like to thank Adam Rahseed who patiently showed me about T5, a complicated and violent facility, which often makes troubles as well as innovative scientific data and with whom I had many valuable discussions. I must acknowledge Bahram Valiferdowsi for everything he did, who has not only been a valuable friend but also helped me a lot during the present experiment with his ideas, knowledge and muscle. I would like to acknowledge all the people either in NAL or in GALCIT who supported me in many ways, physically or mentally, directly or indirectly, including Iwao Kawamoto and Yasutoshi Inoue who allowed me to come and to spend two years for this present research. I would also like to thank Norikazu Sudani who suggested me to start this project and gave valuable discussions, as well as Shigeya Watanabe who has always encouraged and guided my research activities. Finally, I am grateful forever to my wife Miwa and my daughter Nao who have been always encouraging me to challenge in the world of aerodynamics and providing pleasure of life.

Bibliography

[1] J. Fay and F.R. Riddell. Theory of stagnation point heat transfer in dissociated air. *Journal of the Aeronautical Sciences*, 25(2):73–85, February 1958.

[2] D.A. Throckmorton. Benchmark determination of shuttle orbiter entry aerodynamic heat-transfer data. *Journal of Spacecraft and Rockets*, 20(3):219–224, 1983.

[3] E.V. Zoby. Comparisons of STS-1 experimental and predicted heating rates. *Journal of Spacecraft and Rockets*, 20(3):214–218, 1983.

[4] E.V. Zoby. Analysis of STS-2 experimental heating rates and transition data. *Journal of Spacecraft and Rockets*, 20(3):232–237, 1983.

[5] K. Fujii and Y. Inoue. Aerodynamic heating measurement on afterbody of hypersonic flight experiment. *Journal of Spacecraft and Rockets*, 35(6):736–741, 1998.

[6] K. Fujii, S. Watanabe, T. Kurotaki, and M. Shirouzu. Aerodynamic heating measurements on nose and elevon of hypersonic flight experiment vehicle. *Journal of Spacecraft and Rockets*, 38(1):8–14, 2001.

[7] L.M. Mack. Linear stability theory and the problem of supersonic boundary-layer transition. *AIAA Journal*, 13(3):278–289, 1975.

[8] J.M. Kendall. Wind tunnel experiments relating to supersonic and hypersonic boundary-layer transition. *AIAA Journal*, 13(3):290–299, 1975.

[9] C.F. Hansen and S.P. Heims. A review of the thermodynamic transport, and chemical reaction rate properties of high-temperature air. Technical Report NACA TN-4359, National Advisory Committee for Aeronautics (NACA), July 1958.

[10] Y. He and R.G. Morgan. Transition of compressible high enthalpy boundary layer flow over a flat plate. *The Aeronautical Journal*, 98(971):25–34, 1994.

[11] P. Germain and H.G. Hornung. Transition on a slender cone in hypervelocity flow. *Experiments in Fluids*, 22:183–190, 1997.

[12] P. Adam and H.G. Hornung. Enthalpy effects on hypervelocity boundary layer transition: Ground test and flight data. *Journal of Spacecraft and Rockets*, 34(5):614–619, 1997.

[13] M.R. Malik and E.C. Anderson. Real gas effects on hypersonic boundary-layer stability. *Physics of Fluids A*, 3(5):803–821, 1991.

[14] G. Stuckert and H. Reed. Linear disturbances in hypersonic, chemically reacting shock layers. *AIAA Journal*, 32(7):1384–1393, 1994.

[15] H.B. Johnson, T. Seipp, and G.V. Candler. Numerical study of hypersonic reacting boundary layer transition on cones. *Physics of Fluids*, 10(10):2676–2685, October 1998.

[16] J.F. Clarke and M. McChesney. *The Dynamics of Real Gases.* Butterworths, 1964.

[17] F.M. White. *Viscous Fluid Flow.* McGraw-Hill, Inc., second edition, 1991.

[18] T Herbert. Progress in applied transition analysis. AIAA Paper 96-1993, 1996. 27th AIAA Fluid Dynamics Conference, June 17-20, New Orleans, LA, USA.

[19] P.J. Schmid and D.S. Henningson. *Stability and Transition in Shear Flows.* Springer-Verlag, 2001.

[20] M.T. Landahl. A note on an algebraic instability of inciscid parallel shear flows. *Journal of Fluid Mechanics*, 98(2):243–251, 1980.

[21] M.R. Malik and I.E. Beckwith. Stability of a supersonic boundary layer along swept leading edge. In *Fluid Dynamics of Three-Dimensional Turbulent Shear Flows and Transition*, AGARD CP-438, pages 3–1 – 3–9, 1988.

[22] L.M. Mack. Boundary-layer stability theory. In *Special Course on Stability and Transition of Laminar Flow*, AGARD Report Number 709, 1984.

[23] L. Lees and C.C. Lin. Investigation of the stability of the laminar boundary layer in a compressible fluid. Technical Report NACA TN-1115, National Advisory Committee for Aeronautics (NACA), 1946.

[24] L. Lees and E. Reshotko. Stability of the compressible laminar boundary layer. *Journal of Fluid Mechanics*, 12:555–590, 1962.

[25] L.M. Mack. Stability of the compressible laminar boundary layer according to a direct numerical solution. AGARDograph 97, Part I, pages 329–362, 1965.

[26] L. Lees and H. Gold. Stability of laminar boundary layers and wakes at hypersonic speeds: PartI. stability of laminar wakes. Technical Report GALCIT memo, California Institute of Technology, 1964.

[27] E. Reshotko. Boundary layer instability transition and control. AIAA Paper 94-0001, 1994. (32nd Aerospace Sciences Meeting and Exhibit, January 10-13, Reno, NV, USA).

[28] E.R. van Driest and C.B. Blumer. Boundary-layer transition at supersonic speeds: Roughness effects with heat transfer. *AIAA Journal*, 6(4):603–607, 1968.

[29] K.F. Stetson. Hypersonic boundary-layer transition. In J.J. Bertin, J. Periaux, and J. Ballmann, editors, *Advances in Hypersonics: Volume I, Defining the Environment*, pages 324–417. Birkhäuser Boston, 1992.

[30] K.F. Stetson, E.R. Thompson, J.C. Donaldson, and L.G. Siler. Laminar boundary layer stability experiments on a cone at Mach 8. Part IV: On unit reynolds number and environmental effects. AIAA Paper 86-1087, 1986. (4th Fluid Mechanics, Plasma Dynamics and Laser Conference, May 12-14 Atlanta, GA, USA).

[31] W.G. Vincenti and C.H. Kruger. *Introduction to Physical Gas Dynamics.* Krieger Publishing Company, 1965.

[32] M.J. Lighthill. Viscosity effects in sound waves of finite amplitude. In G.K. Batchelor and R.M. Davies, editors, *Surveys in Mechanics*, pages 250–351. Cambridge University Press, 1956.

[33] K. Fujii and H.G. Hornung. A procedure to estimate the absorption rate of sound propagating through high temperature gas. Technical Report FM 01-4, GALCIT, California Institute of Technology, 2001.

[34] P. Germain. *The Boundary Layer on a Sharp Cone in High-Enthalpy Flow.* PhD thesis, California Institute of Technology, 1994.

[35] P. Adam. *Enthalpy Effects on Hypervelocity Boundary Layers.* PhD thesis, California Institute of Technology, 1997.

[36] E.R.G. Eckert. Engineering relations for friction and heat transfer to surfaces in high velocity flow. *Journal of the Aeronautical Sciences*, 22:585–587, August 1955.

[37] N.D. Malmuth, A.V. Fedorov, V. Shalaev, J. Cole, and A. Khokhlov. Problems in high-speed flow prediction relevant to control. AIAA Paper 98-2995, 1998. (2nd Theoretical Fluid Mechanics Meeting, June 15-18, Albuquerque, NM, USA).

[38] A.V. Fedorov, N.D. Malmuth, A. Rasheed, and H.G. Hornung. Stabilization of hypersonic boundary layers by porous coarings. *AIAA Journal*, 39(4):609–610, 2001.

[39] A. Rasheed. *Passive Hypervelocity Boundary Layer Control Using an Ultrasonically Absorptive Surface*. PhD thesis, California Institute of Technology, 2001.

[40] A. Rasheed, H.G. Hornung, A.V. Fedorov, and N.D. Malmuth. Experiments on passive hypervelocity boundary-layer control using an ultrasonically absorptive surface. *AIAA journal*, 40(3):481–489, 2002.

[41] D.I.A. Poll. Transition in the infinite swept attachment line boundary layer. *The Aeronautical Quarterly*, 30:607–629, 1979.

[42] D.I.A. Poll. The development of intermittent turbulence on a swept attachment line including the effects of compressibility. *The Aeronautical Quarterly*, 34(1):1–23, 1983.

[43] D.I.A. Poll. Transition description and prediction in three dimensional flows. In *Special Course on Stability and Transition of Laminar Flow*, AGARD Report Number 709, 1984.

[44] T. Nomura. Navier-Stokes simulation and linear stability analysis for a boundary layer on the swept cylinder. Technical Report NAL TR-1321, National Aerospace Laboratory, Japan, 1997. (in Japanese).

[45] E. Benard, L. Gaillard, and T. Alziary de Roquefort. Influence of roughness on attachment line boundary layer transition in hypersonic flow. *Experiments in Fluids*, 22(4):286–291, 1997.

[46] T.R. Creel, I.E. Beckwith, and F.J. Chen. Transition on swept leading edges at Mach 3.5. *Journal of Aircraft*, 24(10):710–717, October 1987.

[47] A. Murakami, E. Stanewsky, and P. Krogmann. Boundary-layer transition on swept cylinders at hypersonic speeds. *AIAA Journal*, 34(4):649–654, 1996.

[48] K. Fujii, T. Koyama, S. Tsuda, N Hirabayashi, H. Sekine, S. Nagai, S. Sakakibara, and K. Hozumi. Experiments to ascertain the bluntness effect on attachment line transition of a yawed cylinder in hypersonic flow. Technical Report NAL TM-753, National Aerospace Laboratory, Japan, 2000. (in Japanese).

[49] R.C. Millikan and D.R. White. Systematics of vibrational relaxation. *The Journal of Chemical Physics*, 39(12):3209–3213, 1963.

[50] M. Camac. CO_2 relaxation processes in shock waves. In J.G. Hall, editor, *Fundamental Phenomena in Hypersonic Flow*, pages 195–218. Cornell University Press, 1966.

[51] H.G. Hornung and J. Bélanger. Role and techniques of ground testing for simulation of flows up to orbital speed. AIAA Paper 90-1377, 1990. (16th Aerodynamic Ground Testing Conference, June 18-20, Seattle, WA, USA).

[52] H.G. Hornung, B. Sturtevant, J. Bélanger, S. Sanderson, and M. Brouillette. Performance data of the new free-piston shock tunnel T5 at GALCIT. In *Proceedings of the 18th International Symposium on Shock Waves*, 1991. (Sendai, Japan).

[53] H.G. Hornung. Performance data of the new free-piston shock tunnel T5 at GALCIT. AIAA Paper 92-3943, 1992. (17th Aerospace Ground Testing Conference, July 6-8, Nashville, TN, USA).

[54] N. Sudani and H.G. Hornung. Gasdynamical detectors of driver gas contamination in a high-enthalpy shock tunnel. *AIAA Journal*, 36(3):313–319, 1998.

[55] W.C. Reynolds. The element potential method of chemical equilibrium analysis: Implementation in the interactive program STANJAN. Technical report, Department of Mechanical Engineering, Stanford University, 1986.

[56] M.W. Chase. NIST-JANAF thermochemical tables. *Journal of Physical and Chemical Reference Data, Monograph*, (9), 1998.

[57] J.A. Lordi, R.E. Mates, and J.R. Moselle. Computer program for the numerical solution of nonequilibrium expansions of reacting gas mixtures. Technical Report NASA CR-472, National Aeronautics and Space Administration (NASA), 1966.

[58] H. Schlichting. *Boundary Layer Theory.* McGraw-Hill Company, 1987.

[59] C.R. Wilke. A viscosity equation for gas mixtures. *Journal of Chemical Physics*, 18(4):517–519, April 1950.

[60] J.O. Hirschfelder, C.F. Curtiss, and R.B. Bird. *Molecular Theory of Gases and Liquids.* John Wiley and Sons, 1954.

[61] F.G. Blottner, M. Johnson, and M.G. Ellis. Chemically reacting viscous flow program for multi-component gas mixtures. Technical Report SC-RR-70-754, Sandia Laboratories, Albuquerque, N.M., December 1971.

[62] W Sutherland. The viscosity of gases and molecular force. *Phil. Mag.*, 5, 1893.

[63] B.E. Poling, J.M. Prausnitz, and J.P. O'Connell. *The Properties of Gases and Liquids.* McGraw-Hill, fifth edition, 2001.

[64] L. Monchick and E.A. Mason. Transport properties of polar gases. *Jounal of Chemical Physics*, 35:1676, 1961.

[65] P.D. Neufeld, A.R. Janzen, and R.A. Aziz. Empirical equations to calculate 16 of the transport collision integrals $\Omega^{(l,s)*}$ for the Lennard-Jones (12-6) potential. *Journal of Chemical Physics*, 57(3):1100–1102, 1972.

[66] S.R. Sanderson. *Shock Wave Interaction in Hypervelocity Flow.* PhD thesis, California Institute of Technology, 1995.

[67] J.P. Davis. *High-Enthalpy Shock/Boundary-Layer Interaction on a Double Wedge.* PhD thesis, California Institute of Technology, 1999.

[68] ASTM. *Manual on the Use of Thermocouples in Temperature Measurement*, fourth edition, 1993.

[69] D.L. Schultz and T.V. Jones. Heat transfer measurements in short duration hypersonic facilities. Technical Report AG-165, AGARD, 1973.

[70] D. Kendall, W.P. Dixon, and E.H. Schulte. Semiconductor surface thermocouples for determining heat-transfer rates. *IEEE Transactions on Aerospace and Electronic Systems*, 3(4):596–602, July 1967.

[71] I.E. Beckwith and J.J. Gallagher. Local heat transfer and recovery temperatires on a yawed cylinder at a Mach number of 4.15 and high Reynolds numbers. Technical Report NASA TR R-104, National Aeronautics and Space Administration (NASA), 1961.

[72] W.H. Dorrance. *Viscous Hypersonic Flow.* McGraw-Hill Book Company, 1962.

[73] E.P. Bartlett and R.M. Kendall. An analysis of the coupled chemically reacting boundary layer and charring ablator. part3 - nonsimilar solution of the multicomponent laminar boundary layer by an integral matrix method. Technical Report NASA CR-1062, National Aeronautics and Space Administration (NASA), 1968.

[74] H. Tong, A.C. Buckingham, and H.L. Morse. Nonequilibrium chemistry boundary layer integral matrix procedure. Technical Report NASA CR-134039, National Aeronautics and Space Administration (NASA), 1973.

[75] A.L. Murray. Further enhancements of the blimp computer code and user's guide. Technical Report Aerotherm Final Report 88-12/ATD, Acurex Corporation, 1988. (also, AFWAL TR-88-3010).

[76] P.H. Adam. BLIMPK simulations of hypervelocity boundary layers. Technical Report FM 96-6, GALCIT, California Institute of Technology, 1996.

[77] Y.-K. Chen, W.D. Henline, D.A. Stewart, and G.V. Candler. Navier-Stokes solutions with surface catalysis for Martian atmospheric entry. *Journal of Spacecraft and Rockets*, 30(1):32–42, 1993.

[78] J.C. Cooke. An axially symmetric analogue for general three-dimensional boundary layers. Technical Report R&M 3200, British Aeronautical Research Council, 1961.

[79] F.R. DeJarnette and R.M. Davis. A simplified method for calculating laminar heat transfer over bodies at an angle of attack. Technical Report NASA TN D-4720, National Aeronautics and Space Administration (NASA), 1968.

[80] J.V. Rakich and G.G. Mateer. Calculation of metric coefficients for streamline coordinates. *AIAA journal*, 10(11):1538–1540, 1972.

[81] M.L. Hudson, N. Chokani, and G. Candler. Linear stability of hypersonic flow in thermochemical nonequilibrium. *AIAA Journal*, 35(6):958–964, 1997.

[82] F.P. Bertolotti. The influence of rotational and vibrational energy relaxation on boundary-layer stability. *Journal of Fluid Mechanics*, 372:93–118, 1998.

[83] E. Reshotko and I.E. Beckwith. Compressible laminar boundary layer over a yawed infinite cylinder with heat transfer and arbitrary Prandtl number. Technical Report NACA Report 1379, National Advisory Committee for Aeronautics (NACA), 1958.

[84] K.F. Stetson and R.L. Kimmel. On hypersonic boundary-layer stability. AIAA Paper 92-0737, 1992. (30th Aerospace Sciences Meeting and Exhibit, January 6-9, Reno, NV, USA).

[85] I.E. Beckwith. Development of a high reynolds number quiet tunnel for transition research. *AIAA Journal*, 13(3):300–306, 1975.

[86] E.R. Van Driest. Calculations of the stability of the laminar boundary layer in a compressible fluid on a flat plate with heat transfer. *Journal of the Aeronautical Sciences*, 19(13):801–812, 1952.

[87] D.C. Reda. Roughness-dominated transition on nosetips, attachment lines and lifting-entry vehicles. AIAA Paper 2001-0205, 2001. (39th AIAA Aerospace Sciences Meeting and Exhibit, January 8-11, Reno, NV, USA).

[88] D.I.A. Poll. The effect of isolated roughness elements on transition in attachment-line flows. In *Laminar-Turbulent Transition*, IUTAM Symposium, 1989. (Toulouse, France).

[89] G.A. Flynn and R.I. Jones. Attachment line transition with 3D isolated roughness elements. (AIAA Paper 99-1018), 1999. (37th AIAA Aerospace Sciences Meeting and Exhibit).

[90] A.L. Braslow, R.M. Hicks, and R.V. Harris Jr. Use of grit-type boundary-layer-transition trips on wind-tunnel models. Technical Report NASA TN D-3579, National Aeronautics and Space Administration (NASA), 1966.

[91] R.L. Kimmel, J. Poggie, and J.D. Schmisseur. Effect of pressure gradients on axisymmetric hypersonic boundary layer stability. (AIAA Paper 2000-0538), 2000. (38th AIAA Aerospace Sciences Meeting and Exhibit, January 10-13, Reno, NV, USA).

[92] S.P. Schneider. Effect of high-speed tunnel noise on laminar-turbulent transition. *Journal of Spacecraft and Rockets*, 38(3):323–333, 2001.

[93] K. Fujii, S. Watanabe, M. Shirouzu, Y. Inoue, T. Kurotaki, T. Koyama, S. Tsuda, and N. Hirabayashi. Aerodynamic heating measurements on Hypersonic Flight Experiment (HYFLEX) vehicle. Technical Report NAL TR-1415, National Aerospace Laboratory, Japan, 2000. (in Japanese).

[94] J.D. Anderson. *Hypersonic and High Temperature Gas Dynamics.* McGraw-Hill Book Company, 1989.

[95] C Park. *Nonequilibrium Hypersonic Aerothermodynamics.* John Willey and Sons, 1990.

[96] C. Park, R.L. Jaffe, and Harry Partridge. Chemical-kinetic parameters of hyperbolic earth entry. AIAA Paper 00-0210, 2000. (38th AIAA Aerospace Sciences Meeting and Exhibit, January 10-13, Reno, NV, USA).

Table 3.1: Summary of Flow Conditions. Mole fraction is at the edge of attachment line boundary layer assumed equilibrium.

Gas	ϕ_{Throat}	h_0	P_0	U_e	M_e	T_e	ρ_e	mole fractions	
	mm	MJ/kg	MPa	m/s		K	kg/m^3	at the edge	
				N_2 shots, $\Lambda = 60$ deg				x_{N_2}	
N_2	30	2.0∼15.0	10.0∼71.9	1660∼4300	3.3∼3.4	620∼4480	0.07∼0.37	0.99∼1.00	
N_2	30	18.7∼20.7	53.7∼57.5	4690∼4880	3.2	5350∼5660	0.15	0.91∼0.95	
				Air shots, $\Lambda = 60$ deg				x_{N_2}	x_{O_2}
Air	30	1.7∼15.9	11.9∼68.5	1650∼4300	3.2∼3.3	640∼3930	0.12∼0.28	0.67∼0.78	0.06∼0.21
				CO_2 shots, $\Lambda = 60$ deg				x_{CO_2}	
CO_2	15	1.5∼4.3	4.4∼48.6	1410∼2080	3.2∼3.7	760∼1940	0.02∼0.31	0.97∼1.00	
CO_2	30	1.4∼4.4	4.7∼47.8	1400∼2130	3.2∼3.4	750∼1960	0.09∼0.68	0.98∼1.00	
CO_2	30	5.8∼15.4	23.0∼72.2	2360∼3540	3.3	2320∼3440	0.20∼0.43	0.22∼0.92	
				N_2 shots, $\Lambda = 45$ deg				x_{N_2}	
N_2	30	3.3∼16.5	6.3∼66.5	1800∼3660	2.2∼2.3	1760∼6090	0.13∼0.31	0.88∼1.00	
				Air shots, $\Lambda = 45$ deg				x_{N_2}	x_{O_2}
Air	30	2.8∼16.5	6.3∼66.5	1640∼3550	2.1∼2.3	1590∼5310	0.03∼0.36	0.62∼0.78	0.01∼0.21
				CO_2 shots, $\Lambda = 45$ deg				x_{CO_2}	
CO_2	30	2.2∼16.2	3.8∼60.9	1340∼2910	2.4	1440∼3840	0.12∼0.64	0.11∼1.00	

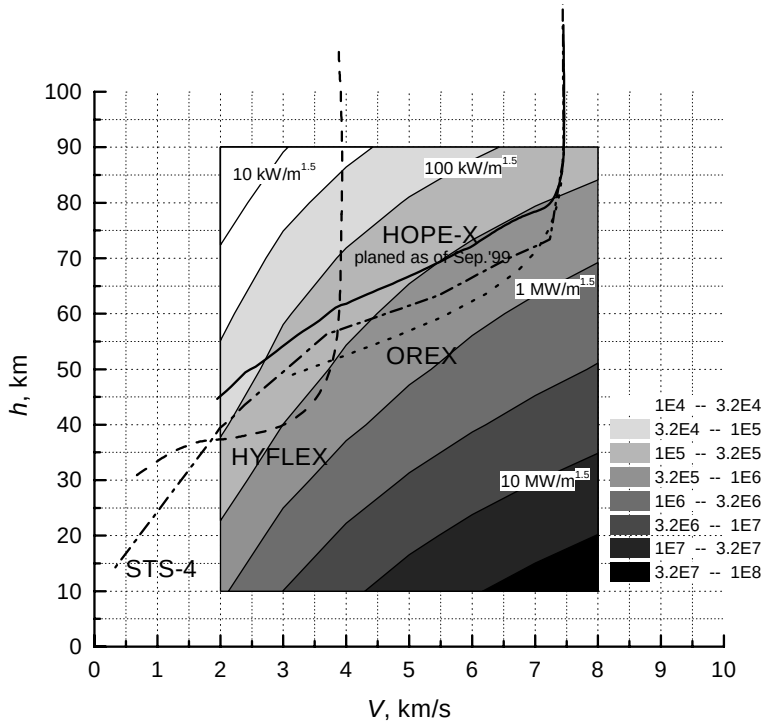

(a) Stagnation heat transfer to sphere of 1m radius calculated by means of the formula by Fay and Riddell[1]

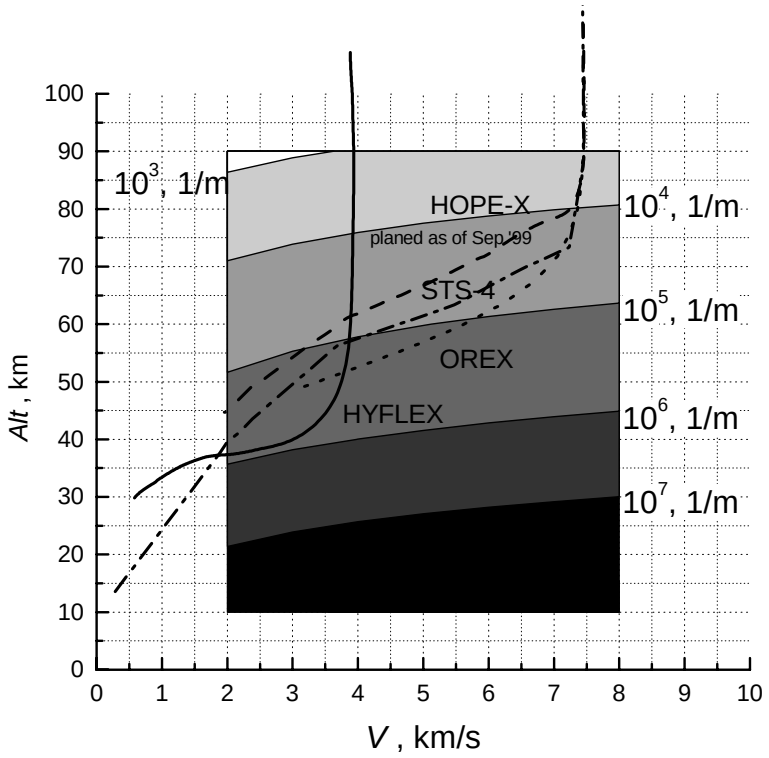

(b) Freestream unit Reynolds number, 1/m

Figure 1.1: Schematic diagram showing estimated stagnation heat flux and unit Reynolds number along a typical re-entry vehicle to the earth's atmosphere. (a) illustrates that typical re-entry vehicles or their trafectories are designed to keep aerodynamic heating below the maximum allowable limit. (b) shows re-entry vehicles eventually experience boundary layer transion during their descent which cause heat flux to increase.

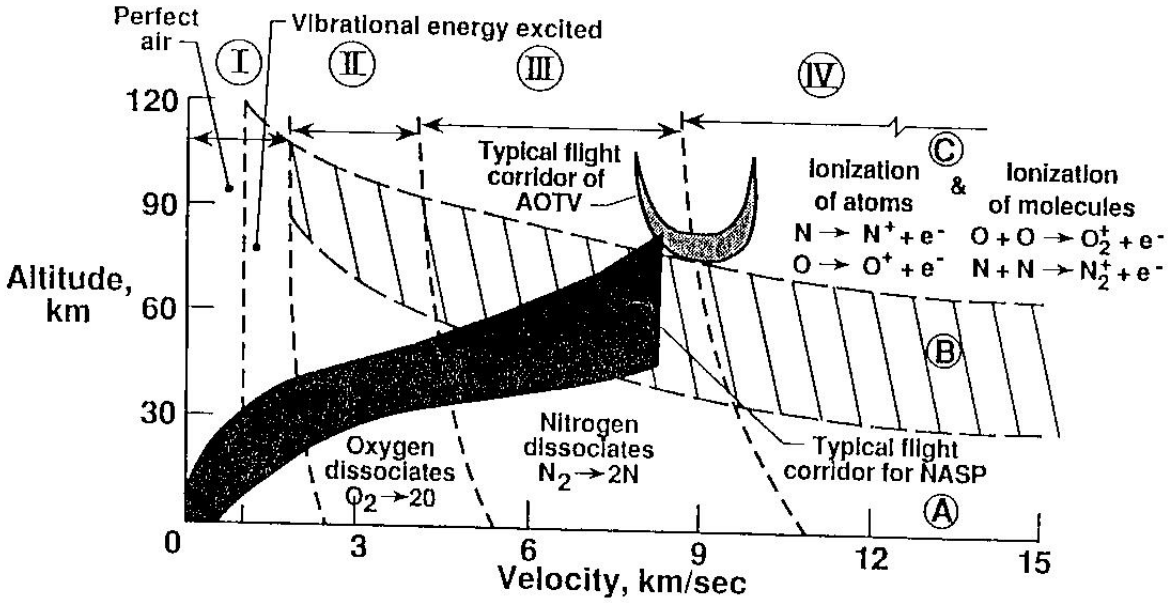

Figure 1.2: Schematic diagram showing thermal and chemical conditions in the stagnation region of a vehicle travelling through the earth's atmosphere. It is obvious that an actual vehicle travelling at a hypersonic speed experiences high temperature flow where chemical and vibrational effects cannot be neglected. Taken from Hansen[9]

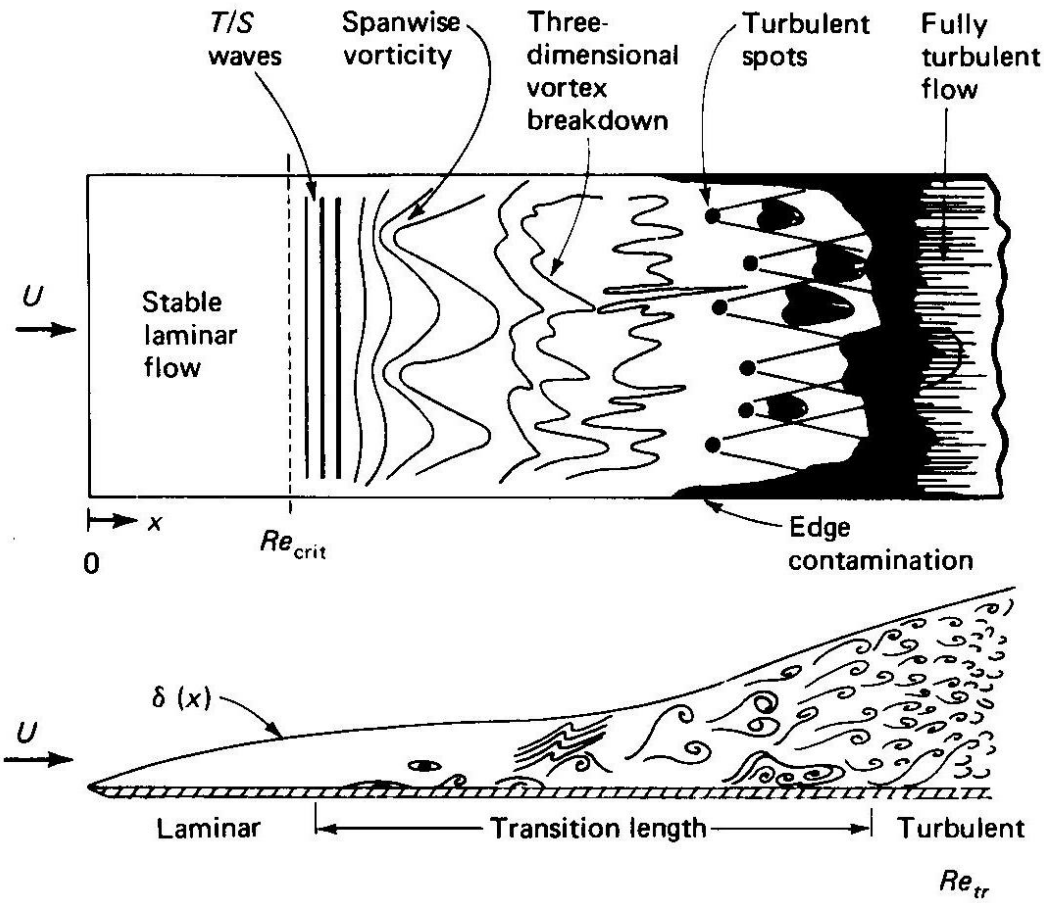

Figure 2.1: Schematic diagram showing a typical transition process of incompressible flat plate boundary layer. Initial disturbances are amplified by linear instability mechanism, followed by three-dimensional processes, and finally turbulent spots agglomerate to be regarded as turbulent. (Taken from White[17])

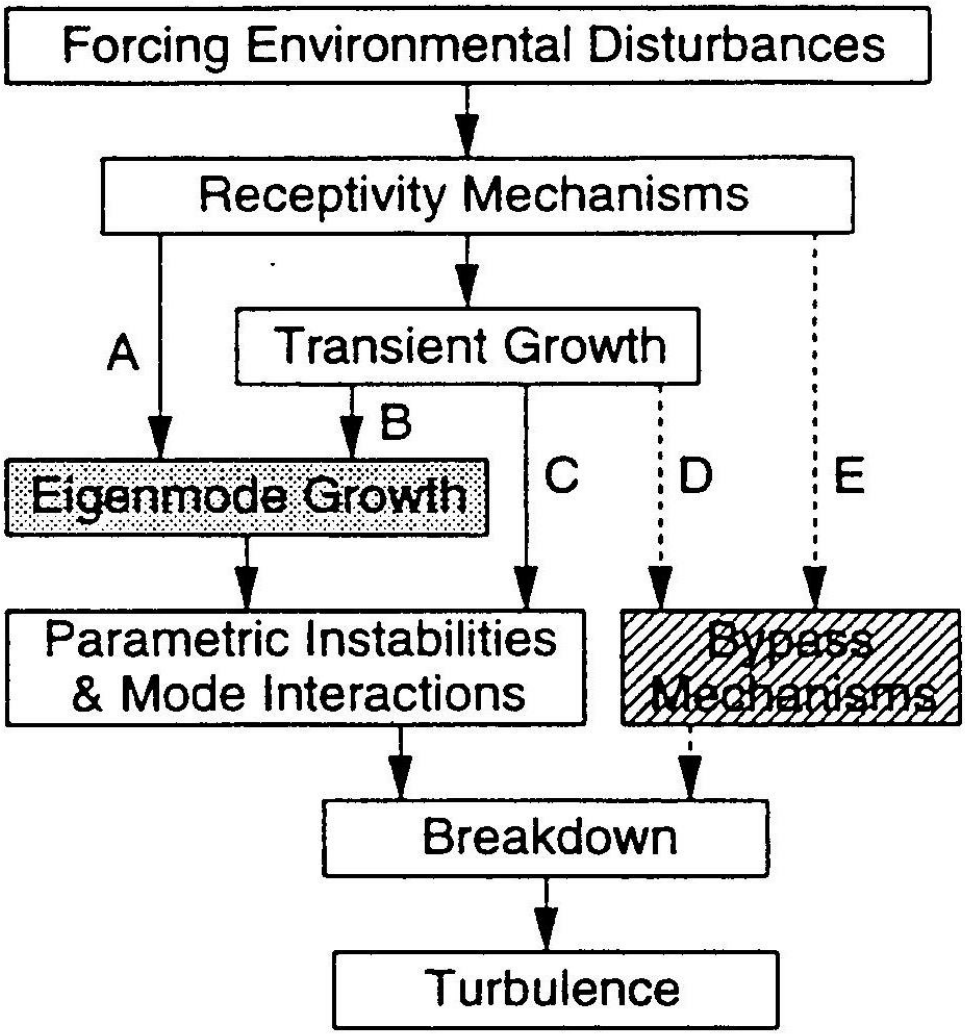

Figure 2.2: Schematic diagram of paths to transition. After entrainment of environmental disturbances, several paths to transition are possible. (After Herbert[18])

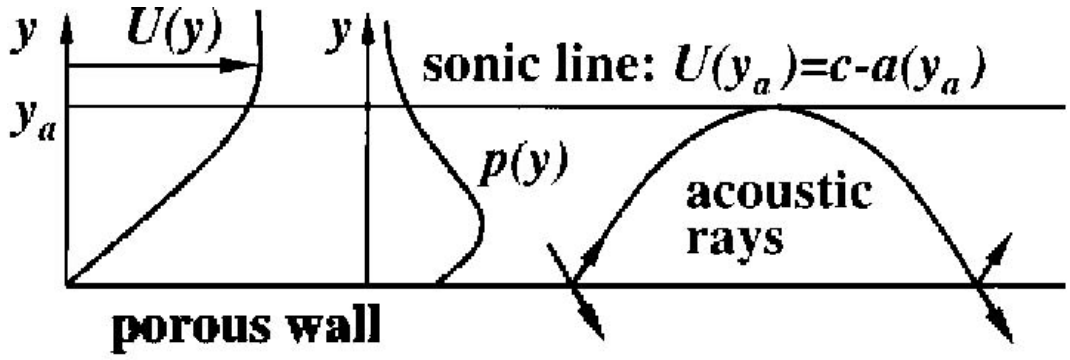

Figure 2.3: Schematic diagram showing the Mack mode (2nd mode) in a hypersonic boundary layer. $U(y)$ is the mean flow velocity profile, $p(y)$, the disturbance pressure profile, c the phase velocity of the disturbance waves, a the local speed of sound, y_a the location of the sonic line which is defined as the location where relative velocity to external flow is equal to sound speed. Taken from Fedorov and Malmuth[38]

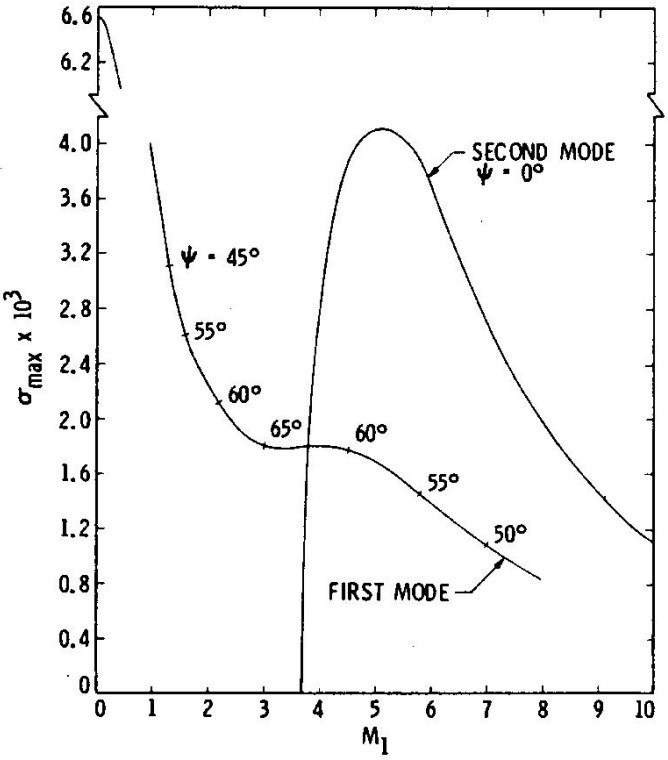

Figure 2.4: Effect of edge Mach number on the maximum spatial amplification rate of first and second mode waves in a flat plate boundary layer at R =1500. Insulated wall. Stagnation temperature is held constant at 311 K until the Mach number at which edge temperature T_1 equals 50 K, and T_1 is held at 50 K at larger edge Mach number. Reproduced from Mack[22]

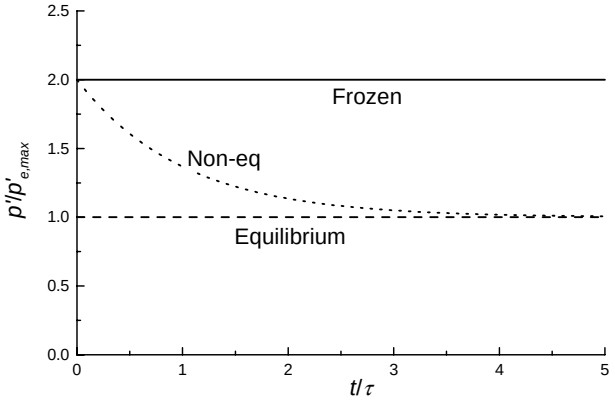

(a) Typical relaxation process in pressure responce to abrupt increase in density at $t/\tau = 0$

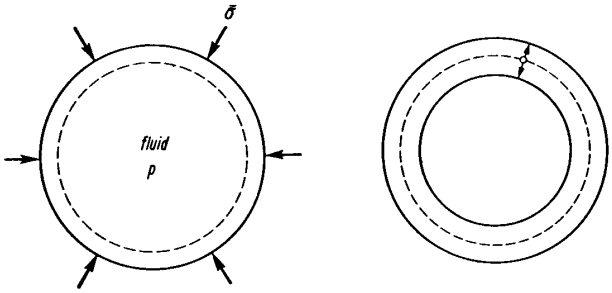

(b) Oscillating fluid particle producing bulk viscosity (reproduction from Schlichting[58])

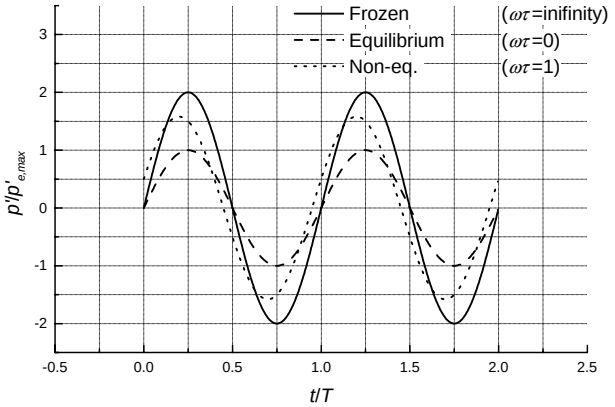

(c) Responce in pressure to oscillating particle of gas in volume.

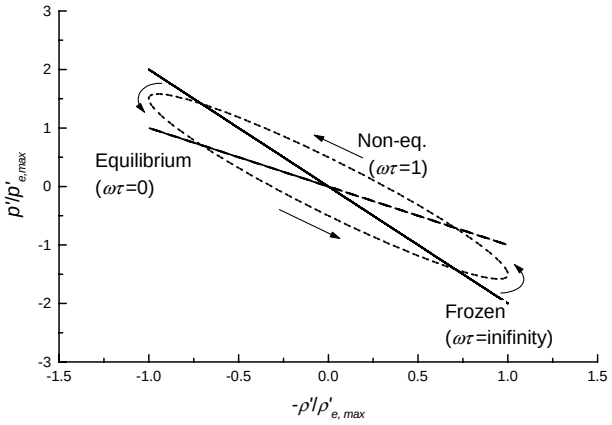

(d) Responce diagram in $p - \rho$ plane

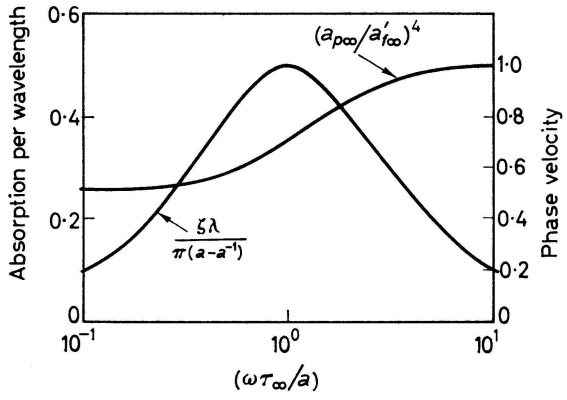

(e) Sound propagation through relaxing gases (reproduction from Clarke and McChesney[16])

Figure 2.5: Schematic diagrams showing effects of relaxing processes. (a),(c),(d):Phase-advanced responce in pressure exists in neither frozen nor equilibrium limit, but in non-equilibrium. p_f/p_e is assumed equal to 2 for simplicity. (e):Sound absorption rate is not expected in the both limit, and takes its maximum at a frequency of reciprocal of characteristic relaxaton time. It is assumed as the ratio of speed of sounds a_f/a_e of 1.183

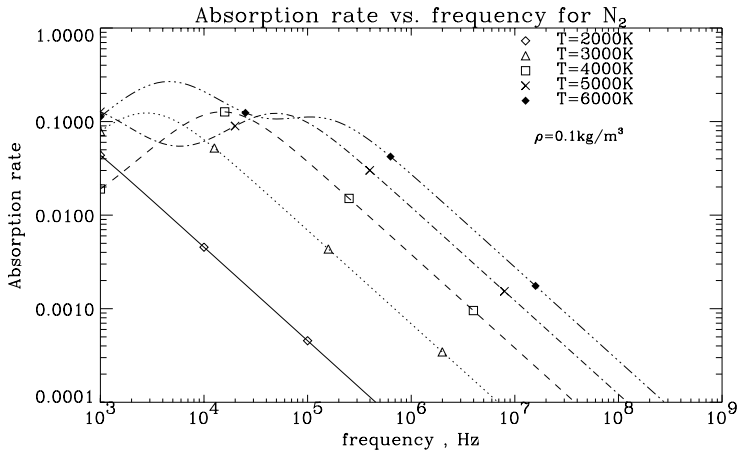

(a)N_2

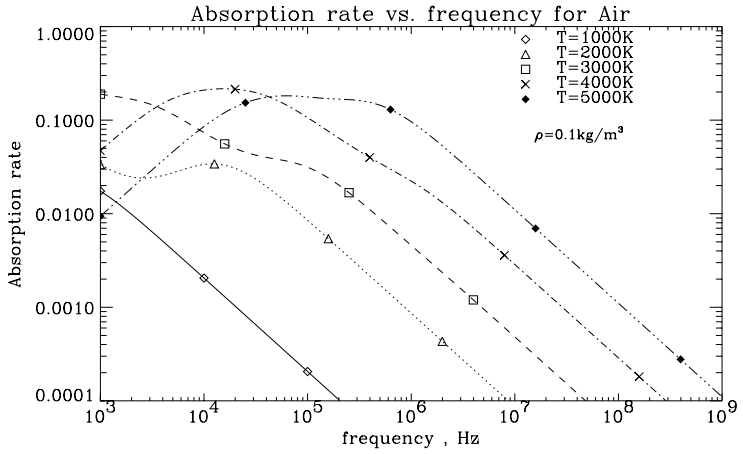

(b)Air

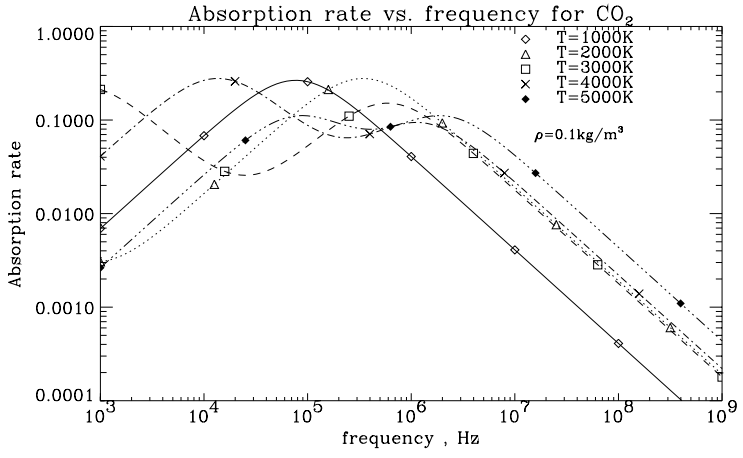

(c)CO_2

Figure 2.6: Calculation of sound absorption rate due to multiple relaxing process including vibrational excitations and chemical reactions of several gas species. Density is kept constant at 0.1 kg/m^3 to represent approximately the conditions of the present experiment. (After Fujii and Hornung[33])

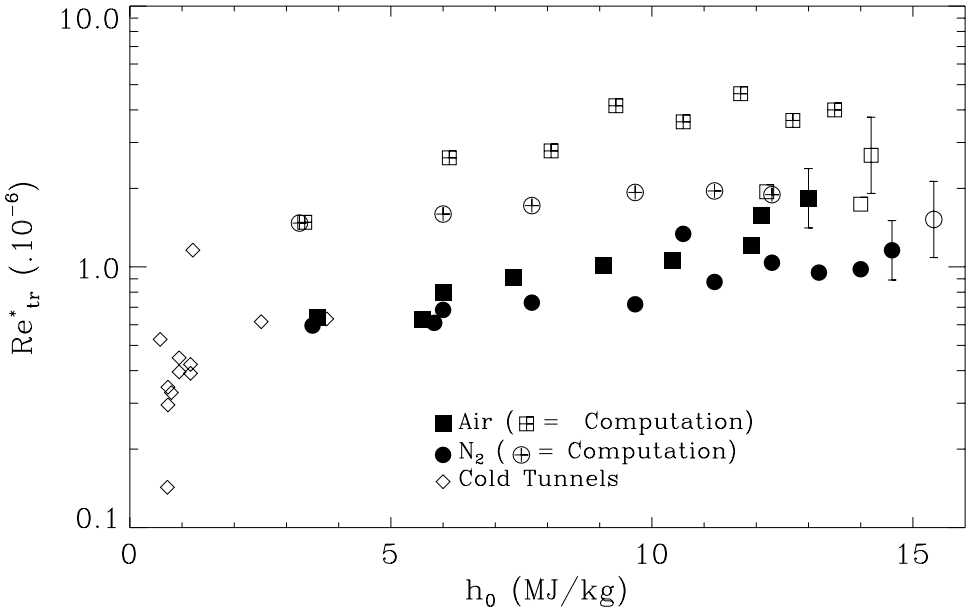

Figure 2.7: Transition Reynolds number measured in high total enthalpy conditions with 5 deg half-angle sharp cone in T5. Test gases employed are air or pure nitrogen. Open symbols with '+' indicate numerical prediction from non-equilibrium linear instability analysis by Johnson *et al.*[15], where the e^N method is applied. Reproduced from Adam[35].

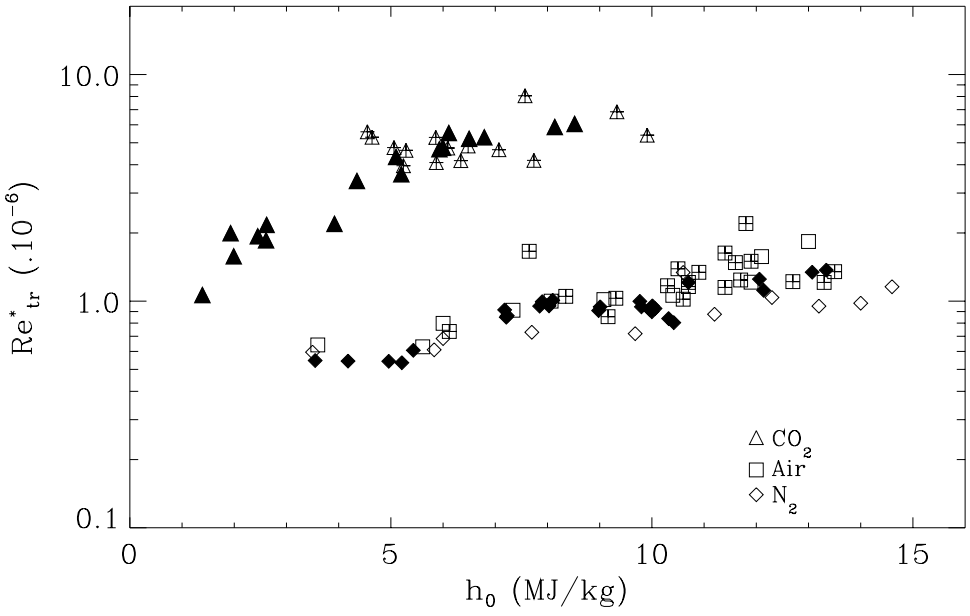

Figure 2.8: Transition Reynolds number observed in previous cone experiments. Open symbols are taken from Germain[34], symbols with '+' from Adam[35], and solid symbols from Rasheed[39].

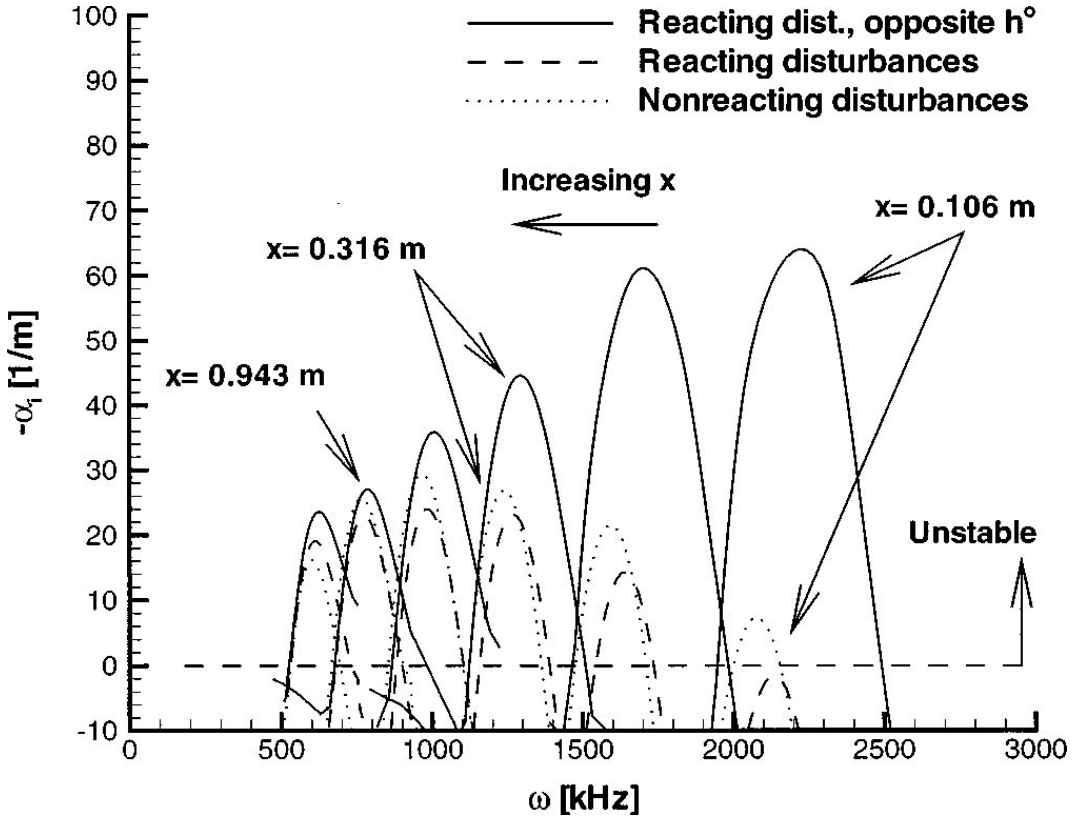

Figure 2.9: Amplification rate α_i from non-equilibrium linear stability analysis evaluated at several locations in sharp cone boundary layer with the condition of shot 1162 of Adam's experiment[35] (Air, h_0 =9.3 MJ/kg, P_0 =34.4 MPa, T_∞ =1330 K, $T_{v,\infty}$ =3000 K, V_∞ =3750.8 m/s, ρ_∞ =0.0396 kg/m^3). Virtual amplification rates calculated with opposite sign of heat of formation of O_2 molecule (solid lines) are compared with amplification rates assuming actual reaction effects and without reaction. Taken from Johnson *et al.*[15].

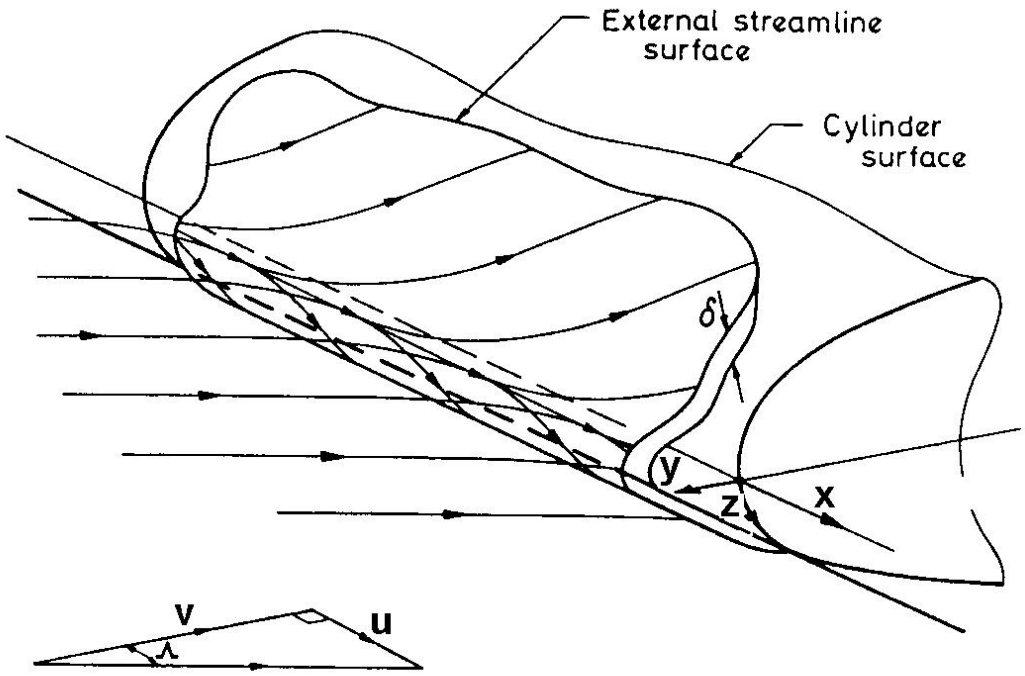

Figure 2.10: Schematic diagram showing flow field in the vicinity of attachment line of yawed cylinder. (After Poll[41])

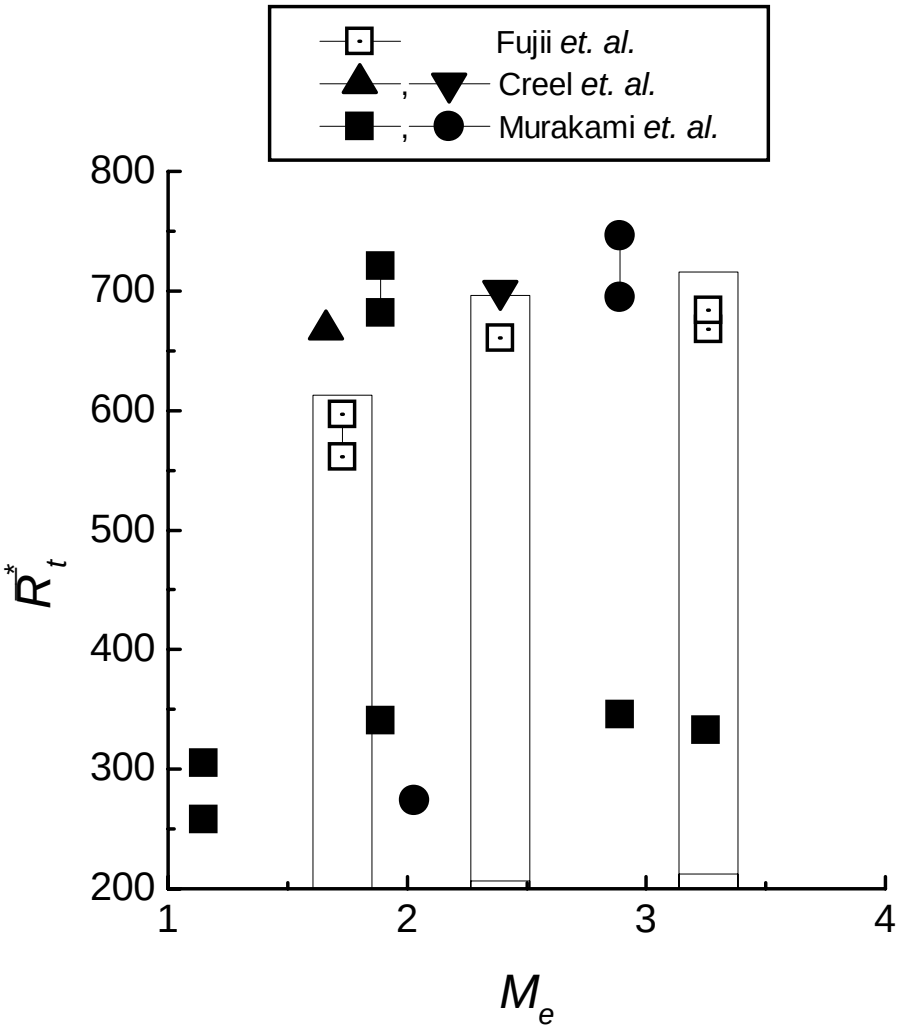

Figure 2.11: Transition attachment-line Reynolds number obtained by Creel *et al.*[46], Murakami *et al.*[47] and Fujii *et al.*[48]. Transition Reynolds number with no large disturbances upstream ranges from 600 to 750. Slight increasing trend with edge Mach number is apparent.

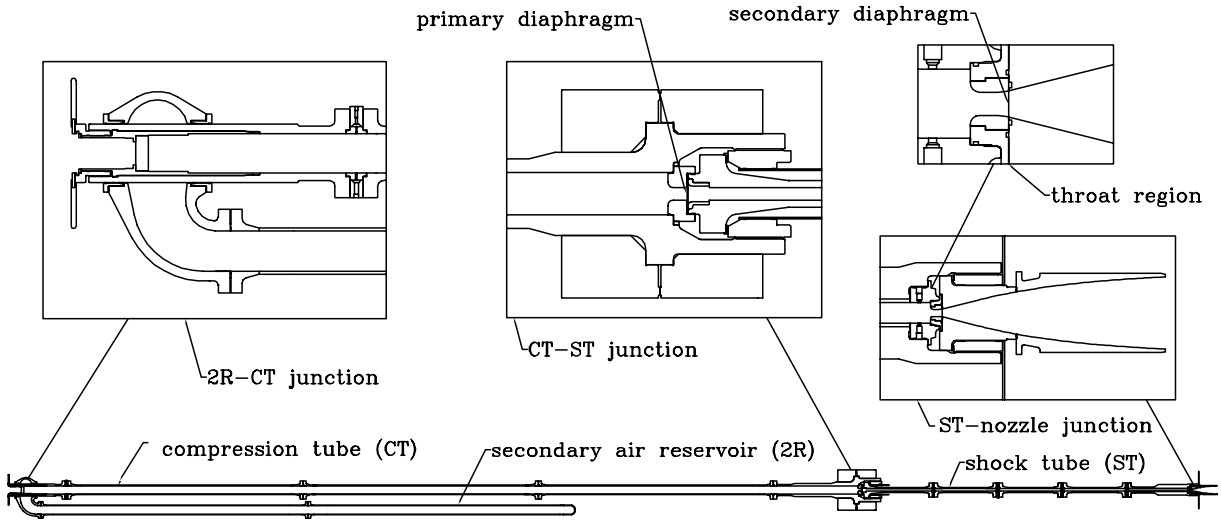

Figure 4.1: Schematic diagram of the T5 Hypervelocity Shock Tunnel. The six major components are the piston, the secondary reservoir, the compression tube, the shock tube, the test section and the dump tank. Overall facility with attached test section and dump tank to the right end in the figure is approximately 50 m long.

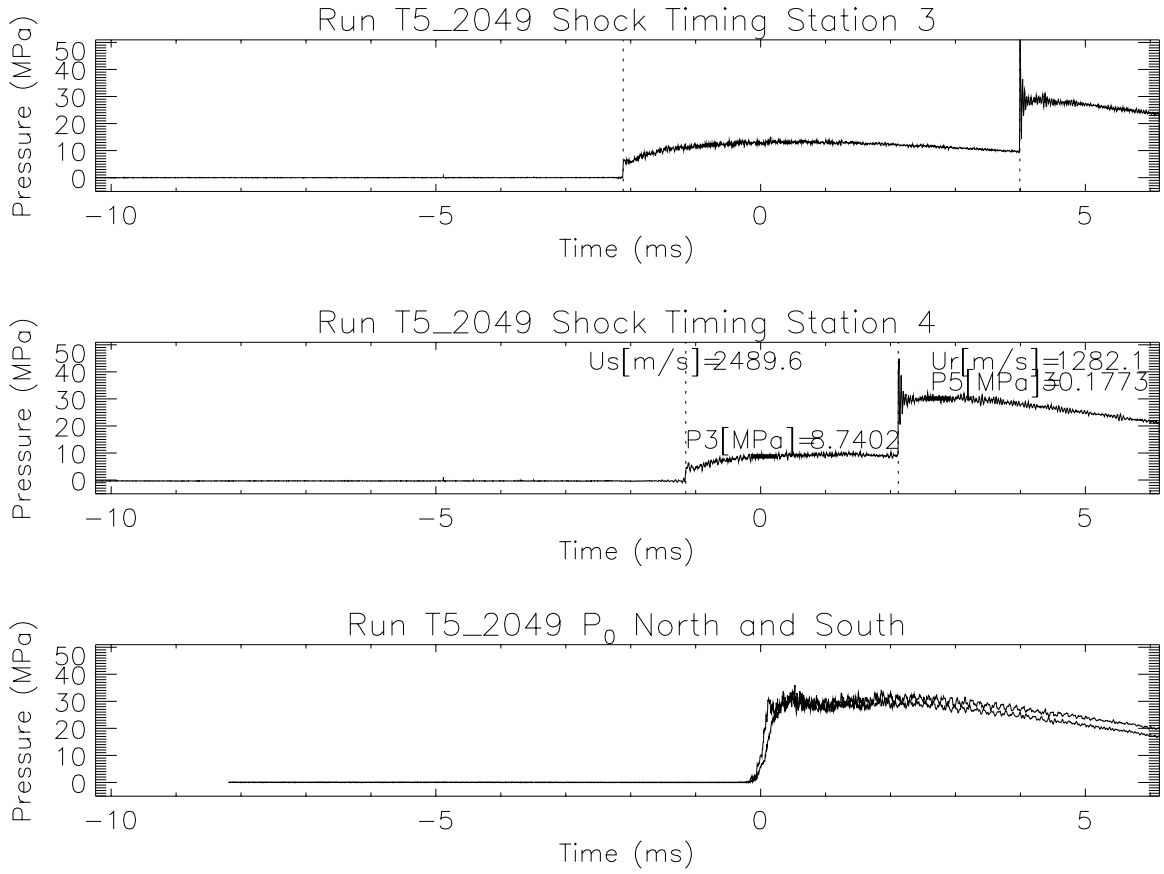

Figure 4.2: Typical traces of diagnostic data measurements. Pressure trace at the shock tube timing station #3 (top), #4 (middle) and stagnation pressure traces (North and South sides, bottom figure). The incident shock speed is read from the time difference in pressure rises between station #3 and #4.

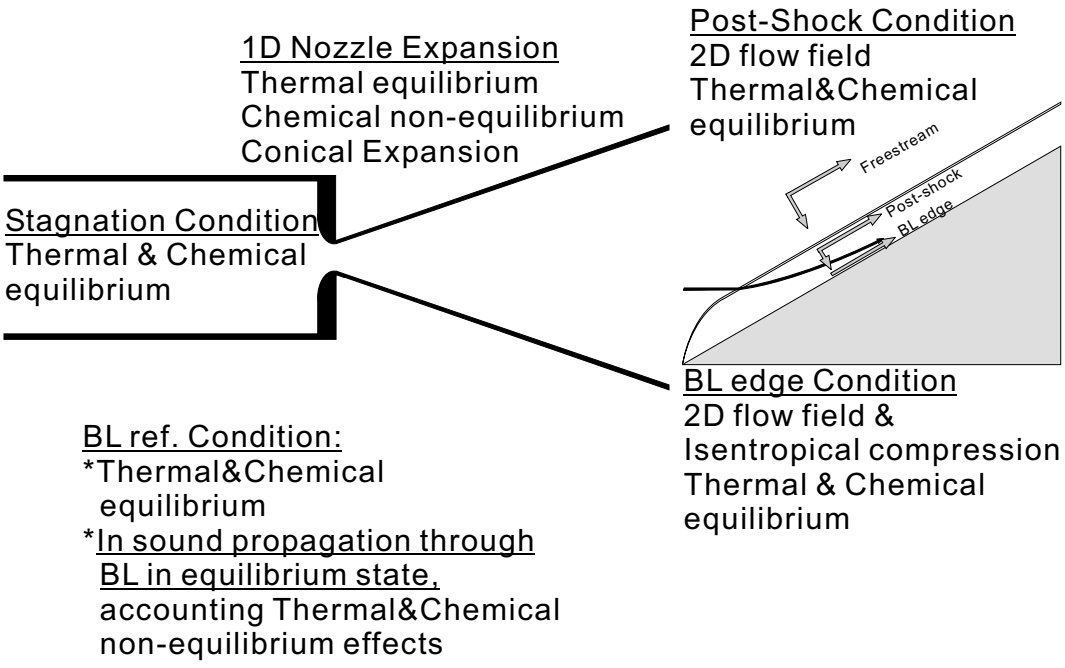

Figure 4.3: Schematic diagram on assumptions made for the flow field modeling

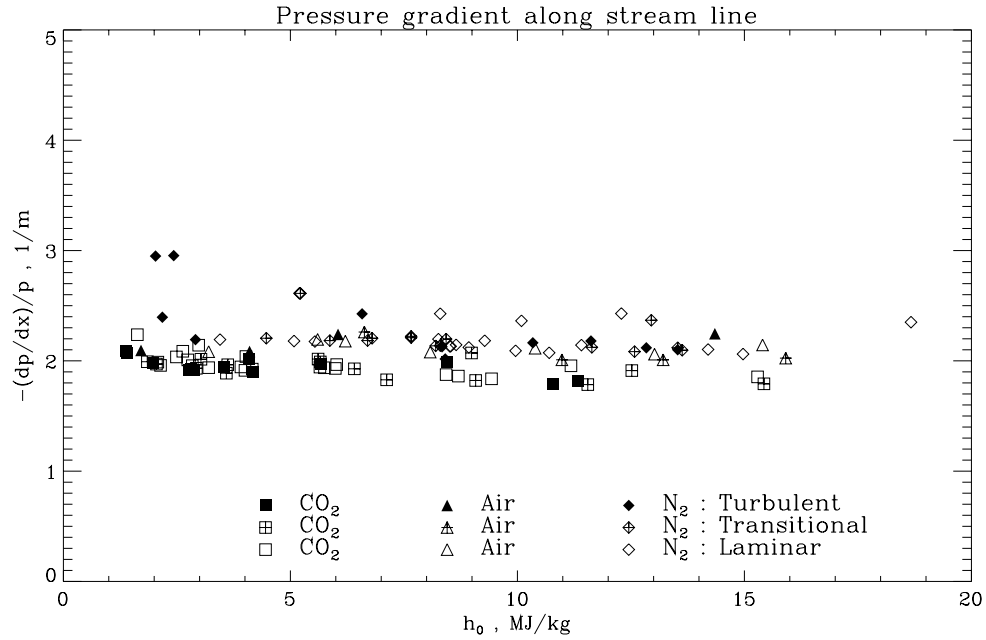

Figure 4.4: The longitudinal pressure gradient in the freestream calculated with NENZF nozzle flow code for the flow conditions of the present experiment. No evident dependence on the total enthalpy or on the test gas species can be seen.

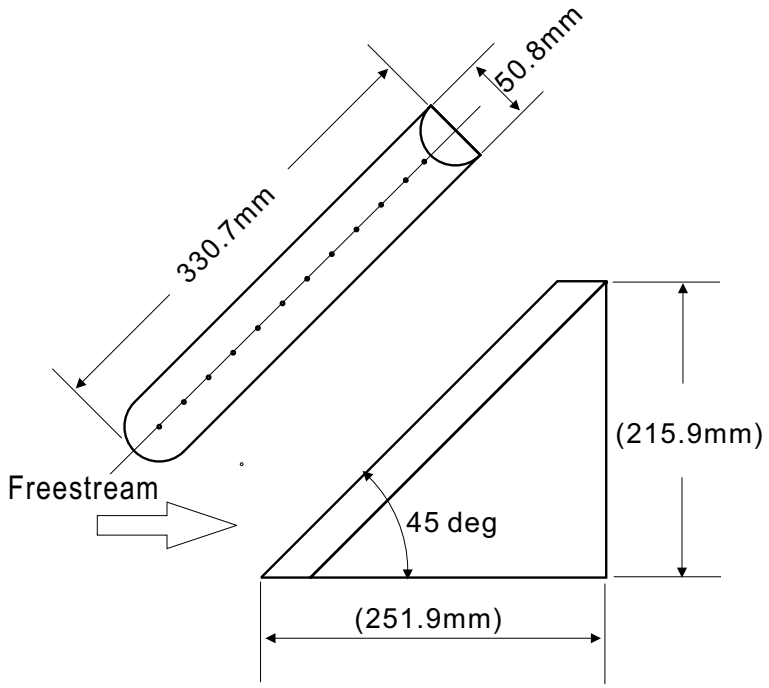

(a)$\Lambda = 45$ deg model

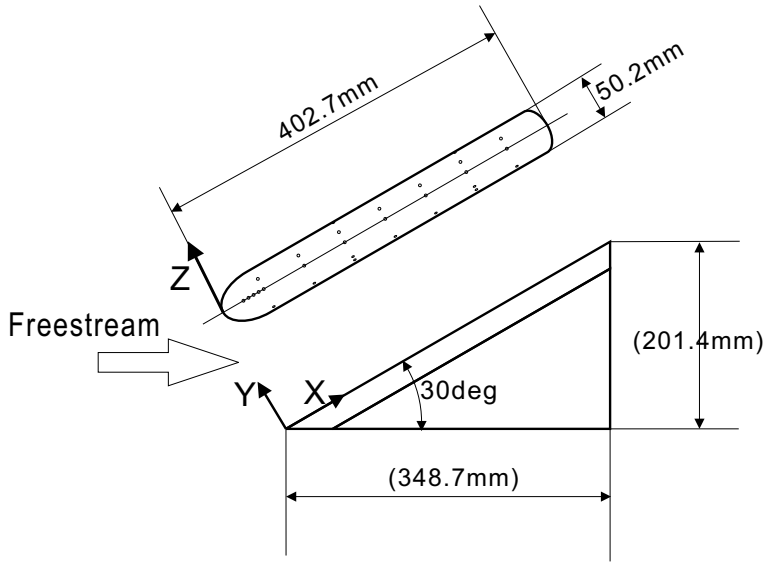

(b)$\Lambda = 60$ deg model

Figure 4.5: Sketch of the swept cylinder models for the present experiment. Aerodynamic heating to the attachment line of the models is measured with in-house made coaxial thermocouples assuming semi-infinite one dimensional heat conduction.

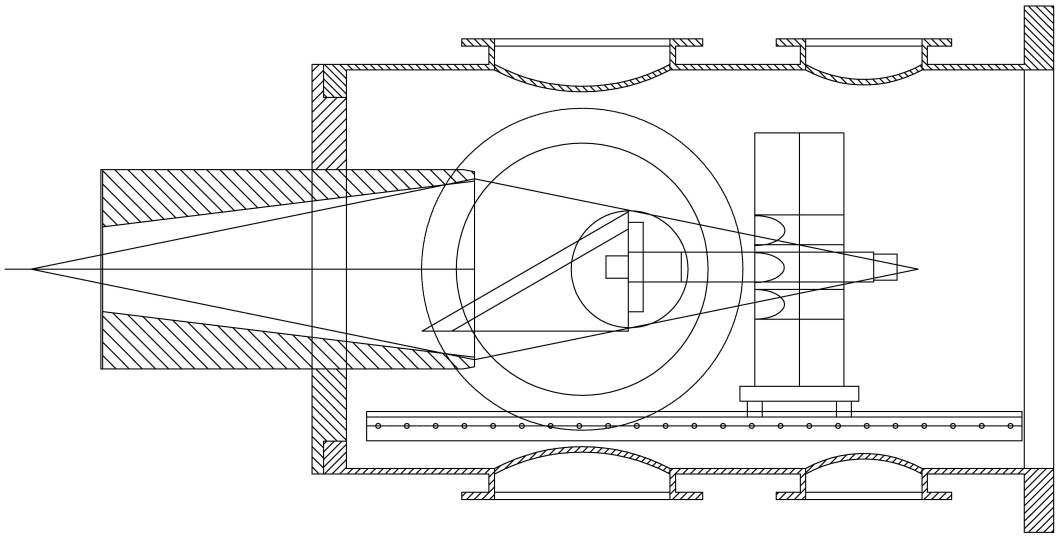

Figure 4.6: Schematic diagram showing the model setup in the test section. Oblique lines from the nozzle tip represent expansion wave angle.

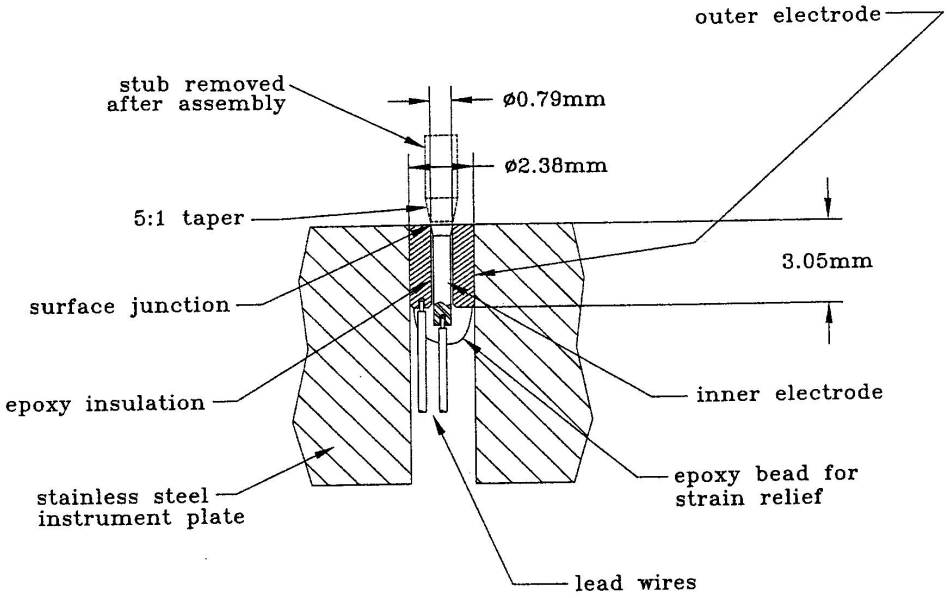

Figure 4.7: Schematic diagram of a coaxial surface thermocouple shown mounted in a model. Outer electrode is made from constantan, and inner electrode is from chromel, forming a type-E thermocouple on the surface.

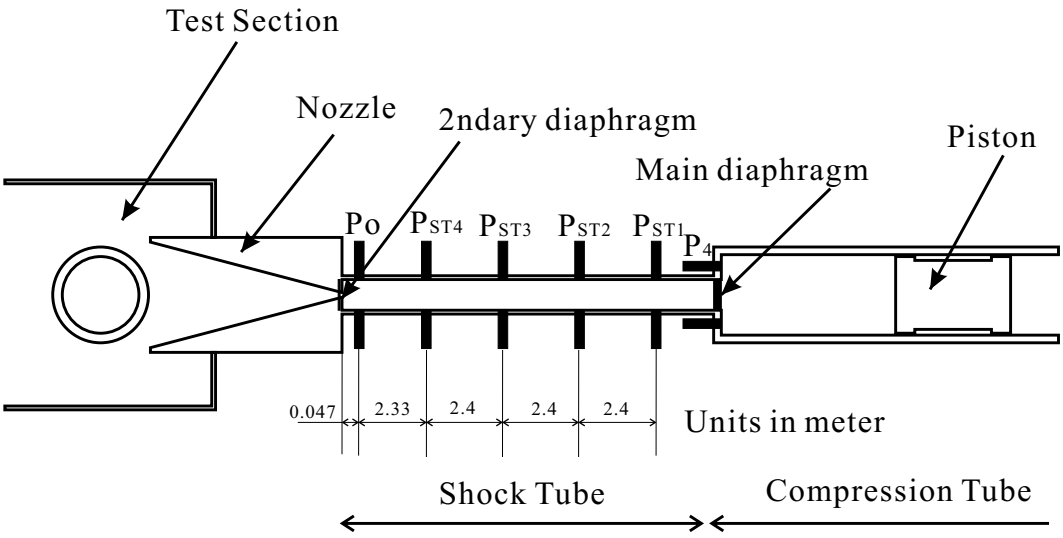

Figure 4.8: Schematic diagram showing facility diagnostic data acquisition (pressure measurement).

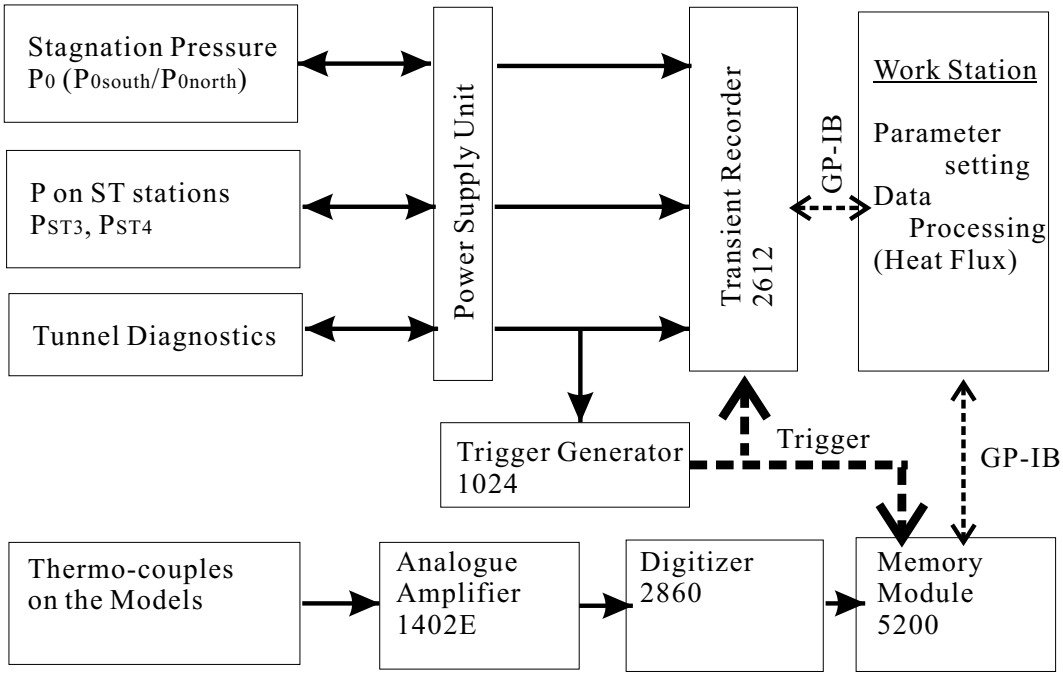

Figure 4.9: Schematic diagram of data acquisition in the experiment.

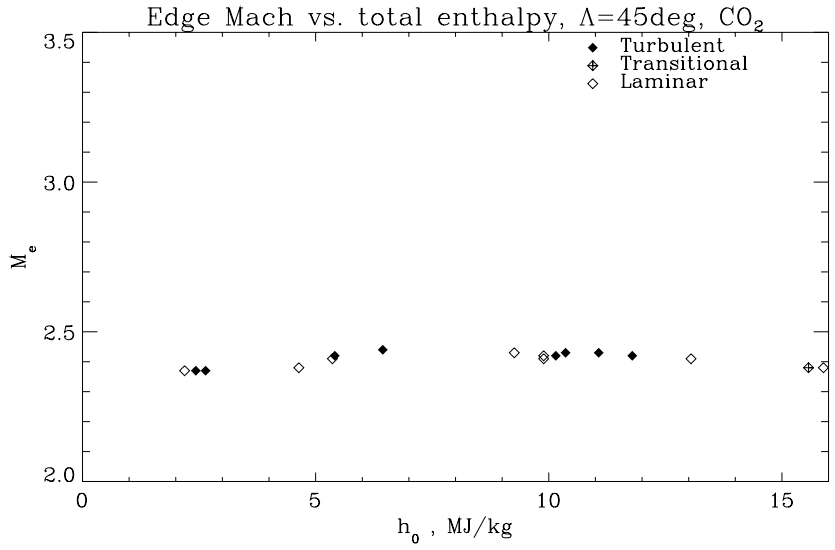

(a)Λ=45 deg, CO_2

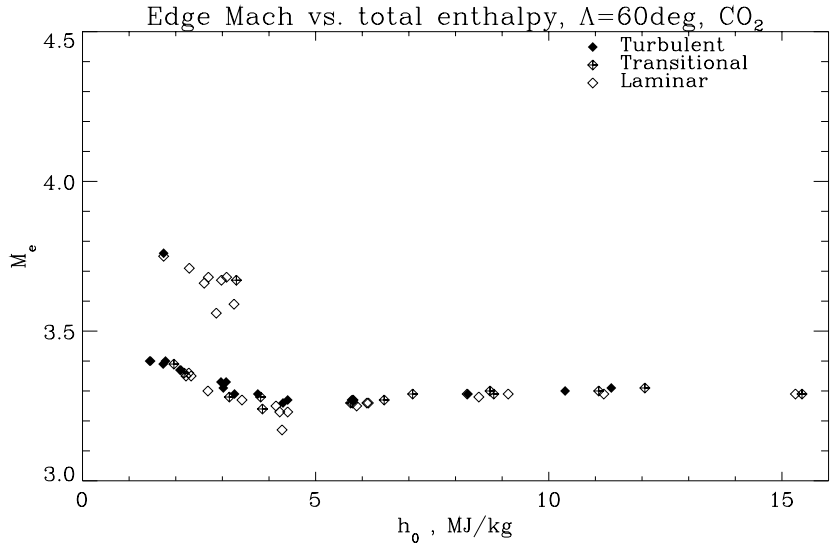

(b)Λ=60 deg, CO_2

Figure 4.10: Frozen edge Mach number versus total enthalpy for carbon dioxide tests. It is assumed that the edge condition is both chemically and vibrationally in equilibrium.

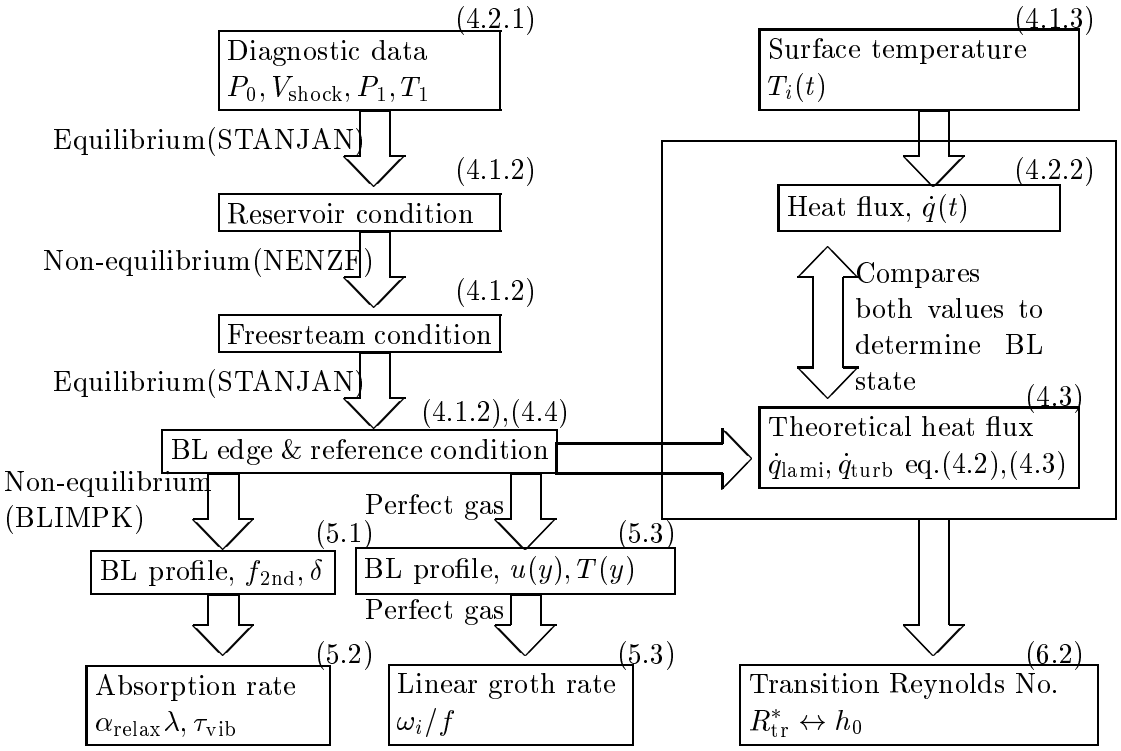

Figure 5.1: Schematic diagram showing flow of data analysis in the present study. Variables at the top are measurable quantities, and those at the bottom represent reduced quantities which appear in the discussion. Numbers on the upper right corner of each box denote the section where the item is first described.

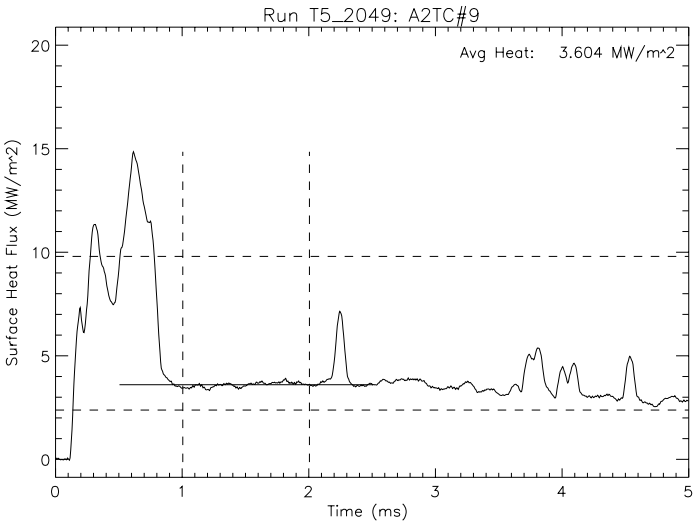

(a)Heat flux trace

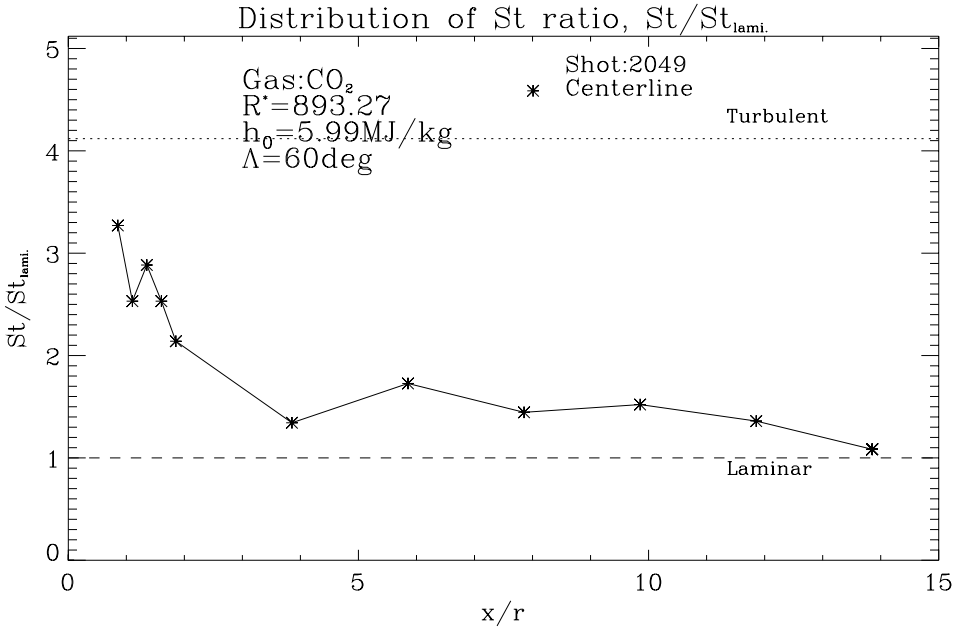

(b)Heat flux distribution at #9 sensor ($x/r \approx 10$)

Figure 6.1: A typical heat flux to the attachment line of 60 deg sweep model. Shot 2049, Laminar case, $\bar{R}^* = 893.3$, $h_0 = 5.8$ MJ/kg. A set of vertical lines indicate test time determined from the end of starting process and the start of driver gas contamination[54]. The upper horizontal line denotes the theoretical turbulent heat flux (eq. 4.3), while the lower line the theoretical laminar heat flux (eq. 4.2)[71].

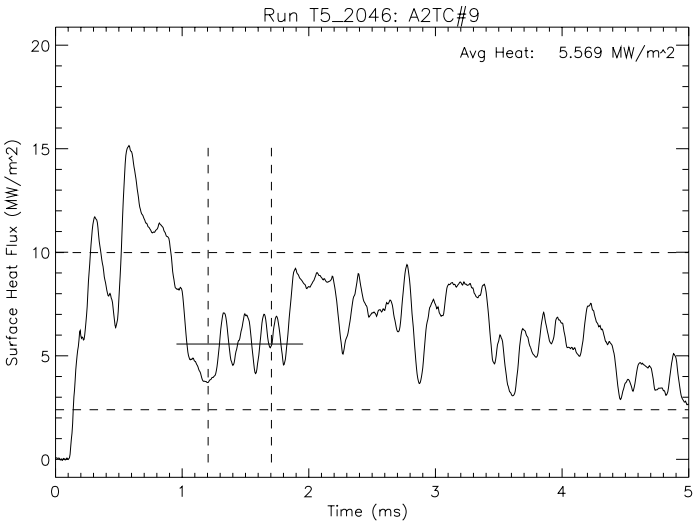

(a)Heat flux trace

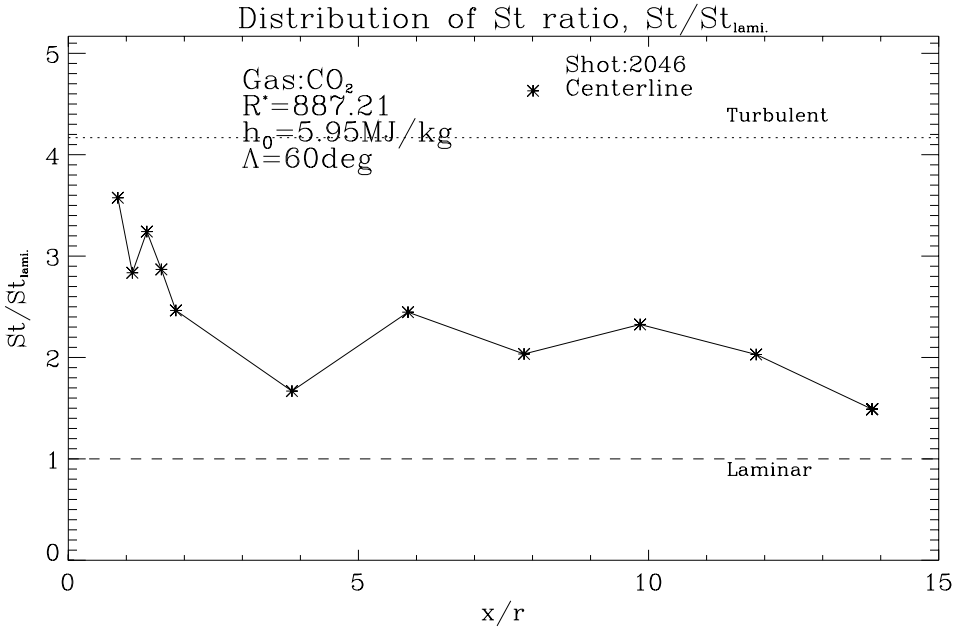

(b)Heat flux distribution at #9 sensor ($x/r \approx 10$)

Figure 6.2: A typical transitional heat flux to the attachment line of 60 deg sweep model. Shot 2046, Intermittent case, $\bar{R}^* = 887.2$, $h_0 = 5.8$ MJ/kg. A set of vertical lines indicate test time determined from the end of starting process and the start of driver gas contamination[54]. The upper horizontal line denotes the theoretical turbulent heat flux (eq. 4.3), while the lower line the theoretical laminar heat flux (eq. 4.2)[71].

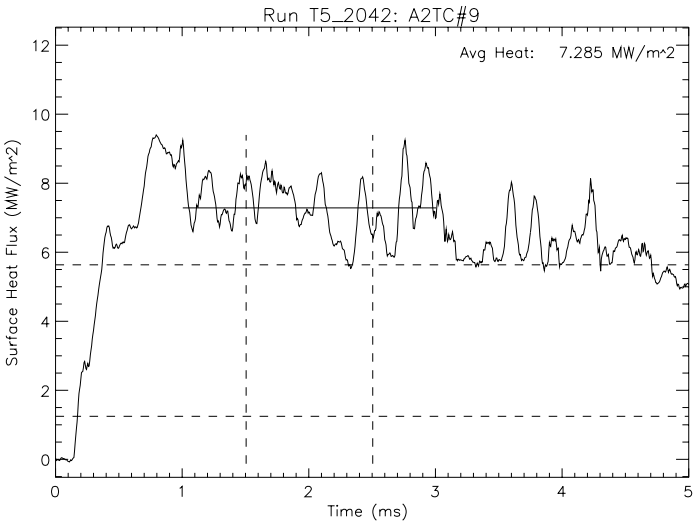

(a)Heat flux trace

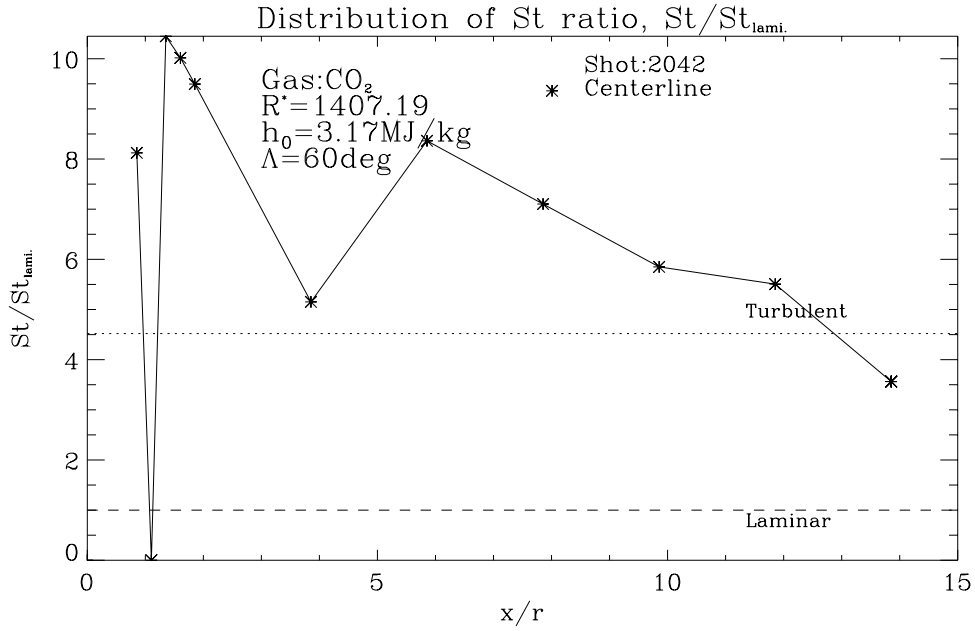

(b)Heat flux distribution at #9 sensor ($x/r \approx 10$)

Figure 6.3: A typical turbulent heat flux to the attachment line of 60 deg sweep model. Shot 2042, Turbulent case, $\bar{R}^* = 1407.2$, $h_0 = 3.0$ MJ/kg. A set of vertical lines indicate test time determined from the end of starting process and the start of driver gas contamination[54]. The upper horizontal line denotes the theoretical turbulent heat flux (eq. 4.3), while the lower line the theoretical laminar heat flux (eq. 4.2)[71].

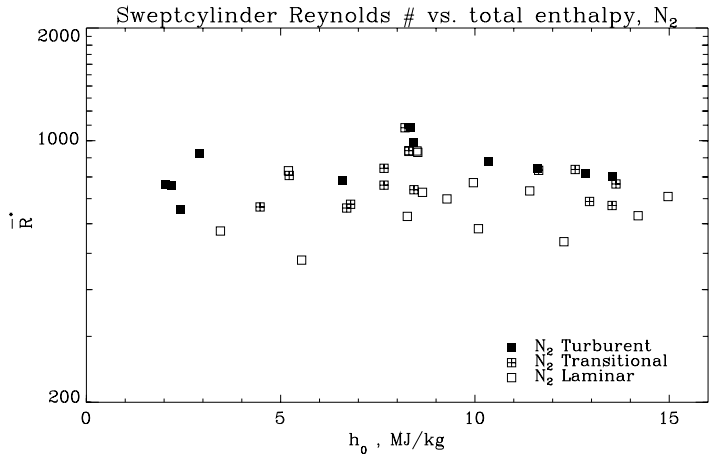

(a) N_2

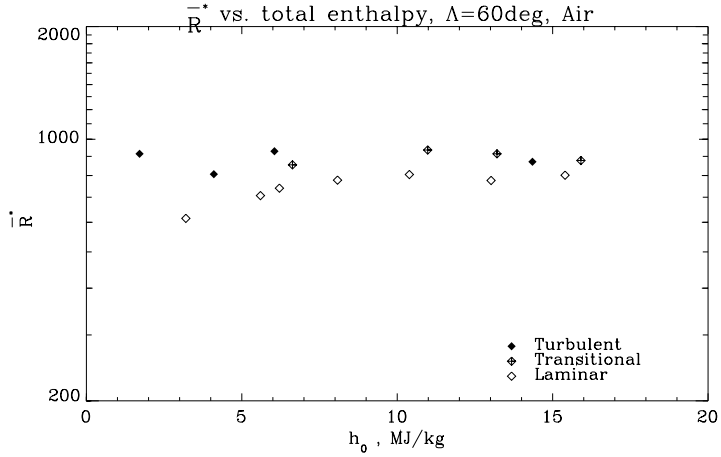

(b) Air

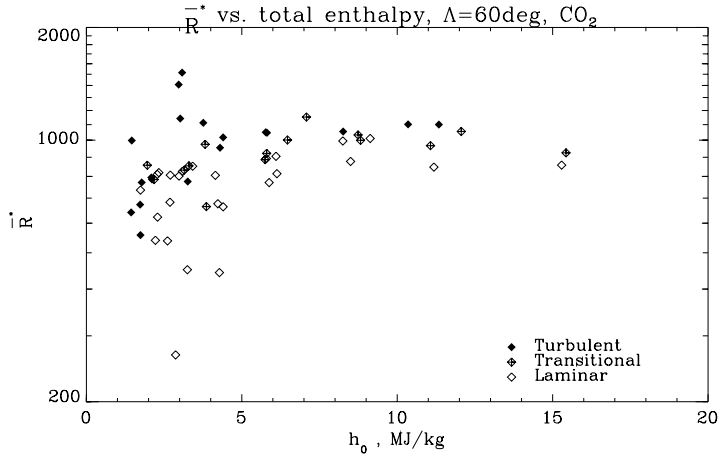

(c) CO_2

Figure 6.4: Reynolds number $\bar{R}_t^*$ versus total enthalpy for nitrogen, air, and carbon dioxide observed on the $\Lambda = 60$ deg model. Solid symbols indicate turbulent cases, open symbols laminar, and symbols with '+' indicate transitional cases. No significant dependence is evident for nitrogen and air, while a strong effect is seen clearly for carbon dioxide tests in the enthalpy range of $h_0 = 1$ MJ/kg to 7 MJ/kg.

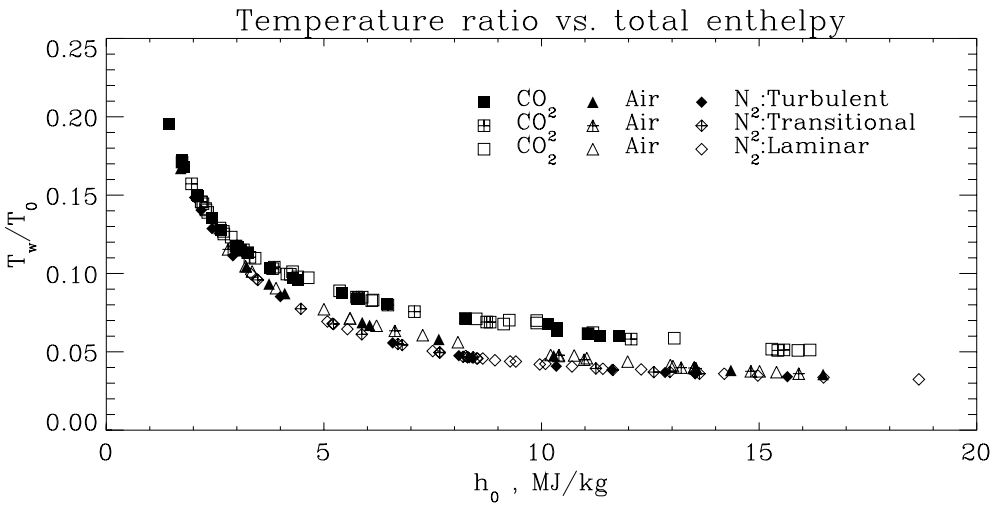

Figure 6.5: The ratio of the wall temperature and the stagnation temperature. The wall temperature is assumed constant at 300 K. No significant difference is visible for different test gas species used compared with the variation due to total enthalpy variation.

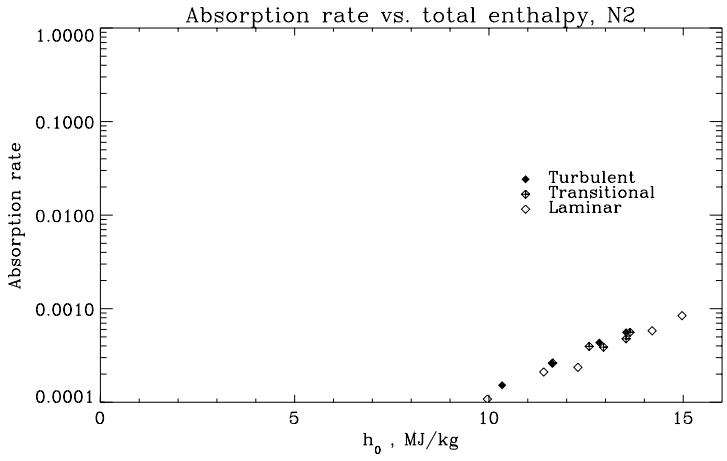

(a) N_2

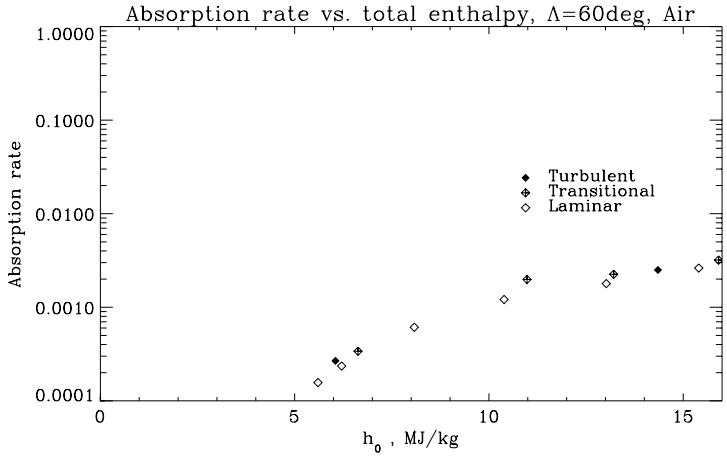

(b) Air

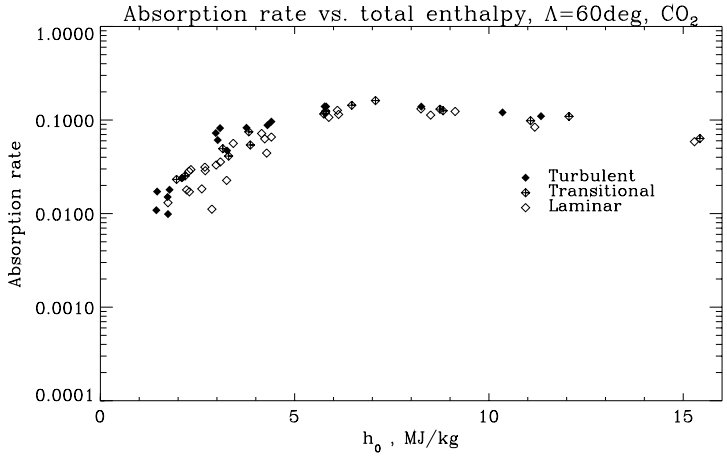

(c) CO_2

Figure 6.6: Sound attenuation rate per wave length evaluated at the reference enthalpy conditions versus total enthalpy for $\Lambda = 60$ deg model.

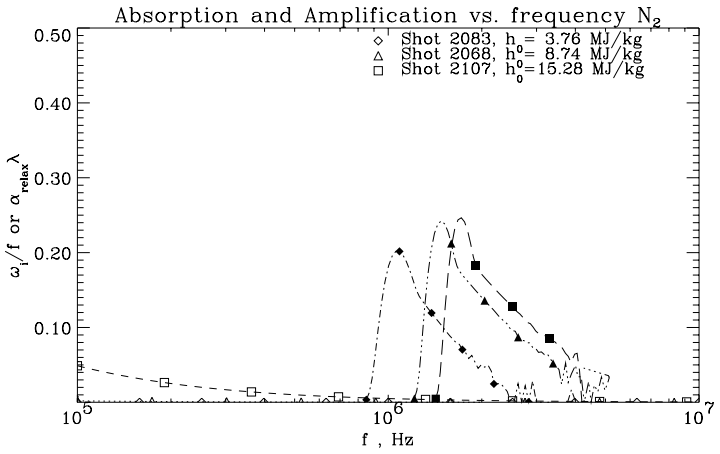

(a) N_2

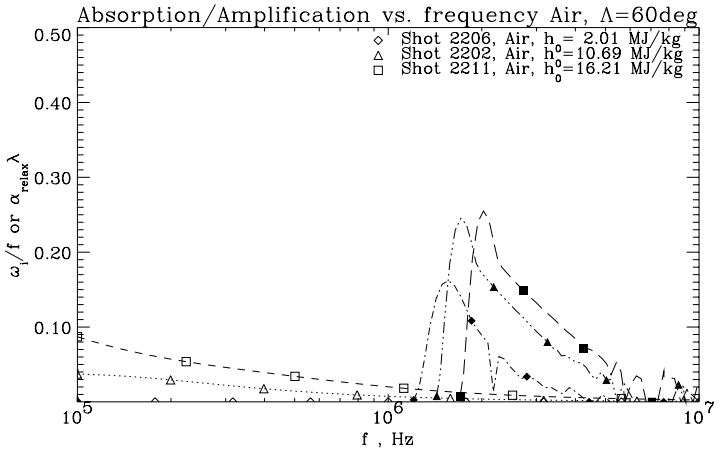

(b) Air

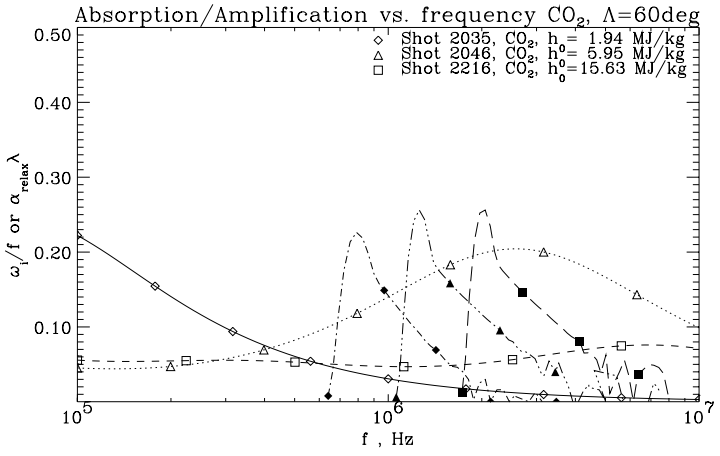

(c) CO_2

Figure 6.7: Comparisons of the absorption rate per wave length due to relaxation (open symbols) with the amplification rate per cycle from perfect-gas linear stability calculations (solid symbols) for several particular T5 shots at 60 deg sweep angle.

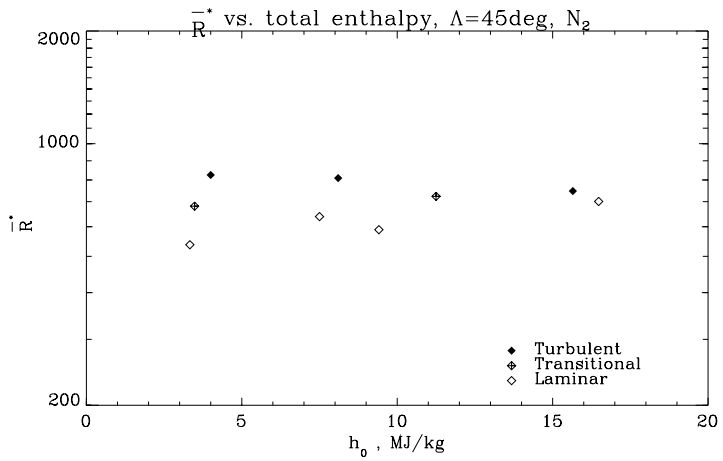

(a) N_2

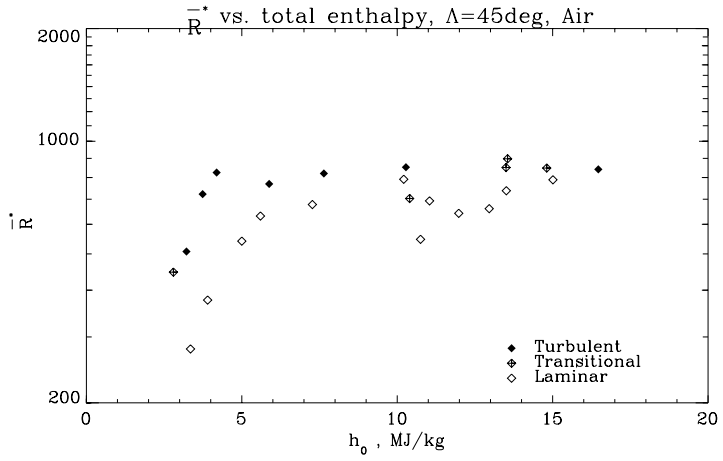

(b) Air

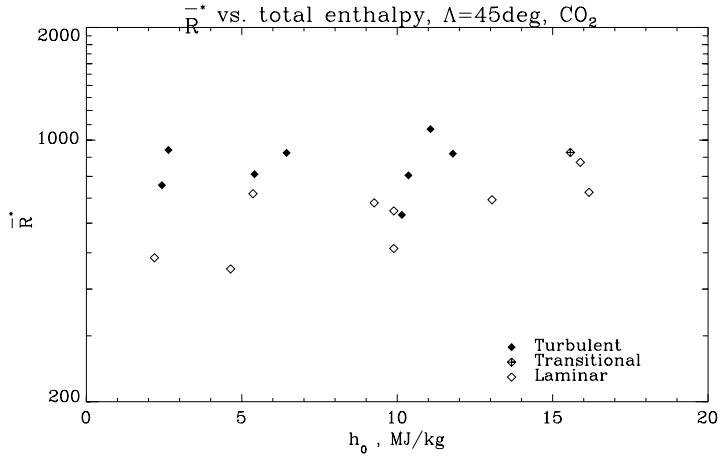

(c) CO_2

Figure 6.8: Reynolds number $\bar{R}_t^*$ versus total enthalpy for nitrogen, air, and carbon dioxide observed on the $\Lambda = 45$ deg model. Solid symbols indicate turbulent cases, open symbols laminar, and symbols with '+' indicate transitional cases.

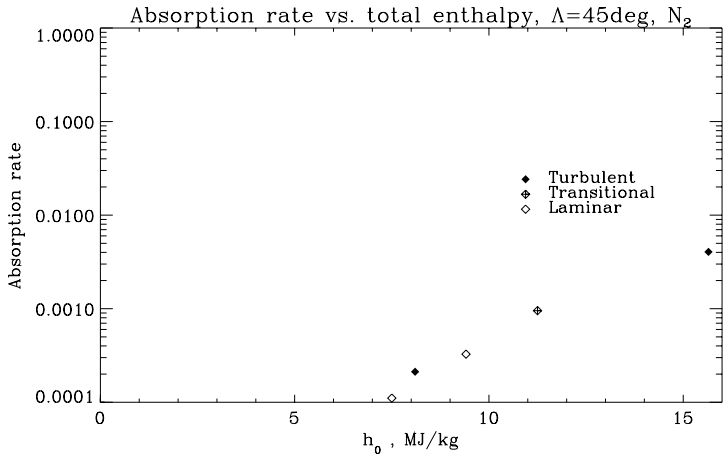

(a) N_2

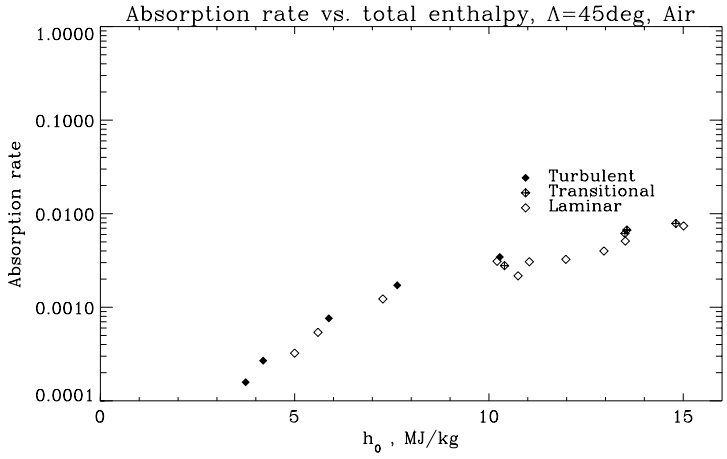

(b) Air

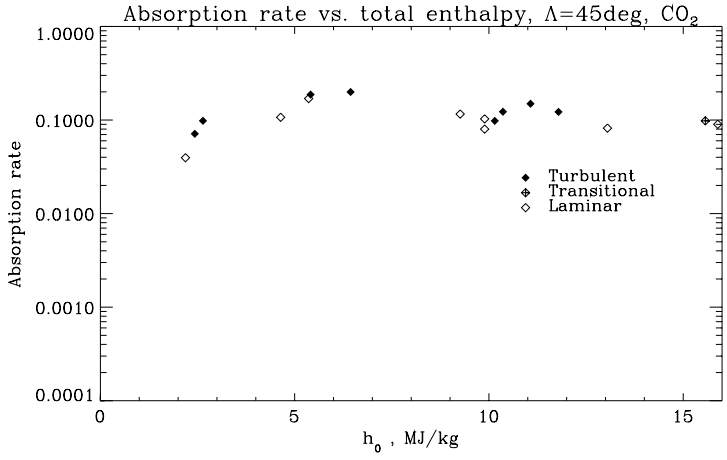

(c) CO_2

Figure 6.9: Sound attenuation rate per wave length evaluated at reference enthalpy conditions versus total enthalpy for $\Lambda = 45$ deg model.

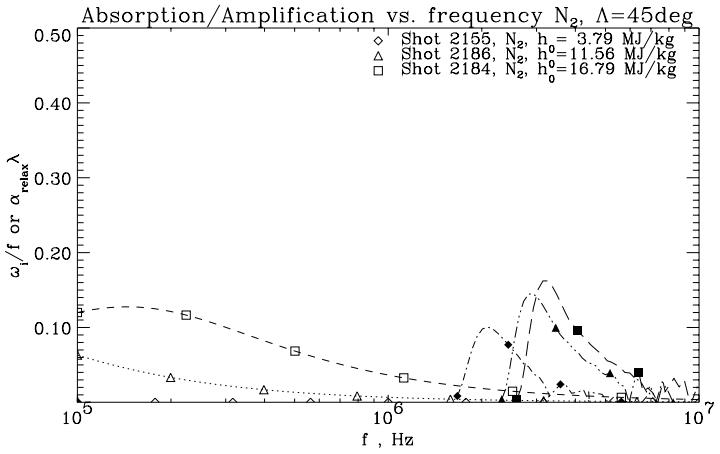

(a) N_2

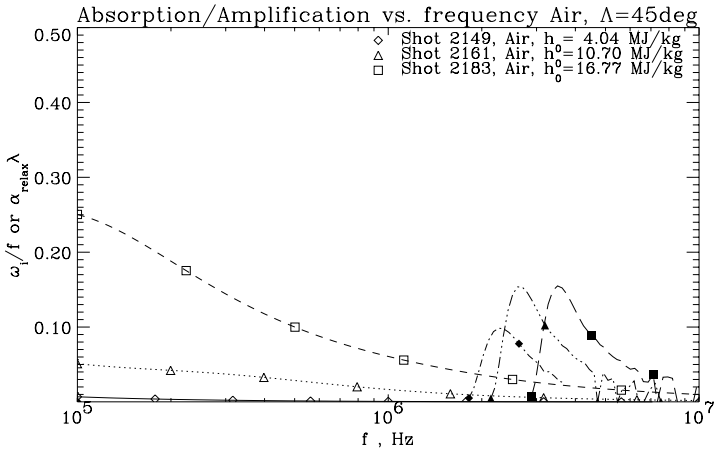

(b) Air

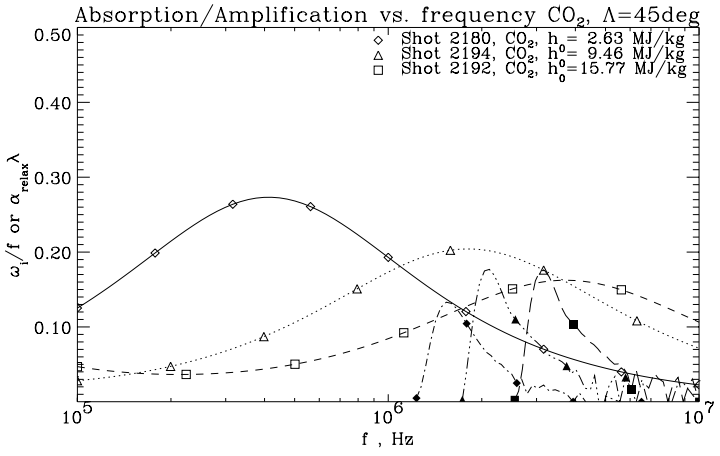

(c) CO_2

Figure 6.10: Comparisons of the absorption rate per wave length due to relaxation (open symbols) with the amplification rate per cycle from perfect-gas linear stability calculations (solid symbols) for several particular T5 shots at 45 deg sweep angle.

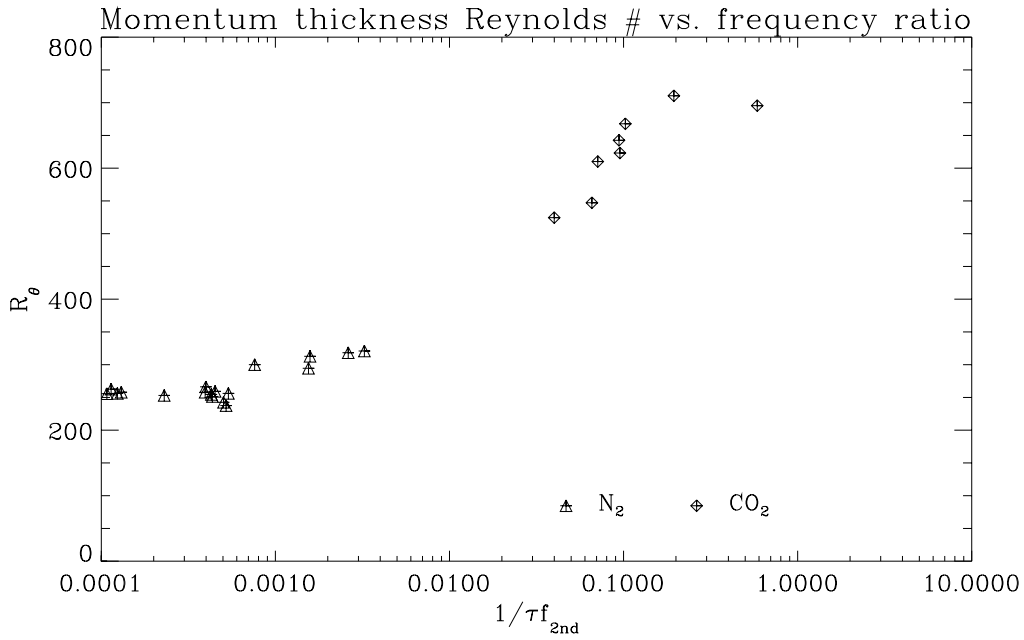

Figure 6.11: Transition Reynolds number based on the momentum thickness calculated with the BLIMPK code versus the ratio of the characteristic frequencies, equation (2.6) in the previous T5 experiment on 5 deg half-angle sharp cone. Based on the data taken from Rasheed[39], the momentum thickness Reynolds number is calculated.

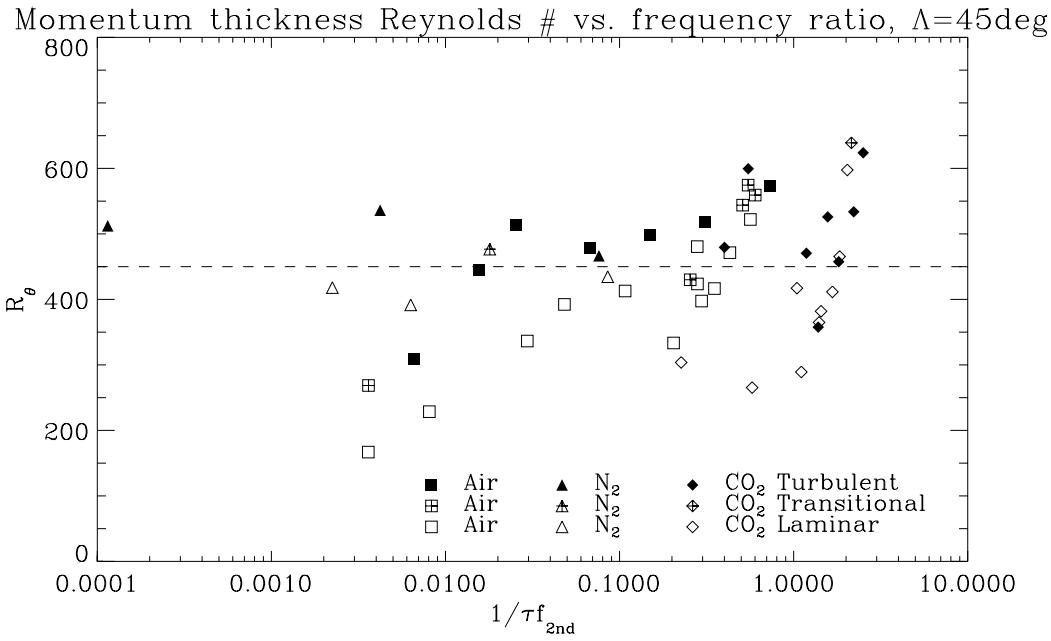

(a) Λ =45 deg

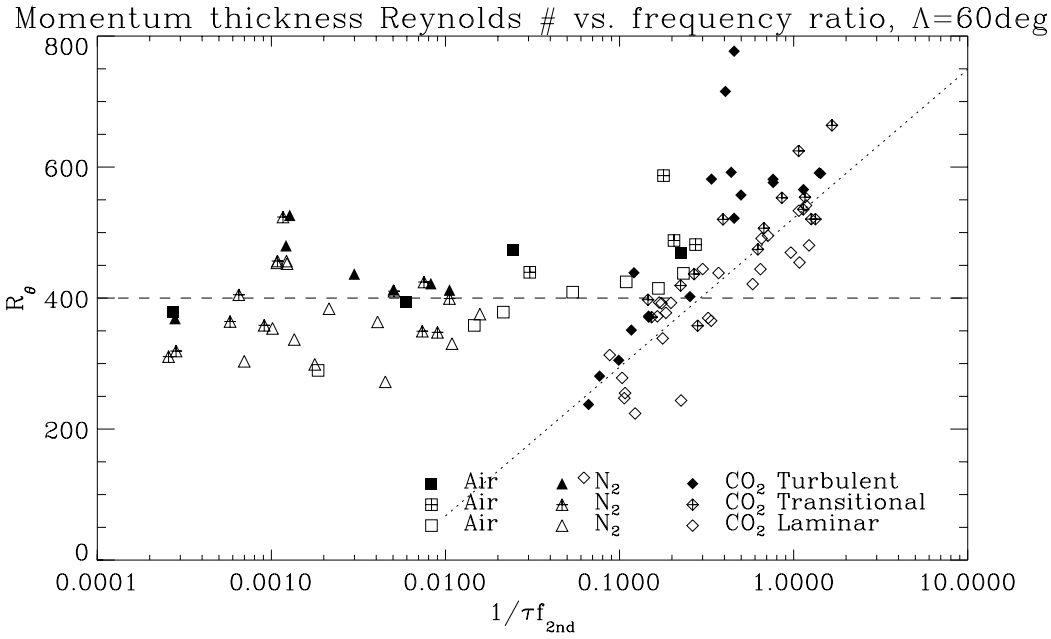

(b) Λ =60 deg

Figure 6.12: Re-plot of transition Reynolds number in terms of momentum thickness Reynolds number versus the frequencies ratio (equation (2.6)).

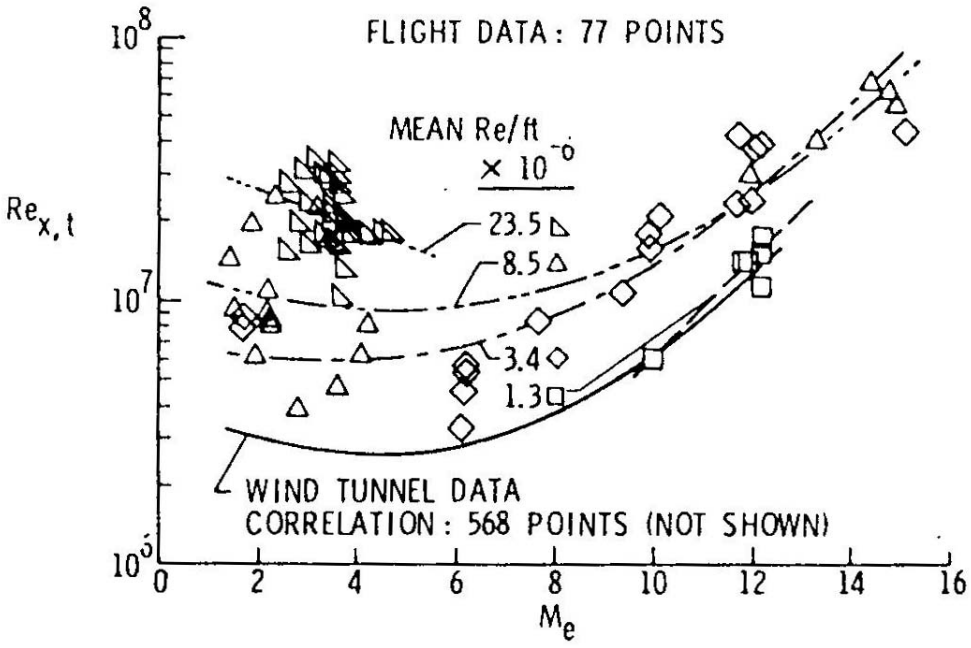

Figure 6.13: Correlation of transition Reynolds number data on sharp cones in wind tunnel and flight with edge Mach number. Taken from Beckwith[85].

Appendix

Appendix A Boundary Layer Transition Observed in Hypersonic Flight Experiment

This section briefly describes an event that makes the author interested in the field of the present study. The details can be found through the articles by the author and co-workers[5,6,93]. A series of experimental flight test vehicles had been launched to gather aero- and aerothermo-dynamic data as well as other important data for the establishment of design technology of a re-entering operational vehicle in Japan. Hypersonic Flight Experiment is one of the programs particularly aiming at acquiring an experience of hypersonic lifting body design and information on relevant technical problems. On its design phase, it had been believed that the boundary layer would stay laminar during hypersonic speed regime because the Reynolds number based on vehicle length (4 m) and on freestream condition is predicted much lower than the Reynolds number at which U.S. space shuttle first experiences boundary layer transition on its re-entering flight path. In addition, hypersonic wind tunnel tests at approximately the same Mach number and Reynolds number as the planned flight condition indicated no clear evidence of boundary layer transition (figure A.1(a)). On-board measurement of aerodynamic heating however showed a violent increase in heating to windward body surface(figure A.1(b),(c)), which was identified later as the occurrence of boundary layer transition. Attempts to explain the unexpected 'early' transition had been made, and they suggested that the transition could be caused by disturbances such as surface roughness since gaps or steps between ceramic tiles covering windward surface of the vehicle are found to possibly exceed the critical height for transition. However, the cause has not been fully understood yet since it was reported that the transition in flight environment is, generally speaking, delayed due to less freestream turbulence than that in wind tunnel conditions, while the above case showed the opposite tendency, *i.e.*, promotion of transition. One may thus have a question about a role of high temperature gas effects on transition, which has not been taken into account in the above considerations. This flight conditions however is expected to provide different mechanisms from the present experiment, since the edge Mach number, which determines unstable mode in the boundary layer, is even lower due to high angles of attack than the present study.

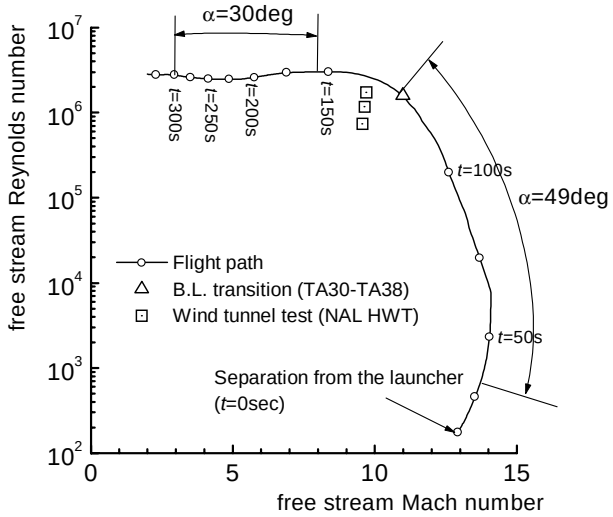

(a)Variation in Reynolds number and Mach number along flight path of HYFLEX

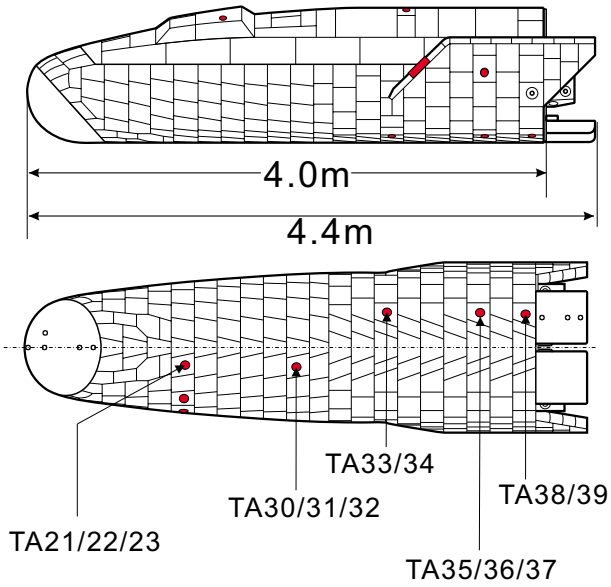

(b)Locations of heat flux sensors on HYFLEX

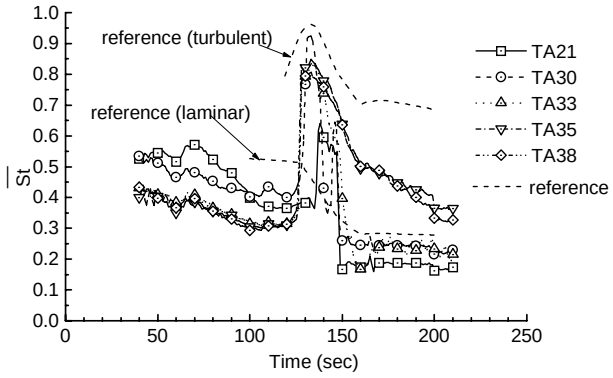

(c)Traces of normalized Stanton number to windward surface of HYFLEX

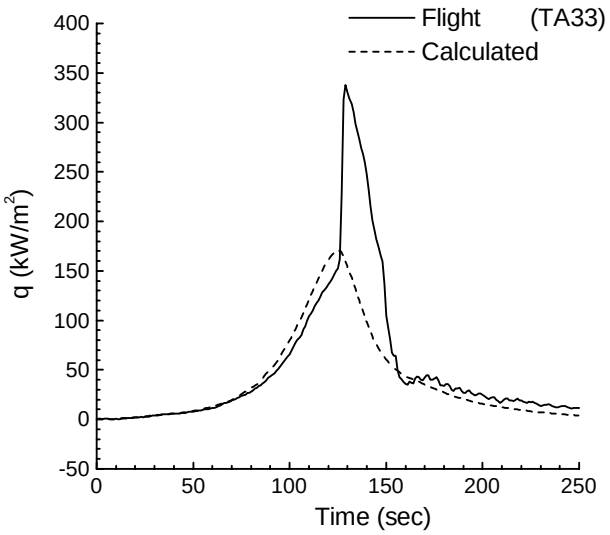

(d)Traces of heating rate measured at TA33 sensor, in kW/m^2

Figure A.1: Boundary layer transition experienced during HYFLEX flight. Figures are taken from Fujii *et al.*[5]

Appendix B Test Conditions

Stagnation conditions (both measured quantities and calculation), freestream conditions calculated with NENZF code, conditions at the boundary layer edge, reference conditions of each shot are presented in this section.

B.1 Air shots

Table B.1: Stagnation and freestream conditions for air shots. From measured stagnation pressure P_0 and shock velocity in the shock tube V_{shock}, stagnation conditions are calculated (such as T_0 and its composition). Freestream conditions were computed with NENZF non-equilibrium nozzle code, where vibrational equilibrium was assumed. M_∞ denotes frozen freestream Mach number.

shot	P_0 MPa	V_{shock} km/s	T_0 K	T_∞ K	p_∞ kPa	ρ_∞ kg/m^3	u_∞ km/s	M_∞	μ_∞ kg/m s
					$\Lambda = 60$ deg				
2199	38.24	2.61	4728	870	12.07	4.82×10^{-2}	3.40	5.85	3.92×10^{-5}
2200	27.52	2.48	4500	797	8.42	3.67×10^{-2}	3.30	5.92	3.70×10^{-5}
2201	64.94	3.31	6667	1661	25.81	5.34×10^{-2}	4.25	5.33	5.98×10^{-5}
2202	46.71	3.24	6339	1538	18.18	4.05×10^{-2}	4.14	5.38	5.69×10^{-5}
2203	68.28	3.61	7512	1994	28.12	4.77×10^{-2}	4.59	5.22	6.77×10^{-5}
2204	11.85	1.83	2868	350	2.75	2.73×10^{-2}	2.45	6.54	2.09×10^{-5}
2205	48.83	3.61	7342	1909	19.83	3.49×10^{-2}	4.55	5.26	6.59×10^{-5}
2206	15.46	1.32	1796	186	3.17	5.94×10^{-2}	1.90	6.95	1.27×10^{-5}
2207	42.28	2.43	4481	772	12.69	5.72×10^{-2}	3.27	5.95	3.62×10^{-5}
2208	23.33	2.42	4209	696	6.79	3.40×10^{-2}	3.15	6.03	3.38×10^{-5}
2209	64.33	3.80	7856	2129	26.74	4.19×10^{-2}	4.76	5.19	7.09×10^{-5}
2210	24.73	2.04	3439	466	6.23	4.66×10^{-2}	2.73	6.34	2.57×10^{-5}
2211	68.54	3.92	8310	2324	28.91	4.10×10^{-2}	4.97	5.15	7.53×10^{-5}
2212	56.25	3.92	8101	2214	23.33	3.47×10^{-2}	4.89	5.19	7.30×10^{-5}
2213	38.10	2.87	5343	1131	12.92	3.96×10^{-2}	3.72	5.64	4.65×10^{-5}
					$\Lambda = 45$ deg				
2148	28.55	2.01	3491	501	8.57	5.96×10^{-2}	2.75	6.16	2.70×10^{-5}
2149	20.35	1.92	3216	437	5.85	4.66×10^{-2}	2.62	6.26	2.46×10^{-5}
2150	6.31	1.83	2599	319	1.66	1.82×10^{-2}	2.32	6.47	1.95×10^{-5}
2151	9.03	1.89	2878	369	2.47	2.34×10^{-2}	2.45	6.38	2.18×10^{-5}

continued on next page

continued from previous page (Table B.1)

shot	P_0 MPa	V_{shock} km/s	T_0 K	T_∞ K	p_∞ kPa	ρ_∞ kg/m^3	u_∞ km/s	M_∞	μ_∞ kg/m s
2152	9.64	1.92	2962	224	0.40	6.21×10^{-3}	2.56	8.51	1.48×10^{-5}
2153	19.60	1.99	3310	266	0.85	1.12×10^{-2}	2.73	8.34	1.70×10^{-5}
2159	26.88	2.77	4947	1018	10.46	3.56×10^{-2}	3.52	5.62	4.34×10^{-5}
2160	41.76	2.83	5175	1097	16.15	5.11×10^{-2}	3.62	5.57	4.56×10^{-5}
2161	35.01	3.33	6272	1569	15.83	3.44×10^{-2}	4.11	5.28	5.78×10^{-5}
2162	34.95	3.39	6528	1663	16.06	3.28×10^{-2}	4.21	5.24	6.01×10^{-5}
2163	21.51	3.41	6290	1545	9.55	2.08×10^{-2}	4.14	5.31	5.74×10^{-5}
2164	31.35	3.49	6851	1763	14.40	2.74×10^{-2}	4.35	5.23	6.26×10^{-5}
2165	66.50	3.64	7618	2112	32.27	5.14×10^{-2}	4.62	5.09	7.03×10^{-5}
2166	59.55	3.64	7563	2079	28.58	4.62×10^{-2}	4.61	5.11	6.97×10^{-5}
2167	34.75	3.66	7219	1898	16.11	2.82×10^{-2}	4.51	5.19	6.58×10^{-5}
2168	44.59	3.73	7474	2019	21.05	3.47×10^{-2}	4.60	5.15	6.85×10^{-5}
2169	51.43	3.17	6318	1585	23.33	5.06×10^{-2}	4.10	5.27	5.80×10^{-5}
2170	54.58	3.87	7984	2243	26.37	3.88×10^{-2}	4.82	5.09	7.35×10^{-5}
2171	62.80	3.85	7981	2256	30.53	4.49×10^{-2}	4.80	5.08	7.37×10^{-5}
2172	13.97	2.34	3886	624	4.47	2.49×10^{-2}	2.98	6.00	3.14×10^{-5}
2173	30.59	2.47	4368	777	10.73	4.80×10^{-2}	3.21	5.84	3.64×10^{-5}
2174	20.17	2.45	4198	725	6.86	3.29×10^{-2}	3.14	5.89	3.47×10^{-5}
2182	44.02	3.19	6250	1562	19.94	4.38×10^{-2}	4.09	5.28	5.75×10^{-5}
2183	66.19	4.03	8438	2461	32.68	4.34×10^{-2}	5.02	5.04	7.83×10^{-5}

Table B.2: Freestream mole fraction for Air shots computed with NENZF code.

shot	x_{N_2}	x_{O_2}	x_{AR}	x_N	x_O	x_{NO}
	Λ =60 deg					
2199	0.7508	0.1796	0.0093	0.0000	0.0035	0.0568
2200	0.7505	0.1791	0.0093	0.0000	0.0038	0.0574
2201	0.7413	0.1647	0.0092	0.0000	0.0295	0.0554
2202	0.7404	0.1632	0.0092	0.0000	0.0314	0.0558
2203	0.7311	0.1475	0.0091	0.0000	0.0600	0.0524
2204	0.7611	0.1899	0.0093	0.0000	0.0004	0.0393
2205	0.7266	0.1402	0.0090	0.0000	0.0725	0.0517
2206	0.7786	0.2076	0.0093	0.0000	0.0000	0.0045
2207	0.7524	0.1814	0.0093	0.0000	0.0018	0.0551
2208	0.7511	0.1799	0.0093	0.0000	0.0026	0.0570
2209	0.7232	0.1346	0.0089	0.0000	0.0832	0.0502
2210	0.7528	0.1816	0.0093	0.0000	0.0004	0.0559
2211	0.7143	0.1200	0.0088	0.0000	0.1093	0.0475
2212	0.7137	0.1190	0.0088	0.0000	0.1112	0.0474
2213	0.7472	0.1742	0.0093	0.0000	0.0115	0.0577
	Λ =45 deg					
2148	0.7536	0.1823	0.0093	0.0000	0.0004	0.0545
2149	0.7556	0.1844	0.0093	0.0000	0.0003	0.0503
2150	0.7664	0.1952	0.0093	0.0000	0.0005	0.0286
2151	0.7606	0.1894	0.0093	0.0000	0.0006	0.0401
2152	0.7588	0.1875	0.0093	0.0000	0.0010	0.0433
2153	0.7525	0.1813	0.0093	0.0000	0.0007	0.0562
2159	0.7477	0.1753	0.0093	0.0000	0.0094	0.0583
2160	0.7488	0.1768	0.0093	0.0000	0.0076	0.0575
2161	0.7368	0.1575	0.0091	0.0000	0.0411	0.0555
2162	0.7331	0.1514	0.0091	0.0000	0.0520	0.0544
2163	0.7274	0.1421	0.0090	0.0000	0.0678	0.0537
2164	0.7254	0.1385	0.0090	0.0000	0.0748	0.0523
2165	0.7285	0.1432	0.0090	0.0000	0.0675	0.0518
2166	0.7269	0.1408	0.0090	0.0000	0.0718	0.0515
2167	0.7206	0.1305	0.0089	0.0000	0.0895	0.0506
2168	0.7216	0.1321	0.0089	0.0000	0.0871	0.0504
2169	0.7419	0.1655	0.0092	0.0000	0.0274	0.0560
2170	0.7154	0.1219	0.0088	0.0000	0.1056	0.0482
2171	0.7195	0.1286	0.0089	0.0000	0.0937	0.0493
2172	0.7501	0.1789	0.0093	0.0000	0.0029	0.0588
2173	0.7516	0.1804	0.0093	0.0000	0.0024	0.0563
2174	0.7506	0.1793	0.0093	0.0000	0.0032	0.0576
2182	0.7405	0.1635	0.0092	0.0000	0.0308	0.0560
2183	0.7094	0.1120	0.0088	0.0000	0.1236	0.0462

Table B.3: Summary of the relevant parameters for the Air shots. θ denotes momentum thickness, δ_{99} does boundary layer thickness where local velocity reaches 99% of edge velocity both computed from BLIMPK code. R_θ for Reynolds number based on θ, $f_{2\mathrm{nd}}$ for the estimated most strongry amplified 2nd mode frequency. "L", "Tr" and "T" in "BL" column denote the boundary layer states, which are "Laminar", "Transitional" and "Turbulent" respectively.

Shot	$\bar{R}^*$	h_0 MJ/kg	η^* mm	U_e km/s	M_e	θ mm	δ_{99} mm	R_θ	$f_{2\mathrm{nd}}$ MHz	BL
					$\Lambda = 60$ deg					
2199	854	6.93	0.081	2.95	3.25	0.041	0.26	439	5.62	Tr
2200	740	6.51	0.093	2.86	3.24	0.047	0.30	379	4.74	L
2201	936	11.28	0.076	3.68	3.30	0.047	0.30	587	6.11	Tr
2202	805	10.69	0.087	3.58	3.28	0.046	0.28	425	6.36	L
2203	914	13.51	0.079	3.98	3.33	0.042	0.25	488	7.88	Tr
2204	614	3.50	0.110	2.12	3.20	0.052	0.36	290	2.99	L
2205	776	13.32	0.092	3.94	3.32	0.049	0.30	415	6.65	L
2206	914	2.01	0.077	1.65	3.27	0.032	0.25	379	3.36	T
2207	929	6.35	0.074	2.83	3.25	0.038	0.24	473	5.88	T
2208	707	5.90	0.097	2.73	3.23	0.049	0.31	358	4.34	L
2209	871	14.65	0.083	4.12	3.34	0.045	0.27	469	7.72	T
2210	807	4.40	0.084	2.37	3.20	0.041	0.27	395	4.37	T
2211	877	16.21	0.083	4.30	3.34	0.045	0.27	482	8.02	Tr
2212	802	15.70	0.090	4.24	3.33	0.049	0.29	438	7.24	L
2213	778	8.38	0.089	3.22	3.25	0.047	0.29	409	5.52	L
					$\Lambda = 45$ deg					
2148	825	4.49	0.054	1.95	2.14	0.034	0.19	513	5.26	T
2149	722	4.04	0.062	1.85	2.13	0.038	0.21	445	4.40	T
2150	447	3.10	0.099	1.64	2.11	0.060	0.34	269	2.41	Tr
2151	507	3.52	0.087	1.73	2.12	0.053	0.30	309	2.91	T
2152	279	3.65	0.164	1.81	2.21	0.098	0.56	167	1.62	L
2153	376	4.20	0.122	1.93	2.22	0.074	0.42	229	2.32	L
2159	678	7.57	0.070	2.49	2.25	0.043	0.23	413	5.49	L
2160	820	7.94	0.058	2.56	2.27	0.035	0.19	498	6.80	T
2161	703	10.70	0.070	2.91	2.31	0.043	0.22	430	6.57	Tr
2162	693	11.34	0.071	2.98	2.31	0.043	0.22	424	6.62	L
2163	547	11.05	0.090	2.93	2.30	0.055	0.28	334	5.19	L
2164	642	12.28	0.077	3.08	2.31	0.047	0.24	398	6.33	L
2165	898	13.85	0.055	3.27	2.30	0.035	0.18	574	9.20	Tr
2166	851	13.80	0.058	3.26	2.30	0.037	0.19	544	8.71	Tr
2167	660	13.26	0.075	3.19	2.30	0.047	0.24	417	6.68	L
2168	738	13.81	0.067	3.25	2.30	0.043	0.21	471	7.56	L
2169	852	10.58	0.058	2.90	2.31	0.035	0.18	518	7.91	T
2170	789	15.31	0.062	3.41	2.28	0.041	0.20	522	8.37	L

continued on next page

continued from previous page (Table B.3)

Shot	$\bar{R}^*$	h_0 MJ/kg	η^* mm	U_e km/s	M_e	θ mm	δ_{99} mm	R_θ	$f_{2\text{nd}}$ MHz	BL
2171	848	15.11	0.058	3.39	2.28	0.038	0.19	559	8.95	Tr
2172	541	5.30	0.084	2.11	2.17	0.052	0.28	336	3.72	L
2173	769	6.18	0.060	2.27	2.20	0.037	0.20	478	5.66	T
2174	631	5.90	0.073	2.22	2.19	0.045	0.24	392	4.55	L
2182	791	10.51	0.062	2.89	2.31	0.038	0.20	481	7.36	L
2183	841	16.77	0.058	3.55	2.26	0.039	0.19	573	9.19	T

Table B.4: Summary of reference conditions and mole fractions at the wall for the Air shots. Wall temperature was assumed constant at 300 K.

Shot	p^* Pa	T^* K	ρ^* kg/m^3	μ^* kg/sm	h_w MJ/kg	$x_{N_2,w}$	$x_{O_2,w}$	$x_{NO,w}$
				$\Lambda = 60$ deg				
2199	134.9	1962.47	0.2395	6.65×10^{-5}	0.32	0.780	0.221	0.000
2200	96.3	1864.28	0.1799	6.44×10^{-5}	0.33	0.780	0.220	0.000
2201	239.4	2874.01	0.2873	8.54×10^{-5}	0.33	0.780	0.220	0.000
2202	171.8	2767.82	0.2146	8.33×10^{-5}	0.32	0.774	0.226	0.000
2203	252.5	3190.30	0.2685	9.17×10^{-5}	0.32	0.767	0.233	0.000
2204	38.8	1116.78	0.1210	4.62×10^{-5}	0.32	0.783	0.217	0.000
2205	180.5	3146.25	0.1944	9.09×10^{-5}	0.26	0.770	0.230	0.000
2206	50.7	711.09	0.2484	3.44×10^{-5}	0.32	0.786	0.214	0.000
2207	147.3	1824.25	0.2812	6.35×10^{-5}	0.33	0.780	0.220	0.000
2208	80.7	1718.40	0.1637	6.11×10^{-5}	0.32	0.780	0.220	0.000
2209	238.4	3319.05	0.2409	9.44×10^{-5}	0.32	0.764	0.236	0.000
2210	82.3	1351.02	0.2122	5.22×10^{-5}	0.32	0.782	0.218	0.000
2211	255.1	3486.48	0.2417	9.79×10^{-5}	0.33	0.762	0.238	0.000
2212	208.8	3416.36	0.2025	9.65×10^{-5}	0.32	0.761	0.239	0.000
2213	133.4	2310.13	0.2010	7.40×10^{-5}	0.35	0.777	0.221	0.000
				$\Lambda = 45$ deg				
2148	213.4	1618.71	0.4592	5.87×10^{-5}	0.32	0.781	0.219	0.000
2149	150.4	1485.90	0.3527	5.56×10^{-5}	0.32	0.781	0.219	0.000
2150	45.7	1196.45	0.1330	4.83×10^{-5}	0.32	0.783	0.218	0.000
2151	66.0	1327.05	0.1732	5.16×10^{-5}	0.32	0.782	0.218	0.000
2152	18.9	1346.19	0.0489	5.21×10^{-5}	0.32	0.781	0.219	0.000
2153	38.8	1509.71	0.0896	5.61×10^{-5}	0.32	0.781	0.219	0.000
2159	213.4	2466.99	0.3008	7.72×10^{-5}	0.32	0.788	0.212	0.000
2160	323.4	2567.42	0.4378	7.92×10^{-5}	0.32	0.774	0.226	0.000
2161	284.6	3108.76	0.3126	9.00×10^{-5}	0.31	0.764	0.235	0.000
2162	285.0	3206.78	0.3017	9.20×10^{-5}	0.32	0.762	0.238	0.000
2163	174.6	3131.92	0.1891	9.06×10^{-5}	0.32	0.762	0.238	0.000
2164	254.6	3325.84	0.2569	9.45×10^{-5}	0.32	0.759	0.241	0.000
2165	540.7	3596.60	0.4990	9.97×10^{-5}	0.32	0.757	0.243	0.000
2166	482.7	3577.32	0.4477	9.94×10^{-5}	0.32	0.757	0.244	0.000
2167	281.4	3456.48	0.2703	9.72×10^{-5}	0.32	0.757	0.243	0.000
2168	360.9	3547.95	0.3364	9.89×10^{-5}	0.32	0.756	0.244	0.000
2169	417.0	3108.12	0.4598	8.99×10^{-5}	0.32	0.766	0.234	0.000
2170	442.5	3744.99	0.3844	1.03×10^{-4}	0.32	0.753	0.247	0.000
2171	508.8	3740.14	0.4444	1.03×10^{-4}	0.32	0.754	0.246	0.000
2172	105.1	1858.29	0.1970	6.42×10^{-5}	0.32	0.779	0.221	0.000
2173	237.2	2102.24	0.3929	6.96×10^{-5}	0.32	0.780	0.220	0.000
2174	154.7	2025.84	0.2660	6.79×10^{-5}	0.33	0.778	0.222	0.000
2182	357.8	3089.21	0.3968	8.96×10^{-5}	0.32	0.766	0.235	0.000

continued on next page

continued from previous page (Table B.4)

Shot	p^* Pa	T^* K	ρ^* kg/m^3	μ^* kg/sm	h_w MJ/kg	$x_{\mathrm{N}_2,w}$	$x_{\mathrm{O}_2,w}$	$x_{\mathrm{NO},w}$
2183	537.7	3936.03	0.4375	1.07×10^{-4}	0.32	0.752	0.248	0.000

B.2 N_2 shots

Table B.5: Stagnation and freestream conditions for nitrogen shots. From measured stagnation pressure P_0 and shock velocity in the shock tube V_{shock}, stagnation conditions are calculated (such as T_0 and its composition). Freestream conditions were computed with NENZF non-equilibrium nozzle code, where vibrational equilibrium was assumed. M_∞ denotes frozen freestream Mach number.

shot	P_0 MPa	V_{shock} km/s	T_0 K	T_∞ K	p_∞ kPa	ρ_∞ kg/m^3	u_∞ km/s	M_∞	μ_∞ kg/m s
					$\Lambda = 60$ deg				
2066	71.87	2.78	6317	1012	21.02	7.00×10^{-2}	3.81	6.00	3.97×10^{-5}
2067	53.10	2.71	6270	1012	15.85	5.28×10^{-2}	3.80	5.98	3.96×10^{-5}
2068	33.28	2.87	6301	1012	9.72	3.23×10^{-2}	3.83	6.03	3.97×10^{-5}
2069	23.56	2.90	6179	989	6.85	2.33×10^{-2}	3.79	6.04	3.90×10^{-5}
2070	33.01	2.93	6409	1043	9.70	3.13×10^{-2}	3.88	6.02	4.05×10^{-5}
2071	53.65	2.77	6400	1044	15.98	5.16×10^{-2}	3.85	5.98	4.05×10^{-5}
2072	70.35	2.75	6232	991	20.49	6.97×10^{-2}	3.78	6.01	3.91×10^{-5}
2073	57.11	3.39	7701	1517	19.00	4.22×10^{-2}	4.46	5.79	5.27×10^{-5}
2074	62.9	3.53	8012	1677	21.58	4.33×10^{-2}	4.62	5.72	5.66×10^{-5}
2075	61.18	3.53	8075	1728	21.45	4.18×10^{-2}	4.66	5.68	5.78×10^{-5}
2076	25.75	3.57	7660	1638	8.93	1.83×10^{-2}	4.55	5.69	5.56×10^{-5}
2077	62.37	3.61	8263	1852	22.34	4.06×10^{-2}	4.77	5.62	6.07×10^{-5}
2078	43.85	3.55	7997	1756	15.61	2.99×10^{-2}	4.67	5.65	5.85×10^{-5}
2079	41.24	3.75	8271	1985	15.42	2.61×10^{-2}	4.85	5.53	6.39×10^{-5}
2080	54.41	2.75	6386	1040	16.19	5.25×10^{-2}	3.84	5.98	4.04×10^{-5}
2081	43.87	3.66	8140	1863	16.04	2.89×10^{-2}	4.75	5.59	6.10×10^{-5}
2082	57.28	3.64	8259	1878	20.88	3.74×10^{-2}	4.78	5.60	6.14×10^{-5}
2083	10.38	1.84	2883	340	2.27	2.25×10^{-2}	2.49	6.62	1.93×10^{-5}
2084	24.04	1.65	2466	277	5.07	6.17×10^{-2}	2.29	6.75	1.70×10^{-5}
2085	13.51	1.44	1898	196	2.70	4.64×10^{-2}	1.99	6.95	1.38×10^{-5}
2086	13.42	1.35	1779	181	2.62	4.87×10^{-2}	1.92	6.99	1.31×10^{-5}
2087	10.89	1.50	2097	224	2.20	3.31×10^{-2}	2.10	6.87	1.49×10^{-5}
2088	52.91	2.71	6269	1009	15.63	5.22×10^{-2}	3.80	5.99	3.96×10^{-5}
2089	33.43	2.52	5178	757	8.34	3.71×10^{-2}	3.40	6.14	3.26×10^{-5}
2091	22.99	2.60	5252	768	5.97	2.62×10^{-2}	3.43	6.16	3.29×10^{-5}
2092	9.99	2.42	4461	613	2.58	1.42×10^{-2}	3.13	6.24	2.83×10^{-5}
2093	32.68	3.06	6705	1136	9.75	2.89×10^{-2}	4.01	5.98	4.30×10^{-5}
2094	58.57	3.26	7701	1509	19.27	4.30×10^{-2}	4.45	5.80	5.25×10^{-5}
2095	56.91	3.17	7240	1298	17.74	4.60×10^{-2}	4.22	5.91	4.72×10^{-5}
2096	59.82	2.83	6341	1025	17.73	5.83×10^{-2}	3.82	5.99	4.00×10^{-5}
2097	40.28	2.75	5883	915	11.54	4.25×10^{-2}	3.66	6.04	3.70×10^{-5}
2098	32.33	2.77	5870	903	9.20	3.43×10^{-2}	3.66	6.08	3.67×10^{-5}
2099	24.49	3.24	6979	1268	7.67	2.04×10^{-2}	4.16	5.90	4.64×10^{-5}

continued on next page

continued from previous page (Table B.5)

shot	P_0 MPa	V_{shock} km/s	T_0 K	T_∞ K	p_∞ kPa	ρ_∞ kg/m^3	u_∞ km/s	M_∞	μ_∞ kg/m s
2100	36.08	3.28	7277	1363	11.52	2.85×10^{-2}	4.28	5.86	4.88×10^{-5}
2101	43.83	3.37	7558	1479	14.39	3.28×10^{-2}	4.41	5.81	5.17×10^{-5}
2102	42.34	3.13	7031	1240	13.06	3.55×10^{-2}	4.14	5.93	4.57×10^{-5}
2103	42.34	2.94	6579	1105	12.81	3.91×10^{-2}	3.93	5.94	4.21×10^{-5}
2104	23.82	2.56	5318	785	6.39	2.74×10^{-2}	3.45	6.13	3.33×10^{-5}
2105	57.52	4.51	9553	3200	26.95	2.77×10^{-2}	5.63	5.04	9.15×10^{-5}
2106	53.71	4.32	9217	2845	23.92	2.79×10^{-2}	5.42	5.16	8.36×10^{-5}
2107	55.02	3.90	8551	2132	21.13	3.33×10^{-2}	4.97	5.47	6.73×10^{-5}
2108	28.68	2.17	4213	567	7.23	4.30×10^{-2}	3.04	6.29	2.69×10^{-5}
2109	16.71	2.13	3659	469	3.94	2.83×10^{-2}	2.82	6.41	2.37×10^{-5}
2110	27.16	2.21	4227	570	6.86	4.06×10^{-2}	3.04	6.28	2.69×10^{-5}
2133	46.87	2.29	4716	659	12.26	6.27×10^{-2}	3.22	6.21	2.97×10^{-5}
2134	36.25	2.22	4123	552	9.08	5.55×10^{-2}	3.00	6.30	2.64×10^{-5}
			$\Lambda = 45$ deg						
2154	9.17	1.90	3013	379	2.53	2.25×10^{-2}	2.54	6.41	2.15×10^{-5}
2155	15.74	1.96	3128	399	4.26	3.60×10^{-2}	2.59	6.37	2.23×10^{-5}
2156	25.73	2.01	3519	468	7.21	5.19×10^{-2}	2.75	6.26	2.50×10^{-5}
2157	43.35	2.83	6308	1068	15.17	4.78×10^{-2}	3.80	5.84	4.33×10^{-5}
2158	26.10	2.79	5938	959	8.42	2.96×10^{-2}	3.68	5.95	4.03×10^{-5}
2184	56.51	4.05	8911	2571	27.45	3.57×10^{-2}	5.18	5.18	7.65×10^{-5}
2185	62.16	3.95	8794	2405	29.19	4.07×10^{-2}	5.08	5.26	7.33×10^{-5}
2186	45.64	3.33	7611	1559	17.66	3.81×10^{-2}	4.42	5.67	5.53×10^{-5}
2187	26.10	3.11	6846	1255	9.43	2.53×10^{-2}	4.08	5.80	4.81×10^{-5}

Table B.6: Freestream mole fraction for N_2 shots computed with NENZF code.

shot	x_{N_2}	x_N
	Λ =60 deg	
2066	0.9999	0.0001
2067	0.9999	0.0001
2068	0.9998	0.0003
2069	0.9996	0.0004
2070	0.9996	0.0003
2071	0.9999	0.0001
2072	0.9999	0.0001
2073	0.9989	0.0011
2074	0.9983	0.0017
2075	0.9979	0.0021
2076	0.9940	0.0060
2077	0.9970	0.0031
2078	0.9962	0.0039
2079	0.9920	0.0081
2080	0.9999	0.0001
2081	0.9948	0.0053
2082	0.9963	0.0037
2083	1.0000	0.0000
2084	1.0000	0.0000
2085	1.0000	0.0000
2086	1.0000	0.0000
2087	1.0001	0.0000
2088	0.9999	0.0001
2089	0.9999	0.0001
2091	0.9999	0.0001
2092	0.9999	0.0001
2093	0.9995	0.0006
2094	0.9990	0.0011
2095	0.9996	0.0005
2096	0.9999	0.0001
2097	1.0000	0.0001
2098	0.9999	0.0001
2099	0.9984	0.0016
2100	0.9987	0.0013
2101	0.9984	0.0015
2102	0.9994	0.0006
2103	0.9997	0.0003
2104	0.9999	0.0001
2105	0.9489	0.0511
2106	0.9678	0.0323
2107	0.9923	0.0077
2108	1.0000	0.0000

continued on next page

continued from previous page (Table B.6)		
shot	x_{N_2}	x_N
2109	1.0000	0.0000
2110	1.0000	0.0000
2133	1.0000	0.0000
2134	1.0000	0.0000
	Λ =45 deg	
2154	1.0000	0.0000
2155	1.0000	0.0000
2156	1.0000	0.0000
2157	0.9998	0.0002
2158	0.9998	0.0003
2184	0.9840	0.0160
2185	0.9899	0.0101
2186	0.9984	0.0016
2187	0.9989	0.0011

Table B.7: Summary of the relevant parameters for the N_2 shots. θ denotes momentum thickness, δ_{99} does boundary layer thickness where local velocity reaches 99% of edge velocity both computed from BLIMPK code. R_θ for Reynolds number based on θ, $f_{2\mathrm{nd}}$ for the estimated most strongry amplified 2nd mode frequency. "L", "Tr" and "T" in "BL" column denote the boundary layer states, which are "Laminar", "Transitional" and "Turbulent" respectively.

Shot	$\bar{R}^*$	h_0 MJ/kg	η^* mm	U_e km/s	M_e	θ mm	δ_{99} mm	R_θ	$f_{2\mathrm{nd}}$ MHz	BL
				$\Lambda = 60$ deg						
2066	1085	8.65	0.067	3.30	3.39	0.032	0.21	526	7.99	T
2067	941	8.61	0.077	3.29	3.39	0.037	0.24	457	6.91	Tr
2068	740	8.74	0.098	3.32	3.40	0.048	0.30	358	5.47	Tr
2069	628	8.57	0.116	3.28	3.40	0.056	0.36	303	4.60	L
2070	728	8.96	0.100	3.36	3.40	0.048	0.31	354	5.44	L
2071	931	8.84	0.078	3.33	3.39	0.038	0.24	453	6.92	L
2072	1083	8.51	0.067	3.27	3.39	0.032	0.21	524	7.91	Tr
2073	833	11.95	0.086	3.86	3.36	0.043	0.26	411	7.33	Tr
2074	838	12.89	0.086	4.00	3.34	0.043	0.26	424	7.63	Tr
2075	819	13.15	0.087	4.03	3.34	0.045	0.27	422	7.48	T
2076	537	12.60	0.132	3.94	3.31	0.067	0.41	272	4.82	L
2077	801	13.84	0.089	4.13	3.32	0.046	0.28	412	7.48	T
2078	688	13.26	0.104	4.04	3.32	0.053	0.32	349	6.31	Tr
2079	630	14.51	0.112	4.20	3.28	0.059	0.35	330	6.02	L
2080	939	8.82	0.077	3.33	3.39	0.038	0.24	456	6.97	L
2081	671	13.84	0.106	4.12	3.30	0.055	0.33	348	6.29	Tr
2082	766	13.94	0.093	4.14	3.31	0.048	0.29	399	7.19	Tr
2083	574	3.76	0.126	2.15	3.35	0.053	0.37	240	2.90	L
2084	924	3.22	0.078	1.98	3.33	0.031	0.23	372	4.36	T
2085	758	2.49	0.095	1.72	3.30	0.035	0.27	281	3.20	T
2086	765	2.34	0.094	1.66	3.30	0.034	0.26	277	3.14	T
2087	655	2.74	0.110	1.82	3.31	0.042	0.32	252	2.88	T
2088	936	8.61	0.077	3.29	3.39	0.038	0.24	454	6.87	L
2089	785	6.89	0.092	2.94	3.39	0.043	0.28	369	5.19	T
2091	661	7.01	0.110	2.97	3.40	0.052	0.34	311	4.41	Tr
2092	480	5.85	0.151	2.71	3.38	0.069	0.46	220	2.95	L
2093	699	9.59	0.104	3.47	3.39	0.050	0.31	337	5.55	L
2094	842	11.93	0.086	3.86	3.36	0.042	0.26	413	7.45	T
2095	880	10.65	0.082	3.65	3.39	0.041	0.26	437	7.16	T
2096	989	8.72	0.073	3.31	3.39	0.036	0.23	480	7.31	T
2097	844	7.97	0.086	3.17	3.39	0.041	0.26	405	5.98	Tr
2098	761	7.97	0.095	3.17	3.40	0.046	0.29	364	5.39	Tr
2099	582	10.40	0.124	3.61	3.37	0.064	0.38	299	4.71	L
2100	688	11.01	0.105	3.71	3.37	0.000	0.00			L

continued on next page

continued from previous page (Table B.7)

Shot	$\bar{R}^*$	h_0 MJ/kg	η^* mm	U_e km/s	M_e	θ mm	δ_{99} mm	R_θ	$f_{2\mathrm{nd}}$ MHz	BL
2101	734	11.72	0.098	3.82	3.36	0.049	0.30	364	6.36	L
2102	772	10.27	0.094	3.59	3.39	0.047	0.29	384	6.28	L
2103	809	9.24	0.089	3.40	3.38	0.000	0.00			L
2104	676	7.11	0.107	2.99	3.39	0.051	0.33	319	4.54	Tr
2105	621	20.96	0.114	4.88	3.23	0.000	0.00			L
2106	625	18.98	0.112	4.69	3.23	0.000	0.00			L
2107	709	15.28	0.100	4.30	3.28	0.053	0.31	376	6.95	L
2108	831	5.51	0.087	2.63	3.38	0.039	0.26	377	4.97	L
2109	665	4.78	0.109	2.44	3.37	0.048	0.33	293	3.73	Tr
2110	807	5.53	0.090	2.63	3.38	0.041	0.27	366	4.84	Tr
2133	1014	6.18	0.071	2.79	3.39	0.000	0.00			Tr
2134	942	5.39	0.077	2.60	3.38	0.000	0.00			L
	$\Lambda = 45$ deg									
2154	537	3.64	0.085	1.80	2.17	0.051	0.29	326	3.09	L
2155	681	3.79	0.067	1.83	2.17	0.041	0.23	416	3.99	Tr
2156	825	4.31	0.055	1.95	2.18	0.034	0.19	512	5.11	T
2157	809	8.41	0.057	2.69	2.21	0.038	0.20	536	6.77	T
2158	638	7.81	0.072	2.60	2.22	0.047	0.25	418	5.19	L
2184	701	16.79	0.070	3.66	2.31	0.043	0.22	435	8.30	L
2185	747	15.96	0.065	3.59	2.30	0.041	0.21	467	8.63	T
2186	723	11.56	0.065	3.13	2.24	0.043	0.22	477	7.10	Tr
2187	589	9.72	0.079	2.88	2.22	0.052	0.27	392	5.30	L

Table B.8: Summary of reference conditions and mole fractions at the wall for the N_2 shots. Wall temperature was assumed constant at 300 K.

Shot	p^* Pa	T^* K	ρ^* kg/m^3	μ^* kg/sm	h_w MJ/kg	$x_{N_2,w}$
	$\Lambda = 60$ deg					
2066	247.2	2344.74	0.3552	7.21×10^{-5}	0.34	1.000
2067	185.3	2336.39	0.2672	7.19×10^{-5}	0.34	1.000
2068	115.6	2363.98	0.1647	7.25×10^{-5}	0.34	1.000
2069	81.7	2325.11	0.1184	7.17×10^{-5}	0.34	1.000
2070	114.6	2413.68	0.1600	7.36×10^{-5}	0.34	1.000
2071	186.1	2390.53	0.2623	7.31×10^{-5}	0.34	1.000
2072	242.0	2311.73	0.3528	7.14×10^{-5}	0.34	1.000
2073	205.4	3112.90	0.2223	8.90×10^{-5}	0.34	1.000
2074	226.8	3333.83	0.2292	9.37×10^{-5}	0.34	1.000
2075	222.5	3396.32	0.2208	9.50×10^{-5}	0.34	1.000
2076	92.8	3280.92	0.0953	9.25×10^{-5}	0.34	1.000
2077	226.8	3560.52	0.2146	9.84×10^{-5}	0.34	1.000
2078	160.0	3428.91	0.1572	9.57×10^{-5}	0.34	1.000
2079	151.2	3732.16	0.1365	1.02×10^{-4}	0.34	0.999
2080	188.8	2384.17	0.2668	7.30×10^{-5}	0.34	1.000
2081	160.9	3568.75	0.1519	9.86×10^{-5}	0.34	1.000
2082	210.2	3588.41	0.1973	9.90×10^{-5}	0.34	1.000
2083	33.3	1190.52	0.0941	4.44×10^{-5}	0.34	1.000
2084	77.0	1057.84	0.2451	4.09×10^{-5}	0.34	1.000
2085	43.4	875.36	0.1670	3.59×10^{-5}	0.34	1.000
2086	42.5	837.23	0.1709	3.48×10^{-5}	0.34	1.000
2087	34.6	939.16	0.1240	3.77×10^{-5}	0.34	1.000
2088	183.3	2335.84	0.2645	7.19×10^{-5}	0.34	1.000
2089	103.9	1936.30	0.1808	6.27×10^{-5}	0.34	1.000
2091	74.7	1963.38	0.1282	6.33×10^{-5}	0.34	1.000
2092	33.5	1692.06	0.0668	5.69×10^{-5}	0.34	1.000
2093	113.4	2561.06	0.1492	7.69×10^{-5}	0.34	1.000
2094	209.0	3106.68	0.2266	8.88×10^{-5}	0.34	1.000
2095	200.5	2805.99	0.2408	8.23×10^{-5}	0.34	1.000
2096	207.3	2361.29	0.2958	7.25×10^{-5}	0.34	1.000
2097	138.2	2188.65	0.2127	6.86×10^{-5}	0.34	1.000
2098	111.7	2185.71	0.1722	6.85×10^{-5}	0.34	1.000
2099	86.3	2753.65	0.1056	8.12×10^{-5}	0.34	1.000
2100	127.8	2893.79	0.1488	8.42×10^{-5}	0.34	1.000
2101	156.2	3059.63	0.1720	8.78×10^{-5}	0.34	1.000
2102	148.8	2717.41	0.1845	8.04×10^{-5}	0.34	1.000
2103	147.3	2483.78	0.1998	7.52×10^{-5}	0.34	1.000
2104	79.4	1986.59	0.1346	6.39×10^{-5}	0.34	1.000
2105	220.8	5064.61	0.1450	1.29×10^{-4}	0.34	1.000
2106	204.7	4725.90	0.1451	1.22×10^{-4}	0.34	1.000

continued on next page

continued from previous page (Table B.8)						
Shot	p^*	T^*	ρ^*	μ^*	h_w	$x_{\mathrm{N}_2,w}$
	Pa	K	kg/m^3	kg/sm	MJ/kg	
2107	202.9	3910.61	0.1747	1.06×10^{-4}	0.34	1.000
2108	95.5	1611.88	0.1997	5.50×10^{-5}	0.34	1.000
2109	54.2	1436.94	0.1270	5.07×10^{-5}	0.34	1.000
2110	90.4	1616.08	0.1884	5.51×10^{-5}	0.34	1.000
2133	157.2	1770.70	0.2990	5.88×10^{-5}	0.34	1.000
2134	120.3	1583.32	0.2561	5.43×10^{-5}	0.34	1.000
	$\Lambda = 45$ deg					
2154	68.6	1318.46	0.1753	4.96×10^{-5}	0.34	1.000
2155	114.2	1363.37	0.2822	5.07×10^{-5}	0.34	1.000
2156	186.7	1514.70	0.4154	5.43×10^{-5}	0.34	1.000
2157	331.7	2691.06	0.4154	7.88×10^{-5}	0.34	1.000
2158	191.4	2519.73	0.2560	7.55×10^{-5}	0.34	1.000
2184	469.7	4918.25	0.3198	1.17×10^{-4}	0.34	1.000
2185	513.5	4735.88	0.3640	1.14×10^{-4}	0.34	1.000
2186	359.2	3576.09	0.3384	9.48×10^{-5}	0.34	1.000
2187	201.8	3059.22	0.2222	8.57×10^{-5}	0.34	1.000

B.3 CO_2 shots

Table B.9: Stagnation and freestream conditions for carbon dioxide shots. From measured stagnation pressure P_0 and shock velocity in the shock tube V_{shock}, stagnation conditions are calculated (such as T_0 and its composition). Freestream conditions were computed with NENZF non-equilibrium nozzle code, where vibrational equilibrium was assumed. M_∞ denotes frozen freestream Mach number.

shot	P_0 MPa	V_{shock} km/s	T_0 K	T_∞ K	p_∞ kPa	ρ_∞ kg/m^3	u_∞ km/s	M_∞	μ_∞ kg/m s
					$\Lambda = 60$ deg				
2028	11.40	1.21	1547	453	5.62	6.57×10^{-2}	1.63	5.00	2.20×10^{-5}
2029	12.46	1.35	1755	387	1.13	1.55×10^{-2}	1.83	6.03	1.92×10^{-5}
2031	5.84	2.21	2967	1121	3.48	1.59×10^{-2}	2.40	4.70	4.47×10^{-5}
2032	4.43	1.79	2435	639	0.50	4.07×10^{-3}	2.18	5.66	2.94×10^{-5}
2033	13.26	1.80	2649	710	1.53	1.12×10^{-2}	2.30	5.68	3.19×10^{-5}
2034	18.14	1.50	2134	526	1.95	1.95×10^{-2}	2.03	5.80	2.50×10^{-5}
2035	20.50	1.34	1753	393	2.02	2.72×10^{-2}	1.82	5.97	1.94×10^{-5}
2036	15.39	1.69	2326	589	1.69	1.51×10^{-2}	2.13	5.76	2.75×10^{-5}
2037	43.44	1.84	2568	679	4.27	3.31×10^{-2}	2.25	5.69	3.08×10^{-5}
2038	43.82	1.82	2611	696	4.60	3.47×10^{-2}	2.28	5.71	3.14×10^{-5}
2039	37.26	1.73	2396	606	3.85	3.34×10^{-2}	2.16	5.78	2.81×10^{-5}
2040	48.63	1.90	2719	744	5.28	3.72×10^{-2}	2.34	5.68	3.30×10^{-5}
2041	14.42	1.79	2655	930	7.42	4.17×10^{-2}	2.21	4.80	3.90×10^{-5}
2042	39.85	1.79	2547	890	22.37	1.32×10^{-1}	2.14	4.77	3.77×10^{-5}
2043	40.24	2.49	3573	1574	25.80	8.38×10^{-2}	2.74	4.56	5.64×10^{-5}
2044	14.60	1.75	2606	917	8.48	4.84×10^{-2}	2.17	4.76	3.86×10^{-5}
2045	40.28	2.50	3585	1584	25.86	8.35×10^{-2}	2.75	4.55	5.66×10^{-5}
2046	29.79	2.50	3532	1538	18.34	6.07×10^{-2}	2.73	4.58	5.55×10^{-5}
2047	23.03	2.54	3534	1542	14.40	4.72×10^{-2}	2.74	4.57	5.57×10^{-5}
2048	12.92	2.26	3066	1197	7.70	3.31×10^{-2}	2.45	4.69	4.68×10^{-5}
2049	29.65	2.49	3542	1552	18.90	6.20×10^{-2}	2.73	4.57	5.59×10^{-5}
2050	49.09	2.99	4209	2053	33.13	7.86×10^{-2}	3.12	4.43	6.75×10^{-5}
2051	55.54	3.08	4345	2135	36.95	8.35×10^{-2}	3.20	4.42	6.93×10^{-5}
2052	58.87	2.73	3965	1883	38.78	1.04×10^{-1}	2.96	4.47	6.35×10^{-5}
2054	11.06	1.49	2159	714	6.04	4.46×10^{-2}	1.95	4.82	3.20×10^{-5}
2055	4.66	1.58	2076	679	2.49	1.94×10^{-2}	1.91	4.84	3.07×10^{-5}
2056	4.67	1.32	1536	448	2.30	2.72×10^{-2}	1.62	5.00	2.18×10^{-5}
2058	10.51	1.47	1908	605	5.45	4.76×10^{-2}	1.82	4.89	2.81×10^{-5}
2059	31.58	2.55	3629	1624	20.71	6.46×10^{-2}	2.78	4.54	5.76×10^{-5}
2060	7.96	1.41	1783	551	4.01	3.84×10^{-2}	1.76	4.93	2.60×10^{-5}
2061	5.79	1.43	1743	538	3.00	2.95×10^{-2}	1.74	4.92	2.55×10^{-5}
2062	9.66	1.51	2058	670	5.14	4.05×10^{-2}	1.90	4.85	3.04×10^{-5}
2063	8.93	1.67	2364	796	4.86	3.21×10^{-2}	2.05	4.81	3.47×10^{-5}

continued on next page

continued from previous page (Table B.9)

shot	P_0 MPa	V_{shock} km/s	T_0 K	T_∞ K	p_∞ kPa	ρ_∞ kg/m^3	u_∞ km/s	M_∞	μ_∞ kg/m s
2064	47.76	1.85	2612	922	26.72	1.52×10^{-1}	2.17	4.76	3.87×10^{-5}
2065	54.20	3.13	4429	2182	36.59	8.00×10^{-2}	3.25	4.42	7.04×10^{-5}
2111	9.54	1.47	2000	645	5.02	4.11×10^{-2}	1.87	4.87	2.95×10^{-5}
2112	40.42	2.55	3756	1727	26.95	7.89×10^{-2}	2.85	4.50	6.00×10^{-5}
2113	29.22	2.15	3135	1246	17.68	7.37×10^{-2}	2.48	4.66	4.80×10^{-5}
2114	13.01	2.17	3016	1162	7.64	3.39×10^{-2}	2.42	4.70	4.58×10^{-5}
2115	25.45	2.11	3090	1214	15.17	6.49×10^{-2}	2.45	4.68	4.72×10^{-5}
2116	11.67	2.05	2883	1072	6.72	3.25×10^{-2}	2.34	4.73	4.33×10^{-5}
2117	17.78	2.11	3011	1159	10.54	4.72×10^{-2}	2.41	4.69	4.57×10^{-5}
2118	9.29	1.49	2009	649	4.94	4.02×10^{-2}	1.87	4.86	2.97×10^{-5}
2119	55.15	2.97	4234	2074	37.35	8.80×10^{-2}	3.13	4.42	6.79×10^{-5}
2120	69.86	3.28	4761	2357	46.95	9.25×10^{-2}	3.43	4.40	7.42×10^{-5}
2121	30.30	1.97	2901	1091	17.79	8.53×10^{-2}	2.34	4.71	4.37×10^{-5}
2122	72.18	3.57	5161	2503	45.14	7.93×10^{-2}	3.67	4.43	7.76×10^{-5}
2123	55.66	3.41	4865	2368	36.71	7.00×10^{-2}	3.51	4.43	7.47×10^{-5}
2124	31.61	2.48	3552	1559	20.12	6.57×10^{-2}	2.74	4.56	5.60×10^{-5}
2125	26.32	2.58	3612	1603	16.70	5.26×10^{-2}	2.79	4.56	5.71×10^{-5}
2126	51.86	3.06	4350	2138	35.03	7.88×10^{-2}	3.21	4.42	6.94×10^{-5}
2127	39.26	3.00	4222	2046	26.16	6.15×10^{-2}	3.15	4.44	6.74×10^{-5}
2128	23.84	1.94	2911	1096	13.95	6.64×10^{-2}	2.35	4.71	4.39×10^{-5}
2130	16.89	1.87	2734	988	9.65	5.11×10^{-2}	2.24	4.74	4.07×10^{-5}
2131	27.26	1.71	2563	896	15.03	8.81×10^{-2}	2.15	4.77	3.79×10^{-5}
2132	10.28	1.54	2121	693	5.65	4.31×10^{-2}	1.93	4.86	3.12×10^{-5}
2214	72.15	3.45	4997	2449	47.90	8.83×10^{-2}	3.56	4.41	7.63×10^{-5}
2215	42.44	3.47	4820	2314	27.75	5.34×10^{-2}	3.51	4.45	7.36×10^{-5}
2216	59.11	4.05	5892	2652	36.18	5.40×10^{-2}	4.09	4.50	8.16×10^{-5}
2217	50.61	4.00	5800	2597	30.85	4.69×10^{-2}	4.06	4.50	8.05×10^{-5}
			$\Lambda = 45$ deg						
2175	24.57	2.45	3420	1484	16.88	5.81×10^{-2}	2.64	4.52	5.42×10^{-5}
2176	33.86	2.56	3722	1732	25.59	7.45×10^{-2}	2.82	4.44	6.01×10^{-5}
2177	6.87	2.26	3083	1219	4.58	1.91×10^{-2}	2.47	4.63	4.74×10^{-5}
2178	18.26	2.36	3373	1451	13.16	4.62×10^{-2}	2.63	4.54	5.34×10^{-5}
2179	16.47	1.68	2344	810	10.44	6.78×10^{-2}	2.03	4.73	3.52×10^{-5}
2180	10.08	1.59	2218	754	6.25	4.37×10^{-2}	1.97	4.75	3.33×10^{-5}
2181	3.80	1.56	2060	686	2.32	1.79×10^{-2}	1.89	4.78	3.10×10^{-5}
2188	60.92	3.39	4890	2433	46.77	8.69×10^{-2}	3.49	4.35	7.60×10^{-5}
2189	20.58	3.33	4432	2106	15.26	3.25×10^{-2}	3.32	4.42	6.92×10^{-5}
2190	13.58	3.26	4289	1988	9.86	2.21×10^{-2}	3.26	4.45	6.67×10^{-5}
2191	33.00	4.11	5861	2534	22.10	3.30×10^{-2}	4.12	4.50	7.98×10^{-5}
2192	48.73	4.05	5855	2647	33.97	5.02×10^{-2}	4.07	4.44	8.17×10^{-5}
2193	28.92	3.73	5112	2355	19.68	3.44×10^{-2}	3.73	4.45	7.52×10^{-5}
2194	22.67	3.14	4272	2059	17.22	3.87×10^{-2}	3.21	4.40	6.79×10^{-5}
2195	47.09	3.51	4981	2425	35.36	6.39×10^{-2}	3.58	4.38	7.61×10^{-5}

continued on next page

continued from previous page (Table B.9)

shot	P_0 MPa	V_{shock} km/s	T_0 K	T_∞ K	p_∞ kPa	ρ_∞ kg/m^3	u_∞ km/s	M_∞	μ_∞ kg/m s
2196	21.20	3.28	4387	2096	15.96	3.44×10^{-2}	3.29	4.41	6.89×10^{-5}
2197	33.82	3.35	4590	2240	25.67	5.19×10^{-2}	3.37	4.38	7.20×10^{-5}
2198	43.51	4.11	5894	2624	30.09	4.42×10^{-2}	4.10	4.46	8.14×10^{-5}

Table B.10: Freestream mole fraction for CO_2 shots computed with NENZF code.

shot	x_{CO_2}	x_{CO}	x_{O_2}	x_O	x_C
	Λ =60 deg				
2028	0.9998	0.0001	0.0001	0.0000	
2029	0.9991	0.0006	0.0003	0.0000	
2031	0.8950	0.0700	0.0350	0.0000	
2032	0.9604	0.0264	0.0132	0.0000	
2033	0.9563	0.0292	0.0146	0.0000	
2034	0.9922	0.0052	0.0026	0.0000	
2035	0.9992	0.0005	0.0003	0.0000	
2036	0.9808	0.0128	0.0064	0.0000	
2037	0.9795	0.0137	0.0068	0.0000	
2038	0.9778	0.0148	0.0074	0.0000	
2039	0.9811	0.0126	0.0063	0.0000	
2040	0.9752	0.0165	0.0083	0.0000	
2041	0.9633	0.0245	0.0123	0.0000	
2042	0.9825	0.0116	0.0058	0.0000	
2043	0.8995	0.0671	0.0335	0.0000	
2044	0.9667	0.0222	0.0111	0.0000	
2045	0.8974	0.0684	0.0342	0.0000	
2046	0.8857	0.0764	0.0379	0.0000	
2047	0.8661	0.0894	0.0445	0.0000	
2048	0.9200	0.0533	0.0267	0.0000	
2049	0.8843	0.0771	0.0386	0.0000	
2050	0.7655	0.1553	0.0761	0.0031	0.0000
2051	0.7405	0.1714	0.0832	0.0050	0.0000
2052	0.8506	0.0995	0.0496	0.0003	0.0000
2054	0.9901	0.0066	0.0033	0.0000	
2055	0.9908	0.0061	0.0031	0.0000	
2056	0.9998	0.0001	0.0001	0.0000	
2058	0.9973	0.0018	0.0009	0.0000	
2059	0.8712	0.0858	0.0429	0.0000	0.0000
2060	0.9987	0.0009	0.0004	0.0000	
2061	0.9989	0.0007	0.0004	0.0000	
2062	0.9932	0.0046	0.0023	0.0000	
2063	0.9761	0.0159	0.0080	0.0000	
2064	0.9826	0.0116	0.0058	0.0000	
2065	0.7110	0.1903	0.0916	0.0071	0.0000
2111	0.9952	0.0032	0.0016	0.0000	
2112	0.8637	0.0908	0.0454	0.0000	0.0000
2113	0.9444	0.0370	0.0185	0.0000	0.0000
2114	0.9276	0.0483	0.0241	0.0000	0.0000
2115	0.9443	0.0371	0.0186	0.0000	
2116	0.9381	0.0413	0.0206	0.0000	

continued on next page

continued from previous page (Table B.10)					
shot	x_{CO_2}	x_{CO}	x_{O_2}	x_O	x_C
2117	0.9386	0.0410	0.0205	0.0000	
2118	0.9949	0.0034	0.0017	0.0000	
2119	0.7727	0.1505	0.0738	0.0030	0.0000
2120	0.6449	0.2321	0.1091	0.0138	0.0000
2121	0.9646	0.0236	0.0118	0.0000	
2122	0.5219	0.3085	0.1388	0.0308	0.0000
2123	0.5793	0.2733	0.1259	0.0215	0.0000
2124	0.8869	0.0754	0.0377	0.0000	0.0000
2125	0.8601	0.0932	0.0466	0.0000	0.0000
2126	0.7294	0.1785	0.0865	0.0056	0.0000
2127	0.7322	0.1770	0.0862	0.0046	0.0000
2128	0.9585	0.0277	0.0139	0.0000	
2130	0.9617	0.0255	0.0128	0.0000	
2131	0.9778	0.0148	0.0074	0.0000	
2132	0.9912	0.0059	0.0029	0.0000	
2214	0.5805	0.2724	0.1253	0.0217	0.0000
2215	0.5502	0.2915	0.1331	0.0253	0.0000
2216	0.3279	0.4206	0.1691	0.0824	0.0000
2217	0.3243	0.4225	0.1692	0.0841	0.0000
	Λ =45 deg				
2175	0.8927	0.0719	0.0354	0.0000	
2176	0.8560	0.0960	0.0480	0.0001	0.0000
2177	0.8803	0.0798	0.0399	0.0000	
2178	0.8847	0.0769	0.0385	0.0000	
2179	0.9831	0.0113	0.0056	0.0000	
2180	0.9869	0.0088	0.0044	0.0000	
2181	0.9909	0.0061	0.0030	0.0000	
2188	0.5826	0.2711	0.1249	0.0213	0.0000
2189	0.5610	0.2855	0.1321	0.0214	0.0000
2190	0.5467	0.2950	0.1366	0.0217	0.0000
2191	0.2591	0.4556	0.1703	0.1150	0.0000
2192	0.3066	0.4319	0.1704	0.0911	0.0000
2193	0.3931	0.3846	0.1623	0.0599	0.0000
2194	0.6334	0.2404	0.1142	0.0120	0.0000
2195	0.5159	0.3122	0.1403	0.0315	0.0000
2196	0.5817	0.2727	0.1272	0.0184	0.0000
2197	0.5856	0.2697	0.1251	0.0196	0.0000
2198	0.2862	0.4424	0.1709	0.1006	0.0000

Table B.11: Summary of the relevant parameters for the CO_2 shots. θ denotes momentum thickness, δ_{99} does boundary layer thickness where local velocity reaches 99% of edge velocity both computed from BLIMPK code. R_θ for Reynolds number based on θ, $f_{2\mathrm{nd}}$ for the estimated most strongry amplified 2nd mode frequency. "L", "Tr" and "T" in "BL" column denote the boundary layer states, which are "Laminar", "Transitional" and "Turbulent" respectively.

Shot	$\bar{R}^*$	h_0 MJ/kg	η^* mm	U_e km/s	M_e	θ mm	δ_{99} mm	R_θ	$f_{2\mathrm{nd}}$ MHz	BL
					$\Lambda = 60$ deg					
2028	998	1.66	0.07	1.41	3.40	0.031	0.23	439	3.05	T
2029	558	1.94	0.14	1.58	3.76	0.058	0.44	238	1.78	T
2031	443	4.48	0.15	2.08	3.17	0.082	0.49	244	2.14	L
2032	267	3.07	0.27	1.89	3.56	0.128	0.86	126	1.10	L
2033	451	3.45	0.16	1.99	3.59	0.080	0.52	224	1.90	L
2034	623	2.49	0.12	1.76	3.71	0.054	0.39	278	2.27	L
2035	735	1.94	0.10	1.58	3.75	0.044	0.33	313	2.36	L
2036	538	2.81	0.14	1.84	3.66	0.063	0.44	247	2.09	L
2037	802	3.18	0.09	1.95	3.67	0.044	0.30	378	3.29	L
2038	825	3.29	0.09	1.98	3.68	0.043	0.29	393	3.43	L
2039	806	2.90	0.09	1.87	3.68	0.043	0.30	372	3.16	L
2040	854	3.50	0.09	2.03	3.67	0.043	0.28	419	3.60	Tr
2041	775	3.46	0.09	1.91	3.29	0.046	0.28	402	3.36	T
2042	1407	3.17	0.05	1.85	3.33	0.025	0.16	716	5.81	T
2043	1050	5.97	0.07	2.37	3.27	0.036	0.21	581	5.66	T
2044	832	3.35	0.08	1.88	3.28	0.043	0.27	437	3.49	Tr
2045	1046	6.01	0.07	2.38	3.27	0.036	0.21	576	5.69	T
2046	887	5.95	0.08	2.36	3.26	0.041	0.24	474	4.95	Tr
2047	770	6.08	0.09	2.37	3.25	0.048	0.28	421	4.25	L
2048	664	4.60	0.10	2.13	3.23	0.056	0.33	365	3.21	L
2049	893	5.99	0.08	2.37	3.26	0.042	0.24	491	4.87	L
2050	995	8.45	0.07	2.71	3.29	0.037	0.22	534	6.27	L
2051	1033	8.94	0.07	2.77	3.30	0.036	0.21	554	6.64	Tr
2052	1153	7.28	0.06	2.57	3.29	0.033	0.19	625	6.85	Tr
2054	819	2.53	0.08	1.69	3.35	0.041	0.27	392	3.09	L
2055	540	2.42	0.13	1.65	3.35	0.061	0.41	255	2.00	L
2056	641	1.64	0.11	1.40	3.40	0.048	0.36	281	1.95	T
2058	857	2.16	0.08	1.58	3.39	0.038	0.27	398	2.97	Tr
2059	905	6.30	0.08	2.41	3.26	0.041	0.24	495	5.06	L
2060	771	1.98	0.09	1.52	3.40	0.042	0.30	351	2.57	T
2061	673	1.93	0.10	1.50	3.39	0.047	0.34	305	2.21	T
2062	785	2.38	0.09	1.64	3.36	0.042	0.29	371	2.86	Tr
2063	682	2.89	0.10	1.77	3.30	0.050	0.32	339	2.74	L
2064	1515	3.28	0.05	1.88	3.33	0.023	0.15	777	6.34	T

continued on next page

continued from previous page (Table B.11)

Shot	$\bar{R}^*$	h_0 MJ/kg	η^* mm	U_e km/s	M_e	θ mm	δ_{99} mm	R_θ	$f_{2\text{nd}}$ MHz	BL
2065	1010	9.33	0.07	2.81	3.29	0.037	0.21	542	6.60	L
2111	795	2.29	0.09	1.62	3.37	0.041	0.28	373	2.85	T
2112	1001	6.67	0.07	2.47	3.27	0.038	0.22	553	5.65	Tr
2113	1017	4.60	0.07	2.15	3.27	0.037	0.22	557	4.90	T
2114	676	4.43	0.10	2.10	3.23	0.054	0.33	370	3.23	L
2115	954	4.50	0.07	2.13	3.26	0.039	0.23	522	4.56	T
2116	664	4.06	0.10	2.03	3.24	0.054	0.33	358	3.06	Tr
2117	805	4.35	0.08	2.09	3.25	0.046	0.27	438	3.80	L
2118	785	2.31	0.09	1.62	3.37	0.042	0.29	371	2.81	T
2119	1054	8.46	0.07	2.71	3.29	0.035	0.20	566	6.65	T
2120	1102	10.55	0.06	2.97	3.30	0.034	0.20	591	7.50	T
2121	1112	3.96	0.06	2.02	3.29	0.033	0.20	592	5.04	T
2122	1055	12.26	0.07	3.18	3.31	0.042	0.24	664	6.55	Tr
2123	967	11.27	0.07	3.04	3.30	0.039	0.23	521	6.72	Tr
2124	922	6.00	0.07	2.37	3.27	0.041	0.24	507	5.03	Tr
2125	814	6.33	0.08	2.41	3.26	0.046	0.26	444	4.56	L
2126	999	9.02	0.07	2.78	3.29	0.037	0.22	536	6.45	Tr
2127	877	8.70	0.08	2.73	3.28	0.042	0.24	470	5.60	L
2128	975	4.02	0.07	2.03	3.28	0.037	0.23	520	4.45	Tr
2130	852	3.62	0.08	1.94	3.27	0.042	0.26	444	3.75	L
2131	1142	3.22	0.06	1.86	3.31	0.031	0.19	582	4.77	T
2132	810	2.48	0.09	1.67	3.36	0.042	0.28	393	2.96	L
2214	1101	11.54	0.06	3.08	3.31	0.034	0.20	590	7.78	T
2215	847	11.38	0.08	3.04	3.29	0.044	0.26	454	5.94	L
2216	925	15.63	0.08	3.54	3.29	0.043	0.25	521	7.22	Tr
2217	858	15.49	0.08	3.52	3.29	0.046	0.26	481	6.68	L
	$\Lambda = 45$ deg									
2175	811	5.61	0.06	1.87	2.42	0.035	0.19	471	5.00	T
2176	925	6.64	0.05	2.00	2.44	0.031	0.16	526	6.14	T
2177	453	4.84	0.11	1.74	2.38	0.062	0.33	265	2.62	L
2178	719	5.56	0.07	1.86	2.41	0.040	0.21	417	4.42	L
2179	941	2.84	0.05	1.43	2.37	0.032	0.18	600	4.00	T
2180	758	2.63	0.06	1.39	2.37	0.040	0.22	480	3.12	T
2181	485	2.39	0.10	1.34	2.37	0.062	0.35	304	1.91	L
2188	1070	11.27	0.05	2.47	2.43	0.028	0.15	624	8.44	T
2189	631	10.35	0.08	2.35	2.42	0.045	0.24	358	4.91	T
2190	514	10.09	0.10	2.31	2.41	0.055	0.29	289	3.96	L
2191	726	16.37	0.07	2.91	2.37	0.045	0.22	466	6.51	L
2192	927	15.77	0.05	2.88	2.38	0.038	0.18	639	8.11	Tr
2193	693	13.25	0.07	2.64	2.41	0.043	0.23	412	5.84	L
2194	680	9.46	0.07	2.27	2.43	0.041	0.22	382	5.14	L
2195	920	11.99	0.06	2.53	2.42	0.032	0.17	534	7.49	T
2196	647	10.09	0.08	2.32	2.42	0.044	0.23	365	5.02	L

continued on next page

continued from previous page (Table B.11)

Shot	$\bar{R}^*$	h_0 MJ/kg	η^* mm	U_e km/s	M_e	θ mm	δ_{99} mm	R_θ	$f_{2\mathrm{nd}}$ MHz	BL
2197	805	10.56	0.06	2.38	2.43	0.036	0.19	458	6.31	T
2198	873	16.09	0.06	2.90	2.38	0.040	0.19	598	7.68	L

Table B.12: Summary of reference conditions and mole fractions at the wall for the CO_2 shots. Wall temperature was assumed constant at 300 K.

Shot	p^* Pa	T^* K	ρ^* kg/m^3	μ^* kg/sm	h_w MJ/kg	$x_{CO_2,w}$	$x_{O_2,w}$	$x_{CO,w}$	$x_{O,w}$	$x_{C,w}$
				$\Lambda = 60$ deg						
2029	12.9	777	8.76×10^{-2}	3.41×10^{-5}	0.218	1.000	0.000	0.000	0.000	0.000
2031	23.2	1547	7.95×10^{-2}	5.55×10^{-5}	0.244	0.994	0.002	0.004	0.000	0.000
2032	4.8	1104	2.30×10^{-2}	4.40×10^{-5}	0.218	1.000	0.000	0.000	0.000	0.000
2033	14.9	1201	6.54×10^{-2}	4.67×10^{-5}	0.218	1.000	0.000	0.000	0.000	0.000
2034	20.2	933	1.14×10^{-1}	3.90×10^{-5}	0.218	1.000	0.000	0.000	0.000	0.000
2035	22.5	777	1.53×10^{-1}	3.41×10^{-5}	0.218	1.000	0.000	0.000	0.000	0.000
2036	17.1	1023	8.83×10^{-2}	4.17×10^{-5}	0.218	1.000	0.000	0.000	0.000	0.000
2037	41.8	1120	1.98×10^{-1}	4.45×10^{-5}	0.218	1.000	0.000	0.000	0.000	0.000
2038	45.4	1148	2.09×10^{-1}	4.52×10^{-5}	0.218	1.000	0.000	0.000	0.000	0.000
2039	39.0	1046	1.97×10^{-1}	4.24×10^{-5}	0.218	1.000	0.000	0.000	0.000	0.000
2040	51.3	1202	2.26×10^{-1}	4.67×10^{-5}	0.218	1.000	0.000	0.000	0.000	0.000
2041	52.0	1245	2.21×10^{-1}	4.79×10^{-5}	0.218	1.000	0.000	0.000	0.000	0.000
2042	155.3	1162	7.07×10^{-1}	4.56×10^{-5}	0.218	1.000	0.000	0.000	0.000	0.000
2043	163.7	1956	4.41×10^{-1}	6.49×10^{-5}	0.439	0.949	0.017	0.033	0.000	0.000
2044	58.6	1217	2.55×10^{-1}	4.71×10^{-5}	0.218	1.000	0.000	0.000	0.000	0.000
2045	163.9	1969	4.38×10^{-1}	6.51×10^{-5}	0.451	0.947	0.018	0.035	0.000	0.000
2046	117.5	1952	3.17×10^{-1}	6.48×10^{-5}	0.441	0.949	0.017	0.034	0.000	0.000
2047	92.0	1996	2.42×10^{-1}	6.57×10^{-5}	0.504	0.935	0.022	0.043	0.000	0.000
2048	51.2	1566	1.73×10^{-1}	5.60×10^{-5}	0.241	0.994	0.002	0.004	0.000	0.000
2049	120.4	1967	3.22×10^{-1}	6.51×10^{-5}	0.460	0.945	0.019	0.036	0.000	0.000
2050	202.4	2509	4.04×10^{-1}	7.67×10^{-5}	1.355	0.758	0.084	0.158	0.000	0.000
2051	225.9	2586	4.32×10^{-1}	7.83×10^{-5}	1.535	0.724	0.096	0.180	0.000	0.000
2052	239.1	2292	5.40×10^{-1}	7.21×10^{-5}	0.851	0.861	0.048	0.091	0.000	0.000
2054	43.2	984	2.33×10^{-1}	4.06×10^{-5}	0.218	1.000	0.000	0.000	0.000	0.000
2055	18.1	950	1.01×10^{-1}	3.96×10^{-5}	0.218	1.000	0.000	0.000	0.000	0.000
2056	18.1	719	1.33×10^{-1}	3.21×10^{-5}	0.218	1.000	0.000	0.000	0.000	0.000
2058	40.5	872	2.46×10^{-1}	3.71×10^{-5}	0.218	1.000	0.000	0.000	0.000	0.000
2059	130.5	2053	3.34×10^{-1}	6.70×10^{-5}	0.551	0.925	0.026	0.049	0.000	0.000
2060	30.4	820	1.96×10^{-1}	3.55×10^{-5}	0.218	1.000	0.000	0.000	0.000	0.000
2061	22.7	804	1.49×10^{-1}	3.50×10^{-5}	0.218	1.000	0.000	0.000	0.000	0.000
2062	37.3	938	2.11×10^{-1}	3.92×10^{-5}	0.218	1.000	0.000	0.000	0.000	0.000
2063	34.5	1089	1.67×10^{-1}	4.36×10^{-5}	0.218	1.000	0.000	0.000	0.000	0.000
2064	184.9	1193	8.21×10^{-1}	4.65×10^{-5}	0.218	1.000	0.000	0.000	0.000	0.000
2065	223.5	2642	4.14×10^{-1}	7.95×10^{-5}	1.707	0.692	0.108	0.201	0.000	0.000
2111	36.9	913	2.14×10^{-1}	3.84×10^{-5}	0.218	1.000	0.000	0.000	0.000	0.000
2112	167.9	2148	4.08×10^{-1}	6.90×10^{-5}	0.653	0.902	0.034	0.064	0.000	0.000
2113	116.6	1558	3.96×10^{-1}	5.58×10^{-5}	0.234	0.996	0.001	0.003	0.000	0.000
2114	51.1	1519	1.78×10^{-1}	5.48×10^{-5}	0.232	0.997	0.001	0.002	0.000	0.000
2115	100.8	1532	3.48×10^{-1}	5.51×10^{-5}	0.232	0.997	0.001	0.002	0.000	0.000
2116	45.5	1417	1.70×10^{-1}	5.23×10^{-5}	0.223	0.999	0.000	0.001	0.000	0.000

continued on next page

continued from previous page (Table B.12)

Shot	p^* Pa	T^* K	ρ^* kg/m^3	μ^* kg/sm	h_w MJ/kg	$x_{CO_2,w}$	$x_{O_2,w}$	$x_{CO,w}$	$x_{O,w}$	$x_{C,w}$
2117	70.4	1493	2.50×10^{-1}	5.42×10^{-5}	0.227	0.998	0.001	0.002	0.000	0.000
2118	36.3	917	2.09×10^{-1}	3.85×10^{-5}	0.218	1.000	0.000	0.000	0.000	0.000
2119	227.4	2516	4.53×10^{-1}	7.68×10^{-5}	1.351	0.759	0.084	0.157	0.000	0.000
2120	287.1	2805	4.84×10^{-1}	8.29×10^{-5}	2.160	0.610	0.137	0.253	0.000	0.000
2121	120.0	1380	4.60×10^{-1}	5.14×10^{-5}	0.220	1.000	0.000	0.000	0.000	0.000
2122	282.6	2968	4.28×10^{-1}	8.65×10^{-5}	2.574	0.541	0.162	0.297	0.000	0.000
2123	227.9	2858	3.68×10^{-1}	8.41×10^{-5}	2.390	0.571	0.151	0.278	0.000	0.000
2124	128.0	1968	3.42×10^{-1}	6.51×10^{-5}	0.458	0.945	0.019	0.036	0.000	0.000
2125	106.2	2059	2.70×10^{-1}	6.71×10^{-5}	0.569	0.921	0.027	0.052	0.000	0.000
2126	213.8	2598	4.06×10^{-1}	7.86×10^{-5}	1.590	0.713	0.100	0.187	0.000	0.000
2127	160.7	2537	3.15×10^{-1}	7.73×10^{-5}	1.479	0.735	0.092	0.173	0.000	0.000
2128	94.0	1397	3.56×10^{-1}	5.18×10^{-5}	0.220	0.999	0.000	0.000	0.000	0.000
2130	65.9	1292	2.70×10^{-1}	4.91×10^{-5}	0.218	1.000	0.000	0.000	0.000	0.000
2131	104.7	1178	4.70×10^{-1}	4.61×10^{-5}	0.218	1.000	0.000	0.000	0.000	0.000
2132	41.1	966	2.25×10^{-1}	4.00×10^{-5}	0.218	1.000	0.000	0.000	0.000	0.000
2214	295.7	2889	4.73×10^{-1}	8.47×10^{-5}	2.267	0.592	0.143	0.265	0.000	0.000
2215	173.6	2834	2.82×10^{-1}	8.37×10^{-5}	2.300	0.587	0.145	0.268	0.000	0.000
2216	237.0	3170	3.10×10^{-1}	9.11×10^{-5}	2.918	0.487	0.185	0.329	0.000	0.000
2217	202.8	3145	2.67×10^{-1}	9.06×10^{-5}	2.937	0.484	0.186	0.331	0.000	0.000
	$\Lambda = 45$ deg									
2175	204.7	2157	4.96×10^{-1}	6.92×10^{-5}	0.872	0.856	0.050	0.095	0.000	0.000
2176	301.3	2406	6.41×10^{-1}	7.45×10^{-5}	1.239	0.781	0.076	0.143	0.000	0.000
2177	58.0	1937	1.58×10^{-1}	6.45×10^{-5}	0.690	0.895	0.036	0.069	0.000	0.000
2178	160.6	2143	3.91×10^{-1}	6.89×10^{-5}	0.874	0.855	0.050	0.095	0.000	0.000
2179	138.6	1207	6.08×10^{-1}	4.69×10^{-5}	0.227	0.998	0.001	0.001	0.000	0.000
2180	84.1	1141	3.90×10^{-1}	4.51×10^{-5}	0.223	0.999	0.000	0.001	0.000	0.000
2181	31.7	1062	1.58×10^{-1}	4.29×10^{-5}	0.220	1.000	0.000	0.000	0.000	0.000
2188	539.8	3040	8.03×10^{-1}	8.78×10^{-5}	2.483	0.562	0.165	0.273	0.000	0.000
2189	181.4	2879	2.86×10^{-1}	8.47×10^{-5}	2.635	0.531	0.166	0.304	0.000	0.000
2190	118.9	2826	1.91×10^{-1}	8.37×10^{-5}	2.681	0.523	0.168	0.309	0.000	0.000
2191	282.7	3319	3.37×10^{-1}	9.44×10^{-5}	2.774	0.511	0.177	0.312	0.000	0.000
2192	421.0	3238	5.43×10^{-1}	9.22×10^{-5}	1.348	0.834	0.166	0.000	0.000	0.000
2193	242.1	3133	3.25×10^{-1}	9.02×10^{-5}	3.009	0.472	0.189	0.338	0.000	0.000
2194	201.9	2800	3.37×10^{-1}	8.29×10^{-5}	2.367	0.575	0.149	0.276	0.000	0.000
2195	415.6	3096	5.89×10^{-1}	8.91×10^{-5}	2.884	0.492	0.181	0.327	0.000	0.000
2196	188.6	2858	3.02×10^{-1}	8.42×10^{-5}	2.560	0.543	0.161	0.296	0.000	0.000
2197	299.8	2943	4.63×10^{-1}	8.59×10^{-5}	2.644	0.529	0.166	0.305	0.000	0.000
2198	376.5	3248	4.79×10^{-1}	9.25×10^{-5}	1.411	0.825	0.175	0.000	0.000	0.000

Appendix C Numerical Codes Used in Data Analysis

C.1 STANJAN: Chemical Equilibrium Code

STANJAN is an interactive program for chemical equilibrium computations developed by Reynolds[55], where a detailed description was made. It uses 'element potential method' to find the minimized state in Gibbs energy. As described in some text books including that by Anderson[94] and by Vincenti[31], chemical equilibrium state is determined as Gibbs energy would not change by any infinitesimal change in advancement of chemical reactions, which is equivalent to no irreversible contribution to the change in entropy. This can be explicitly expressed in terms of chemical potential $\hat{\mu}_s$:

$$0 = \sum_s \hat{\mu}_s d\mathcal{N}_s = \sum_s \nu_s \hat{\mu}_s,$$

where $\mathcal{N}_s$ is number of moles of the chemical species and ν_s denotes stoichiometric coefficient of the chemical reaction in consideration. Here, Gibbs free energy is defined by:

$$G \equiv E + pV - TS = H - TS$$

It means if H and S is provided as functions of T for each chemical species, the chemical potential $\hat{\mu}_s$ can be calculated and so can be the chemical composition in equilibrium, since chemical potential $\hat{\mu}_s$ can be written as,

$$\hat{\mu}_s = \hat{\mu}_s^0(T) + \hat{R}T \ln \frac{p_i}{p_0},$$

where $\hat{\mu}_s^0$ is chemical potential that would be if the partial pressure were at the reference value p_0 and at the temperature of T. JANAF table (Chase *et al.*[56]) provides enthalpy h and entropy s at a reference pressure of 0.1 MPa as a function of temperature ranging from 0 K to 6000 K for more that a thousand of chemical species. STAN-JAN program[55] has been developed to calculate chemical compositions in equilibrium based on the JANAF table with the method outlined above.

C.2 NENZF: Quasi-1-Dimensional Non-equilibrium Nozzle Flow Code

The complete description of NENZF code can be found in the report by Lordi *et al.*[57]. Only basic concept of the code will be described here. Nozzle explanation flow in general is governed by the following quasi-1-dimensional equations:

$$\rho u A = \text{constant}, \tag{C.1}$$

$$u du + \frac{1}{\rho} dp = 0, \tag{C.2}$$

$$h + \frac{1}{2} u^2 = h_0 = \text{constant}, \tag{C.3}$$

where A is area of the nozzle. Consider a multi-component mixture composed of s chemical species which consist of c chemical elements and these species undergo r coupled chemical reactions of the form :

$$\sum_{j=1}^{s} \nu'_{ij} M_j \leftrightarrows \sum_{j=1}^{s} \nu''_{ij} M_j \qquad (i = 1, 2, \ldots, r),$$

where ν'_{ij} and ν''_{ij} are the stoichiometric coefficients of the reactants and products, respectively. Since these reactions are elementary reactions which can physically occur, r is not necessarily equal to $s - c$. The condition that the chemical elements be conserved is,

$$\sum_{j=1}^{s} \alpha_{jk} \frac{dN_j}{dx} = 0, \qquad (k = 1, 2, \ldots, c), \tag{C.4}$$

where α_{jk} denotes the number of atoms of the jth element per molecule of the ith species and N_j represents mole mass ratio of the jth species. In addition, chemical rate conditions give $s - c$ equations:

$$\frac{dN_j}{dx} = \sum_{i=1}^{n} (\nu''_{ij} - \nu'_{ij}) \frac{\rho^{\sum_j \nu'_{ij} - 1}}{u} k_{f_i} \prod_{j=1}^{s} N_j^{\nu'_{ij}} \left(1 - \frac{\rho^{\sum_j (\nu''_{ij} - \nu'_{ij})}}{K_i} \prod_{j=1}^{s} N_j^{\nu''_{ij} - \nu'_{ij}} \right), \qquad (j = c{+}1, c{+}2, \ldots, s), \tag{C.5}$$

where k_{f_j} is forward reaction rate and K_j is equilibrium constant of jth reaction. Equations C.1, C.2, C.3 can be re-written as,

$$\frac{d\ln\rho}{dx} + \frac{1}{u}\frac{du}{dx} + \frac{d\ln A}{dx} = 0,$$

$$\sum_{j=1}^{s}(T - h_j)\frac{dN_j}{dx} + \sum_{j=1}^{s} N_j(1 - C_{p_j})\frac{dT}{dx} + \frac{T}{\overline{M_w}}\frac{d\ln\rho}{dx} = 0, \tag{C.6}$$

$$\sum_{j=1}^{s} h_j\frac{dN_j}{dx} + \sum_{j=1}^{s} N_j C_{p_j}\frac{dT}{dx} - \frac{u^2}{\overline{M_w}}\frac{d\ln\rho}{dx} - \frac{u^2}{\overline{M_w}}\frac{d\ln A}{dx} = 0, \tag{C.7}$$

where C_{p_j} is specific heat at constant pressure of jth species defined as $\frac{dh_j}{dT}$ and h_j is enthalpy of the species related with enthalpy of the gas mixtures h as $h = \sum_j x_j h_j$. For a prescribed geometry (*i.e.*, $\frac{d\ln A}{dx}$ given), equations C.4, C.5, C.6, C.7 provide a set of $s + 2$ equations for the unknown gradients $\frac{dN_j}{dx}$, $\frac{dT}{dx}$, $\frac{d\ln\rho}{dx}$ at a point in the numerical integration.

To proceed the computation, it is required to obtain h_j, $\hat{\mu}_j^0$, and s_j^0 for each species at a given temperature as discussed before. In the NENZF code, thermal equilibrium flow or frozen flow are assumed, and harmonic oscillator model is used at a temperature below 5000 K typically and a curve fit method (referred as thermo-fit below) is switched above the temperature where the harmonic oscillator model is not expected valid instead. The harmonic oscillator model in the NENZF program however is effective only for diatomic molecules but not for polyatomic ones such as carbon dioxide. To deal with the problem, a slight modification had been made for T5 diagnostic data analysis so that thermo-fit method is used throughout the temperature range for carbon dioxide properties. Thermo-fit data for carbon dioxide valid at relatively low temperature (up to 6000 K) have been obtained by correlation with JANAF data mentioned previously. The curve fit is made by the following form:

$$\frac{\hat{\mu}_j^0 - \hat{h}_{j0}^0}{\hat{R}T} = a_j(1 - \ln T) - b_j T - \frac{c_j}{2}T^2 - \frac{d_j}{3}T^3 - \frac{e_j}{4}T^4 - k_j,$$

where $\hat{h}_{j0}^0$ is the formation enthalpy of jth species at standard conditions per mole. Then enthalpy

and entropy can be compared with the JANAF table:

$$\frac{\hat{h}_j - \hat{h}^0_{j_0}}{\hat{R}T} = a_j + b_j T + c_j T^2 + d_j T^3 + e_j T^4,$$
$$\frac{\hat{s}^0_j}{\hat{R}} = \frac{\hat{h}_j - \hat{\mu}^0_j}{\hat{R}T}.$$

Table C.1: Thermofit coefficients used in NENZF calculations

Species	a_j	b_j, 1/K	c_j, 1/K^2	d_j, 1/K^3	e_j, 1/K^4	k_j
N_2	3.4515	3.0883×10^{-4}	-4.2514×10^{-8}	2.7393×10^{-12}	-5.4683×10^{-17}	3.0713
O_2	3.2495	4.9634×10^{-4}	-6.7018×10^{-8}	4.4433×10^{-12}	-1.0003×10^{-16}	5.9150
N	3.0089	-3.1346×10^{-4}	6.3118×10^{-8}	-4.1652×10^{-12}	9.3349×10^{-17}	1.3035
O	2.5941	-5.0089×10^{-5}	1.1995×10^{-8}	-8.6816×10^{-13}	2.1481×10^{-17}	4.6006
NO	3.7562	2.0840×10^{-4}	-2.6395×10^{-8}	1.6903×10^{-12}	-3.6115×10^{-17}	3.6112
CO_2	3.0251	2.9082×10^{-3}	-9.5461×10^{-7}	1.5194×10^{-10}	-9.1524×10^{-15}	6.8901
CO	3.3561	3.2473×10^{-4}	-1.3970×10^{-9}	-1.0914×10^{-11}	1.1519×10^{-15}	4.4018
C	2.6588	-1.7476×10^{-4}	7.5554×10^{-8}	-1.2250×10^{-11}	7.3726×10^{-16}	3.9289

C.3 BLIMPK: Non-equilibrium 2-Dimensional Boundary Layer Code

Boundary layer equations in hypervelocity flow has been discussed in some text books such as those by Dorrance[72] or Anderson[94]. As for BLIMPK code, there are some user's guide available and a detailed description can be found in a report by Tong *et al.*[74] and also Adam[76] describes its algorithms and applications to T5 test conditions. Thus, only a brief description of the algorithms is attempted in this section. The governing equations for the reacting boundary layer are,

$$\frac{\partial}{\partial s}(\rho u r^\kappa) + \frac{\partial}{\partial y}(\rho v r^\kappa) = 0, \tag{C.8}$$

$$\rho u \frac{\partial u}{\partial s} + \rho v \frac{\partial u}{\partial y} = \frac{1}{r^\kappa}\frac{\partial}{\partial y}\left[r^\kappa(\mu + \epsilon_M)\frac{\partial u}{\partial y}\right] - \frac{\partial p}{\partial s}, \tag{C.9}$$

$$\begin{aligned}\rho u \frac{\partial I}{\partial s} + \rho v \frac{\partial I}{\partial y} = \frac{1}{r^\kappa}\frac{\partial}{\partial y}\Bigg\{ r^\kappa \Bigg[&(\mu + \epsilon_M)\frac{\partial (u^2/2)}{\partial y} + (\lambda + \epsilon_H \overline{C_p})\frac{\partial T}{\partial y} \\ &+ \sum_i \left(\epsilon_D \frac{\partial C_i}{\partial y} - J_i\right) h_i \\ &- \frac{RT}{\rho}\sum_i \sum_j \frac{x_j D_i^T}{M_i \mathcal{D}_{ij}}\left(\frac{J_i}{C_i} - \frac{J_j}{C_j}\right)\Bigg]\Bigg\},\end{aligned} \tag{C.10}$$

$$\rho u \frac{\partial C_i}{\partial s} + \rho v \frac{\partial C_i}{\partial y} = \frac{1}{r^\kappa}\frac{\partial}{\partial y}\left[r^\kappa\left(\epsilon_{D_i}\frac{\partial C_i}{\partial y} - J_i\right)\right] + \psi_i, \tag{C.11}$$

where κ equals 1 for axisymmetric flow and 0 for two-dimensional flows. μ, λ and $\mathcal{D}_{ij}$ are viscosity, thermal conductivity, and binary diffusivity which can be approximated by $\mathcal{D}_{ij} \approx \frac{\bar{D}}{F_i F_j}$, where D is a reference diffusivity, F_i is a diffusion factor for ith species. D^T is the thermal diffusivity. And ϵ_M, ϵ_H, ϵ_D are respectively turbulent eddy viscosity, turbulent eddy conductivity and turbulent eddy diffusivity, defined as:

$$\epsilon_M \equiv -\frac{\overline{(\rho v)' u'}}{\partial \bar{u}/\partial y},$$

$$\epsilon_H \equiv -\frac{\overline{(\rho v)' h_i'}}{\partial \bar{T}/\partial y},$$

$$\epsilon_D \equiv -\frac{\overline{(\rho v)' C_i'}}{\partial \bar{C}_i/\partial y},$$

and I is total enthalpy defined as $I \equiv h + u^2/2$, J_i denotes diffusional mass flux of ith species. ψ_i is the rate of mass generation of ith species due to chemical reactions.

Now, introduce the following transformation,

$$\xi \equiv \int_0^s \rho_e u_e \mu_e r_0^{2\kappa} ds$$
$$\eta \equiv \frac{u_e}{\alpha_H \sqrt{2\xi}} \int_0^y \rho r^\kappa dy$$
$$f_w \equiv -\frac{1}{\sqrt{2\xi}} \int_0^\xi \frac{\rho_w v_w}{\rho_e u_e \mu_e r^\kappa} d\xi$$
$$f \equiv f_w + \alpha_H \int_0^\eta \frac{u}{u_e} d\eta.$$

This transformation leads to a set of equations to be solved numerically with respect to f, I and C_k:

$$f f'' + \left[\frac{C\left(1 + \frac{\epsilon_M}{\mu}\right)}{\alpha_H} f'' \right]' + \beta \left(\alpha_H^2 \frac{\rho_e}{\rho} - f'^2 \right) = 2 \left(f' \frac{\partial f'}{\partial \ln \xi} - f'^2 \frac{\partial \alpha_H}{\partial \ln \xi} - f'' \frac{\partial f}{\partial \ln \xi} \right), \tag{C.12}$$

$$f I' = 2 \left(f' \frac{\partial I}{\partial \ln \xi} - I' \frac{\partial f}{\partial \ln \xi} \right), \tag{C.13}$$

$$f C_k' + \left(\frac{\epsilon_M}{\alpha_H S_{C_t}} C_k' - J_k^* \right)' + \left(\frac{\psi_k}{\rho} \right) \left(\frac{\rho_e \mu_e \alpha_H}{\alpha^{*2}} \right) = 2 \left(f' \frac{\partial C_k'}{\partial \ln \xi} - C_k' \frac{\partial f}{\partial \ln \xi} \right) \tag{C.14}$$

where $*$ refers to quantities that have been appropriately non-dimensionalized. The streamwise pressure gradient parameter β and the Chapman-Rubesin parameter C are respectively defined as

$$\beta \equiv 2 \frac{\partial \ln u_e}{\partial \ln \xi}$$
$$C \equiv \frac{\rho \mu}{\rho_e \mu_e}$$

C.4 Inviscid 2-Dimensional Linear Stability Analysis

In the present study, linear evolution of 'frozen disturbances' traveling through non-equilibrium boundary layer is of our interest, since sound absorption estimation deals with 'non-equilibrium effects' on the evolution of the disturbance wave. The author, then, extended two dimensional, inviscid perfect gas algorithm of linear instability described in detail by Mack[22] into frozen disturbances through profile with arbitrary chemical composition, *i.e.*, accounting distributions in specific heat and/or molecular weight (though, thermal equilibrium is assumed). It would be still useful to outline the extended procedure which includes perfect gas equations as a special form, although it has been decided not to use it in the present study, simply due to insufficient number of nodes allowed in the boundary layer profile computation (BLIMPK). According to Mack[22], linearized small perturbation equations can be written as follows:

$$\rho_0\left[i(\alpha u_0+\beta w_0-\omega)\hat{e}'+\frac{\partial e_0}{\partial y}\hat{v}'\right]=\left(\frac{p_e}{\rho_e e_e}\right)\left(\frac{\partial}{\partial y}\hat{v}'+i\tilde{\alpha}\tilde{u}'\right)\qquad\text{energy} \tag{C.15}$$

$$\hat{p}'=\frac{\hat{r}'}{\rho_0}+\frac{\hat{e}'}{C_vT_0}\qquad\text{state} \tag{C.16}$$

$$\rho\left[i(\alpha u_0+\beta w_0-\omega)\tilde{\alpha}\tilde{u}'+\left(\alpha\frac{\partial u_0}{\partial y}+\beta\frac{\partial w_0}{\partial y}\right)\hat{v}'\right]=-i\frac{p_e}{\rho_e u_e^2}(\alpha^2+\beta^2)\hat{p}'\qquad x'\text{-momentum} \tag{C.17}$$

$$i\rho_0(\alpha u_0+\beta w_0-\omega)\hat{v}'=-\frac{p_e}{\rho_e u_e^2}\frac{\partial\hat{p}'}{\partial y}\qquad y\text{-momentum} \tag{C.18}$$

$$i(\alpha u_0+\beta w_0-\omega)\hat{r}'+\rho_0\left(\frac{\partial}{\partial y}\hat{v}'+i\tilde{\alpha}\tilde{u}'\right)+\frac{\partial\rho_0}{\partial y}\hat{v}'=0\qquad\text{continuity}\qquad, \tag{C.19}$$

$$\tag{C.20}$$

where, energy equation is written in terms of e not temperature T, here. C_v denotes specific heat at constant volume, ($\equiv\frac{\partial e}{\partial T}_{v:\text{constant}}$), and all quantities are non-dimensionalized by their edge values as:

$$p\equiv\frac{p^*}{p_e},\qquad \rho\equiv\frac{\rho^*}{\rho_e},\qquad T\equiv\frac{T^*}{T_e}$$
$$u\equiv\frac{u^*}{u_e},\qquad v\equiv\frac{v^*}{v_e},\qquad w\equiv\frac{w^*}{w_e}$$

where $*$denotes dimensional quantities, and:

$$\begin{pmatrix} u(x,y,z,t) \\ v(x,y,z,t) \\ w(x,y,z,t) \\ p(x,y,z,t) \\ \rho(x,y,z,t) \\ e(x,y,z,t) \end{pmatrix} = \begin{pmatrix} u_0(x,y,z) \\ v_0(x,y,z) \\ w_0(x,y,z) \\ p_0(x,y,z) \\ \rho_0(x,y,z) \\ e_0(x,y,z) \end{pmatrix} + e^{i(\alpha x+\beta z-\omega t)} \begin{pmatrix} \hat{u}'(y) \\ \hat{v}'(y) \\ \hat{w}'(y) \\ \hat{p}'(y) \\ \hat{r}'(y) \\ \hat{e}'(y) \end{pmatrix}$$

$$T(x,y,z,t) = T_0(x,y,z) + \frac{\hat{e}'(y)e^{i(\alpha x+\beta z-\omega t)}}{C_v(y)}$$

$$\tilde{\alpha}\tilde{u}' = \alpha\hat{u}' + \beta w'$$

Substituting equation C.16 to equation C.19 eliminates $\hat{r}'$:

$$-i\frac{\rho_0}{C_vT_0}(\alpha u_0 + \beta w_0 - \omega)\hat{e}' + i\rho_0(\alpha u_0 + \beta w_0 - \omega)\hat{p}' + \rho_0\left(\frac{\partial}{\partial y}\hat{v}' + i\tilde{\alpha}\tilde{u}'\right) + \frac{\partial\rho_0}{\partial y}\hat{v}' = 0 \qquad \text{(C.21)}$$

Substituting equation C.15 to equation C.21 to eliminate $\hat{e}'$ gives:

$$\left[\frac{1}{C_vT_0}\left(\frac{p_e}{\rho_e e_e}\right) + \rho_0\right]\left(\frac{\partial}{\partial y}\hat{v}' + i\tilde{\alpha}\tilde{u}'\right) + \left(\frac{\rho_0}{C_vT_0}\frac{\partial e_0}{\partial y} + \frac{\partial\rho_0}{\partial y}\right)\hat{v}' i\rho_0(\alpha u_0 + \beta w_0 - \omega)\hat{p}' = 0$$

Using the above equation to eliminate $\tilde{u}'$, equation C.17 gives a relation of $\frac{\partial\hat{v}'}{\partial y}$ with $\hat{v}'$ and $\hat{p}'$. Combined with equation C.18, a closed form of equations for frozen small perturbation can be obtained:

$$\begin{aligned}(\alpha u_0 + \beta w_0 - \omega)\frac{\partial\hat{v}'}{\partial y} = &\left[\left(\alpha\frac{\partial u_0}{\partial y} + \beta\frac{\partial w_0}{\partial y}\right) - \frac{(\alpha u_0 + \beta w_0 - \omega)\left(\frac{1}{C_vT_0}\frac{\partial e_0}{\partial y} + \frac{1}{\rho_0}\frac{\partial\rho_0}{\partial y}\right)}{\frac{1}{C_v\rho_0T_0}\frac{p_e}{\rho_e e_e} + 1}\right]\hat{v}' \\ &+ i\left[\frac{1}{\rho_0}\frac{p_e}{\rho_e u_e^2}(\alpha^2+\beta^2) - \frac{(\alpha u_0 + \beta w_0 - \omega)^2}{\frac{1}{C_v\rho_0T_0}\frac{p_e}{\rho_e e_e} + 1}\right]\hat{p}' \end{aligned} \qquad \text{(C.22)}$$

$$\frac{\partial\hat{p}'}{\partial y} = -i\left(\frac{\rho_e u_e^2}{p_e}\right)\rho_0(\alpha u_0 + \beta w_0 - \omega)\hat{v}' \qquad \text{(C.23)}$$

It is not difficult to see that the above equations reduce to the equations 2.1 and 2.2 when the specific heat ratio γ is constant throughout the boundary layer.

To find a set of boundary conditions to start with, the solution of the above equations for

freestream condition is required. Remembering $u_0 = 1$ in the freestream (or external flow), the solution is:

$$\hat{p}' = i(\alpha - \omega)e^{-\sqrt{C_A/P_u}y} \tag{C.24}$$

$$\hat{v}' = \sqrt{P_u C_A}e^{-\sqrt{C_A/P_u}y}, \tag{C.25}$$

where,

$$C_A = P_u(\alpha^2 + \beta^2) - \frac{\alpha - \omega}{\frac{P_e}{C_v} + 1}$$

$$P_u = \frac{p_e}{\rho_e u_e^2}$$

$$P_e = \frac{p_e}{\rho_e e_e}$$

Appendix D Coefficients for chemical reaction, relaxation and transport properties

This section summarizes data used in the present study to estimate equilibrium properties, chemical reaction rate and relaxation rate in vibrational excitation. Data sources are Lordi[57] for NENZF calculation, Park[95] for gas phase reactions, and Chen *et al.*[77] for surface reactions. Information for the transport properties were taken from several literatures including Park *et al.*[96]and Poling *et al.*[63]. As had been described, those for the vibrational relaxation was taken from Millikan and White[49] for air related molecules and Camac[50] for carbon dioxide molecule. Table D.1 shows properties of chemical species which may exist under the present experiment conditions in the T5 hypervelocity shock tunnel.

Table D.1: Properties used in the calculations

species	M_w	$\sigma_{\text{sym}}\Theta_{rot}$	h_f^o	g_v	Θ_v	g_{e_o}	g_{e_i}	ϵ_e	ε_{pw}/k_B	σ_{col}	μ_p
	g/mol	K	J/mol		K			J/mol	K	Å	Debye
N_2	28.016	5.79	0.0	1	3353.2	1	3	6.015×10^5	97.53	3.621	0.0
							6	7.136×10^5			
							1	7.342×10^5			
O_2	32.000	4.16	0.0	1	2239.0	3	2	9.225×10^4	107.40	3.458	0.0
							1	1.579×10^5			
							3	4.320×10^5			
							3	5.960×10^5			
Ar	39.944	–	0.0	–	–	1	5	1.115×10^6	136.50	3.330	0.0
							3	1.122×10^6			
N	14.008	–	4.713×10^5	–	–	4	6	2.301×10^5	72.40	3.298	0.0
							4	2.308×10^5			
							6	3.452×10^5			
							12	9.971×10^5			
O	16.000	–	2.468×10^5	–	–	5	3	1.903×10^3	80.00	2.750	0.0
							1	2.717×10^3			
							5	1.899×10^5			
							1	4.044×10^5			
							5	8.829×10^5			
NO	30.008	2.45	8.990×10^4	1	2699.2	4	2	5.262×10^5	97.53	3.621	0.0
							4	5.496×10^5			
C	12.011	–	7.116×10^5	–	–	1	3	1.962×10^2	30.50	3.385	0.0
							5	5.204×10^2			
							5	1.219×10^5			
							1	2.590×10^5			
							5	4.036×10^5			
CO_2	44.011	1.13	-3.933×10^5	2	960.1	1			98.10	3.650	0.0
				1	1992.5						
				1	3380.2						
CO	28.011	2.78	-1.139×10^5	1	3082.0	1	6	5.824×10^5	98.10	3.650	0.0
							3	6.687×10^5			
							6	7.453×10^5			
							2	7.785×10^5			

D.1 Rate Coefficients of Chemical Reactions : Air and nitrogen shots

Table D.2: Air shots (NENZF)

Third Body	C_f m^3/mole s	η_f	Θ_f K
	$N_2 \leftrightarrows 2N$		
N_2	2.30×10^{23}	-3.5	113260.
N	8.50×10^{19}	-2.5	113260.
the others	9.90×10^{14}	-1.5	113260.
	$O_2 \leftrightarrows 2O$		
O_2	3.60×10^{15}	-1.5	59390.
O	2.10×10^{12}	-0.5	59390.
the others	1.20×10^{15}	-1.5	59390.
	$NO \leftrightarrows N+O$		
any species	5.20×10^{15}	-1.5	75500.
	$O_2+N \leftrightarrows O+NO$		
none	1.00×10^{6}	0.5	3625.
	$N_2+O \leftrightarrows N+NO$		
none	5.00×10^{7}	0.0	38020.
	$N_2+O_2 \leftrightarrows 2NO$		
none	9.10×10^{18}	-2.5	65010.

Table D.3: Air shots (BLIMPK& absorption)

Third Body	C_f m^3/mole s	η_f	Θ_f K
	$N_2 \leftrightarrows 2N$		
N or O	3.00×10^{16}	-1.6	113200.
the others	7.00×10^{15}	-1.6	113200.
	$O_2 \leftrightarrows 2O$		
N or O	1.00×10^{16}	-1.5	59500.
the others	2.00×10^{15}	-1.5	59500.
	$NO \leftrightarrows N+O$		
N_2 or O_2	5.00×10^{9}	0.0	75500.
the others	1.10×10^{11}	0.0	75500.
	$N_2+O \leftrightarrows N+NO$		
none	6.40×10^{11}	-1.0	38400.
	$O+NO \leftrightarrows O_2+N$		
none	8.40×10^{6}	0.0	19400.

Table D.4: Surface reactions : Air shots $J_M/M_{w_M} = k_{p,f}(\prod p_i^{\nu_i'} - \frac{1}{K_p}\prod p_i^{\nu_i''})$ (mole per unit time and unit area)

Surface reaction	k_{pf}, mole/m^{2}s atm$^{\sum \nu_i'}$
O$\rightarrow \frac{1}{2}$O$_2$	5×10^9
N$\rightarrow \frac{1}{2}$N$_2$	5×10^9
NO$\rightarrow \frac{1}{2}$O$_2$+$\frac{1}{2}$N$_2$	5×10^9

D.2 Rate Coefficients of Chemical Reactions : Carbon dioxide shots

Table D.5: CO_2 shots

Third Body	C_f m^3/mole s	η_f	Θ_f K
CO$_2 \leftrightarrows$CO+O			
any species	2.88×10^5	0.5	37655.
2CO$\leftrightarrows$CO$_2$+C			
none	2.33×10^3	0.5	65700.
CO+O$_2\leftrightarrows$CO$_2$+O			
none	1.60×10^7	0.0	20640.
CO$\leftrightarrows$C+O			
CO	1.76×10^{24}	-3.52	128750.
O	1.29×10^{25}	-3.52	128750.
the others	8.79×10^{23}	-3.52	128750.
O$_2\leftrightarrows$2O			
O$_2$	2.75×10^{13}	-1.0	59390.
O	2.10×10^{12}	-0.5	59390.
the others	2.55×10^{12}	-1.0	59390.
CO+O$\leftrightarrows$O$_2$+C			
none	2.73×10^5	0.5	69520.

Table D.6: Surface reactions : CO_2 shots $J_M/M_{w_M} = k_{p,f}(\prod p_i^{\nu_i'} - \frac{1}{K_p}\prod p_i^{\nu_i''})$ (mole per unit time and unit area)

Surface reaction	k_{pf}, mole/m^{2}s atm$^{\sum \nu_i'}$
C+O$\rightarrow$CO	5×10^9
CO+O$\rightarrow$CO$_2$	5×10^9
O$\rightarrow \frac{1}{2}$O$_2$	5×10^9